UNIVERSIDADE FEDERAL DE SÃO CARLOS
CENTRO DE CIÊNCIAS BIOLÓGICAS E DA SAÚDE
PROGRAMA DE PÓS-GRADUAÇÃO EM ECOLOGIA E RECURSOS NATURAIS

SABRINA LARISSA BELATTO

PRESERVAÇÃO EXCEPCIONAL DE INSETOS FÓSSEIS DA FORMAÇÃO CRATO (CRETÁCEO INICIAL, BRASIL) POR MEIO DE TÉCNICAS PALEOMÉTRICAS

São Carlos - SP

2025

SABRINA LARISSA BELATTO

Preservação excepcional de insetos fósseis da Formação Crato (Cretáceo Inicial, Brasil) por meio de técnicas paleométricas

Dissertação apresentada ao Programa de Pós-Graduação em Ecologia e Recursos Naturais da Universidade Federal de São Carlos como parte dos requisitos para obtenção do título de MESTRE ECOLOGIA E RECURSOS NATURAIS

Orientador: Dr. Gabriel Ladeira Osés

Coorientadora: Profa. Dra. Mírian Liza Alves Forancelli Pacheco

São Carlos - SP

2025

Belatto, Sabrina Larissa

Preservação excepcional de insetos fósseis da Formação Crato (Cretáceo inicial, Brasil) por meio de técnicas paleométricas. / Sabrina Larissa Belatto -- 2025.
113f.

Dissertação (Mestrado) - Universidade Federal de São Carlos, campus São Carlos, São Carlos
Orientador (a): Gabriel Ladeira Osés
Banca Examinadora: Alexandre Ribeiro Cardoso, Gabriel Ladeira Osés, Jaime Joaquim Dias Prata
Bibliografia

1. Paleontologia. 2. Fossildiagenese. 3. Tafonomia. I. Belatto, Sabrina Larissa. II. Título.

Ficha catalográfica desenvolvida pela Secretaria Geral de Informática (SIn)

DADOS FORNECIDOS PELO AUTOR

Bibliotecário responsável: Arildo Martins - CRB/8 7180

UNIVERSIDADE FEDERAL DE SÃO CARLOS

Centro de Ciências Biológicas e da Saúde
Programa de Pós-Graduação em Ecologia e Recursos Naturais

Folha de Aprovação

Defesa de Dissertação de Mestrado da candidata Sabrina Larissa Belatto, realizada em 26/06/2025.

Comissão Julgadora:

Prof. Dr. Gabriel Ladeira Osés (USP)

Prof. Dr. Alexandre Ribeiro Cardoso (UFVJM)

Prof. Dr. Jaime Joaquim Dias Prata (UFRJ)

O Relatório de Defesa assinado pelos membros da Comissão Julgadora encontra-se arquivado junto ao Programa de Pós-Graduação em Ecologia e Recursos Naturais.

DEDICATÓRIA

Aos meus pais, pilares de minha caminhada; ao meu marido, fiel e digno*; in memoriam* dos meus avós, que me ensinaram que há sabedoria no tempo. E a todos que ousam interrogar o mundo, mesmo quando ele responde com silêncio — que a ciência siga sendo nosso gesto mais humilde e mais audaz diante do desconhecido.

AGRADECIMENTOS

Aos meus pais, Ilenice Nogueira e Pedro Donizetti Belatto a quem serei grata antes de qualquer formalidade. A vocês, que sustentaram meus ombros cansados quando eu mesma já não acreditava na força que havia neles. Por cada gesto silencioso de cuidado, por cada palavra dita ou contida, por cada noite em que perderam o sono por minha causa: esta conquista é tão de vocês quanto minha. Foram vocês que me ensinaram que o amor verdadeiro é aquele que permanece firme mesmo quando tudo o mais vacila. E a vocês eu dedico tudo até aqui, e tudo o que virá depois.

Se foram meus pais que me ensinaram a resistir com amor, foi durante esses dois anos, por meio do meu orientador, Dr. Gabriel Ladeira Osés, que consegui transformar essa resistência em pensamento, método e criação

A você, Gabs, minha admiração e gratidão sinceras. Sua escuta atenta, orientação impecável e entusiasmo foram fundamentais para que eu redescobrisse a confiança no meu trabalho. Sob sua orientação, este trabalho se tornou possível e se transformou em algo maior do que um simples requisito acadêmico. Obrigada por acreditar em mim em todos os momentos, sem dúvidas e sem hesitações.

Também expresso, com especial carinho, meu apreço à minha coorientadora, Profa. Dra. Mírian Liza Alves Forancelli Pacheco, por ter protagonizado este reencontro com a minha paixão pela pesquisa. Sua presença foi farol em um dos momentos mais escuros da minha trajetória – e bastou um comentário seu, firme, para reacender em mim a chama da ciência. Obrigada por me lembrar que ainda havia um lugar para mim na paleontologia.

Agradeço imensamente aos meus colegas de academia, Silvio Cesar Marqui Limeira Junior, Thândara Jacob, Ludmilla Fernanda dos Reis, Gabriel Eduardo Baréa de Barros e Allan Mello Macedo. Com vocês, aprendi que fazer ciência não precisa ser sinônimo de solidão. Foram companhia e apoio em meu dia a dia acadêmico. Em especial, agradeço à Thândara e à Ludmilla, que me acolheram quando cheguei fragilizada.

Dedico também às minhas colegas de profissão, que se tornaram grandes amigas pessoais, Thaís Rabito Pansani e Jacqueline Freitas Oliveira. Muito obrigada por serem exemplos, por me ouvirem com atenção e por serem minhas melhores conselheiras. Thais, você é a minha inspiração de vida.

À todas as mulheres incríveis que estiveram ao meu lado, obrigada por me lembrarem que mulheres que se apoiam, caminham juntas – e resistem.

Ao Prof. Dr. Renato Pirani Ghilardi, meu primeiro orientador, agradeço por ter me apresentado ao caminho da paleontologia e ao fascínio do tempo profundo. Foi você quem plantou, ainda na juventude da minha vida acadêmica, a semente de uma paixão que por tanto tempo permaneceu em dormência, mas que floresceu nestas páginas.

Agradeço ao Laboratório de Paleontologia e Astrobiologia (LPA/UFSCar) e ao Laboratório de Arqueometria e Ciências Aplicadas ao Patrimônio Cultural (LACAPC/IFUSP), meus "lares" fundamentais para meu crescimento na pesquisa.

Agradeço também ao Laboratório de Paleoecologia e Paleoicnologia (LPP) e ao Laboratório de Ecologia de Interações, ambos vinculados ao DEBE – UFSCar – São Carlos, por me acolherem durante todo o período de cumprimento das disciplinas. Estendo esse agradecimento ao Prof. Dr. Marcelo Adorna Fernandes e à Profa. Dra. Carolina Reigada Montoya, pelo acolhimento.

Registro também meus agradecimentos ao Laboratório de Quimiosfera (IQc-USP), ao Instituto de Física da USP (IF-USP), ao Instituto de Geociências da USP (IGc-USP) e ao Laboratório Nacional de Nanotecnologia (LNNano/CNPEM), cujas contribuições foram essenciais em diferentes etapas da pesquisa.

Este trabalho foi financiado pelo Conselho Nacional de Desenvolvimento Científico e Tecnológico (CNPq), por meio da bolsa de mestrado (processo nº 131500/2023-6), que possibilitou minha dedicação integral ao desenvolvimento desta pesquisa.

Reconheço também o apoio da Fundação de Amparo à Pesquisa do Estado de São Paulo (FAPESP) pelos projetos vinculados ao meu orientador, Dr. Osés (processos nºs FAPESP: 2022/06485-5; 2023/14250-0; 2023/17293-2) e à minha coorientadora Dra. Pacheco (processo nº 2023/04501-6), cujos aportes financeiros e suporte institucional foram indispensáveis.

O presente trabalho foi também realizado com apoio da Coordenação de Aperfeiçoamento de Pessoal de Nível Superior – Brasil (CAPES) – Código de Financiamento 001 (PROAP/CAPES PPGERN).

Por trás de todo esforço e resultado acadêmico, há pilares que não aparecem nas métricas, mas sem os quais nenhum projeto se sustenta. Agradeço agora, um a um dos meus "pilares", com profunda estima:

Ao meu companheiro de vida, Joseph Ou, dedico não apenas estas páginas, mas todos os dias em que continuei lutando por este sonho. Você, mesmo à distância, foi uma presença constante – minha base, meu alívio, meu apoio em cada momento. Obrigada por me amparar nas crises existenciais, por me ouvir quando eu nem sabia o que estava dizendo, por ficar ao meu lado mesmo nos dias em que tudo parecia estar um caos. Esta vitória é nossa – da nossa fidelidade, da nossa união e da nossa escolha de continuarmos nos escolhendo, todos os dias.

Aos meus avós, José Belatto, Leontina Nogueira e Leonilda Belatto, dedico cada verso escrito com lágrimas, em meio a um luto que não pude viver plenamente. Vocês me ensinaram, com amor e muita singeleza, o valor da vida, das pequenas coisas, da ternura e da dignidade, mesmo tendo vivido uma vida difícil, entre a poeira e o sol de uma vida forjada na terra. A Vó Tina e o Vô Zezinho, partiram durante este processo de pesquisa e escrita, e não puderam me ver chegar ao fim desta trajetória – a dor de não poder compartilhar com vocês esta vitória será sempre um lamento mudo. A Vó Nica, agora se despede aos poucos desta vida, e muitas vezes é incapaz de reconhecer a neta que tanto a ama. Deixo a vocês a minha gratidão mais profunda e aqui registro a saudade que me acompanhou em cada linha escrita, em cada dia e em cada madrugada de trabalho. Esta dissertação é, também, um tributo à memória viva que vocês deixaram em mim – e a tudo o que sou, graças ao carinho e ao zelo com que me criaram.

Aos meus fiéis guardiões felinos dos dias e das noites (Jiraya, Gaia, Krika, Margaretti, Luna e agregados), agradeço o amor puro e sincero. Seus ronronares e olhares atentos me acompanharam em noites solitárias de estudo, nunca permitindo que o silêncio noturno me alcançasse. Vocês aqueceram os pés e o coração de uma pesquisadora cansada. A ciência, por mais racional que seja, também se faz de afetos.

Ao meu primo-irmão, Vinicius Lemos Belatto, minha gratidão mais terna. Nestes dois anos tão intensos, você foi refúgio, foi riso e leveza nas pausas, cumplicidade nos momentos em que eu precisava lembrar de viver. Obrigada por me lembrar de quem sou fora da pesquisa, e por sempre estar por perto quando mais precisei.

À Ingrid Natália Nunes, minha melhor amiga, agradeço profundamente por sua amizade generosa. Obrigada por entender com doçura os meus afastamentos e minha demora de semanas em responder suas mensagens, e por me receber de braços abertos a cada reencontro. Você foi como uma âncora emocional: sólida, firme, leal. Você me lembrou, sem palavras, que as verdadeiras amizades resistem ao tempo, à ausência e às tempestades.

A todos que cruzaram meu caminho nesta jornada, obrigada por me ajudarem a escrever, com afeto e resiliência, uma nova página da minha história. Quando, para muitos, o mestrado é apenas o começo, para mim ele significou um recomeço. E, dentre todo o conhecimento que adquiri nesses dois anos, o que mais me trouxe sabedoria foi entender que nenhuma conquista é verdadeiramente individual – ela carrega em si os gestos, os abraços, as palavras e um pedacinho de todos que caminharam ao nosso lado.

"Insects don't lie. They are silent witnesses to time and death — all I have to do is listen."

— Gil Grissom, CSI: Crime Scene Investigation

RESUMO

Os fósseis da Formação Crato fazem parte de um depósito *Konservat-Lagerstätten* e são centrais nos debates sobre os processos paleobiológicos e geoquímicos que governam a fossilização. A Formação Crato (Aptiano, Bacia do Araripe, NE do Brasil) representa um desses depósitos excepcionais, com a preservação tridimensional de insetos em calcários laminados com a intercalação de calcários bege e calcários cinza. Este trabalho investigou a composição química e mineralógica de fósseis de insetos de calcário cinza (*grey limestone*, GL), por meio de uma abordagem paleométrica — espectroscopia Raman, fluorescência de raios X (XRF), microscopia eletrônica de varredura com espectroscopia de dispersão de energia de raios X acoplada (MEV-EDS) e preparo de lamelas ultrafinas por *Focused Ion Beam – Scanning transmission electron microscopy* (FIB-STEM). Os resultados revelam a presença recorrente de pirita framboidal na cutícula dos fósseis, enquanto os compartimentos internos estão enriquecidos em sulfatos de ferro, principalmente jarositas. A distribuição zonada desses minerais é interpretada como microambientes diagenéticos com variação espacial de pH e condições redox: a pirita precipitou em zonas periféricas tamponadas, enquanto regiões internas mais ácidas favorecem a formação de jarositas. Tais padrões complementam o modelo tafonômico anterior, que restringia a piritização aos calcários beges, e demonstram que diferentes regimes mineralizantes podem coexistir no GL. Propõe-se, portanto, um novo modelo tafonômico para os insetos da Formação Crato, no qual a compartimentalização geoquímica interna e a ação microbiana definem gradientes de preservação mineral em escala micro a nanométrica.

Palavras-chave: Piritização; fosfatização; modelo tafonômico; fossildiagênese; tafonomia.

ABSTRACT

Fossils from the Crato Formation are part of a Konservat-Lagerstätten deposit and are central to debates on the paleobiological and geochemical processes governing fossilization. The Crato Formation (Aptian, Araripe Basin, NE Brazil) represents one of these exceptional deposits, with three-dimensional preservation of insects in laminated limestones, alternating between beige and grey limestone. This study investigated the chemical and mineralogical composition of insect fossils from grey limestone (GL) through a paleometric approach—Raman spectroscopy, X-ray fluorescence (XRF), scanning electron microscopy with energy-dispersive X-ray spectroscopy (SEM-EDS), and ultrathin lamella preparation by Focused Ion Beam – Scanning Transmission Electron Microscopy (FIB-STEM). Results reveal the recurrent presence of framboidal pyrite in the fossil cuticle, whereas internal compartments are enriched in iron sulfates, mainly jarosites. The zoned distribution of these minerals is interpreted as diagenetic microenvironments with spatial variation in pH and redox conditions: pyrite precipitated in buffered peripheral zones, while more acidic internal regions favored jarosite formation. These patterns complement the previous taphonomic model, which limited pyritization to beige limestones, and demonstrate that different mineralizing regimes can coexist in GL. We propose a new taphonomic model for Crato Formation insects, in which internal geochemical compartmentalization and microbial activity define mineral preservation gradients at micro- to nanoscale.

Keywords: Pyritization; phosphatization; taphonomic model; fossil diagenesis; taphonomy.

LISTA DE FIGURAS

FIGURA INTRODUÇÃO GERAL - CONTEXTO GEOLÓGICO

FIGURAS MATERIAIS E MÉTODOS

Figura 5. Esquema ilustrando o preparo de lamela ultra fina de fibra muscular por feixe de íons focalizados (FIB). À esquerda, o feixe de íons realiza o fresamento preciso da amostra sob visualização simultânea por MEV. À direita, a lamela obtida é fixada em um suporte de cobre (grid) com auxílio de um micromanipulador, etapa essencial para posterior análise em STEM-EDS (Foto confeccionada pelo aplicativo android IBIS-Paint pela autora).

FIGURAS CAPÍTULO ÚNICO - Investigating the complexity of exceptional fossil preservation: an integrative model for insects from the Crato formation.

Figure 1. Legend: Geological map and the stratigraphic chart of the Araripe Basin. The insect fossil specimens are from the late Aptian Crato Formation (Santana Group). PI: Piauí State; PE: Pernambuco State; CE: Ceará State; PB: Paraíba State; JUR.: Jurassic; TITHON.: Tithonian; BERRIAS.: Berriasian; VALANG.: Valanginian; HAUTER.: Hauterivian; BARREM.: Barremian; CENOM.: Cenomanian. The nomenclature of the lithostratigraphic units is based on Assine et al. (2014). The geological map is modified from Assine (2007) and Dias et al. (2022).

Figure 2. Photographs of the samples analyzed. Scale (1 cm): **(a - b)** sample GP/1E11237c - Orthoptera; **(c)** sample GP/1E10501 - Orthoptera; **(d - e)** sample GP/1E10609 - Blattodea; **(f)** sample GP/1E10836 - Blattodea.

Figure 3. X-ray fluorescence (XRF) spectra from samples **(a)** GP/1E11237c, **(b)** GP/1E10609, **(c)** GP/1E10501, and **(d)** GP/1E10836, showing element distribution as a function of energy (x-axis, in keV). The spectra correspond to the color-coded points indicated in the photographic insects for each sample. The Ar is naturally detected during XRF analysis, while the gold (Au) signal results from gold-palladium coating for SEM imaging. Scale (5mm).

Figure 4. Scatter plots with linear regressions between major and trace elements as a function of Fe **(a–b)**, S **(c–d)**, and Ca **(e–f)**, with corresponding R^2 values indicated. Each element is represented by a distinct color. Data obtained from normalized XRF analyses.

Figure 5. Representation of chemical elements count in the beige, matrix, and black areas of the fossils on a logarithmic scale. The points correspond to an individual chemical element measurement, as indicated in the legend on the right (Ca, Co, Cr, Cu, Fe, K, Mn, P, Pb, S, Sr, Zn). The boxes illustrate the dispersion of the data in each area, with the inner line indicating the median of the distributions. Statistical comparisons between areas are represented at the top of the figure, with significant levels indicated by asterisks (*** for $p < 0.001$; ns for not significant).

Figure 6. Spearman Correlation Heatmap in the upper triangle, with p-values in the lower triangle. The upper triangle displays Spearman correlation coefficients (ρ), ranging from +1 (strong positive correlation – elements increase together, shown in red tones) to –1 (strong negative correlation – one element increases as the other decreases, shown in bluish tones). Values close to 0 indicate no monotonic correlation (white). The lower triangle shows the p-values associated with each correlation. Values of $p \leq 0.05$ (in green) indicate statistically significant correlations, meaning the association is unlikely to have occurred. P-values > 0.05 (from yellow to white) indicate non-significant correlations, suggesting the observed association may not be statistically robust.

Figure 7. (a) Samples GP/1E11237c and **(b)** GP/1E10609, highlighting the points analyzed by Raman spectroscopy: P1 and P3 (black-colored points – "BP"), P2 and P4 (beige-colored points – "BeP"). **(a1–a2, b1–b2)** Photomicrographs of the measurement points. **(a3–b3)** Raman spectra obtained from the marked regions, with mineral identification: pyrite (FeS_2) in P1 and P3; jarosite in P2 and P4 and sulfate bands. **(c)** Sample GP/1E10501 highlighting the points analyzed by Raman spectroscopy: P5 and P6 (black-colored points – "BP"). **(c1–c2)** Photomicrographs of the measurement points. **(c3)** Raman spectra from the marked regions, with mineral identification: in P5, pyrite (FeS_2), calcium phosphate, and luminescence signals; in P6, pyrite, gypsum, and calcite.

Figure 8. Micrographs of sample GP/1E11237c. **(a)** General view of the sample, with rectangles marked to indicate the areas where the micrographs were obtained, divided into three regions: area 1 — red rectangle (left hind leg); area 2 — green rectangle (abdomen). **(b)** Fragment of area 1 containing preserved muscle fiber, subdivided into two positions with distinct textures: (b1) yellow rectangle and (b2) light blue rectangle. **(c)** Elongated, subhedral

micrometric crystals, slightly covered by anhedral microcrystals, corresponding to position b1. **(d)** Enlargement of position b2. **(e)** Enlarged detail of d, showing rhombohedral, micrometric, euhedral iron sulfide crystals with fine growth striations. **(f)** Preserved muscle fiber. **(g)** Detail of "f". **(h)** Detail of the muscle fiber observed in "f" and "g". **(i)** Microcrystals preserve the muscle fiber of "h", like the crystals in "e", with evident growth striations. **(j)** View another region of muscle fiber. **(k)** Enlargements of "j", showing micrometric, euhedral pyrite crystals covered by granular iron sulfide nanocrystals, with morphologies ranging from subhedral to anhedral. **(l)** Non-identified preserved abdominal organ. **(m)** Magnification of "l". **(n)** Muscle fibers covering the abdominal organ.

Figure 9. SEM-EDS of the localized crystals preserving the muscle fiber (a -e) and the possible organ (g -h) of the samples GP1E11237c. **(a)** Granular nanocrystals observed covering the prismatic crystals. **(b)** Spectra of the prismatic crystals **(c)** Euhedral crystals. **(d)** Spectra of the elemental compositions of rhombohedral crystals. **(e)** The right hind leg, tibiofemoral joint. **(f)** Spectrum of the elemental composition of the crystalline microplot. **(g)** Barium sulfate crystals. **(h)** Spectrum showing the presence of barium sulfate.

Figure 10. FIB-SEM-STEM-EDS analyses fossilized muscle fiber from the sample GP/1E11237c. **(a)** Micrograph of the muscle fiber from which the lamella was extracted by FIB (Focused Ion Beam); the red rectangle indicates the extraction region. **(b)** STEM image showing the top of the lamella, corresponding to the external part of the fiber. **(b1)** Map with superimposition of the distributions of Mg, Fe, and Ca and elemental maps obtained from the top of the lamella (scale - 5µm). **(b2)** EDS sum spectrum **(c)** STEM image of the base of the lamella, which represents the internal portion of the fiber.; the blue and yellow circles mark the region of spectral acquisition. **(c1)** EDS spectrum of the areas marked in "c". **(c3)** Sum spectrum of the analyzed area at the base of the lamella indicated in figure "c". The area marked by the red line in "b-c" in was analyzed by EDS.

Figure 11. SEM micrographs of sample GP/1E10609**. (a)** General view of the fossil with highlighted regions shown in panels (b–i). **(b)** Fine dispersed anhedral crystals with high brightness over a granular substrate. **(c)** Porous texture with predominantly anhedral crystals. **(d)** Preserved surface with branched linear structures over granular regions, suggesting fine fractures distributed on the cuticle or, alternatively, poorly preserved cuticular

ornamentations with secondary infill. **(e)** Thin, elongated, and parallel structures preserved within the internal region of the fossil. The observed organization and morphology are consistent with structures of possible biological origin. **(f)** Compact texture with euhedral crystals. **(g–i)** Muscle fibers preserved in the posterior femoral region of the fossil, showing parallel orientation and a continuous filamentous pattern. **(g)** General view of the region showing organized elongated bundles. **(h)** Intermediate magnification highlighting the linear texture and parallel arrangement of the fibers. **(i)** High-magnification detail revealing well-defined contours.

Figura 12. SEM-EDS of sample GP/1E10609. **(a)** Euhedral nanometric crystals covering rhombohedral crystals. **(b)** Spectrum of micrometric crystals possible galena, or iron sulfate enriched in Pb. **(c)** Crystals with subhedral to euhedral morphology that preserve the inner part of the cuticle. **(d)** Spectrum of micrometric crystals, possible galena, or iron sulfate enriched in Pb. **(e)** Micrograph of porous textured crystals, with euhedral crystals **(f - g)** Spectrum of porous texture. **(h)** Structures suggestive of biological origin. **(i)** EDS spectrum of organic material. **(j)** Muscle fiber **(k)** Spectrum of muscle fiber showing calcium phosphate present on the surface of the fibers.

Figure 13. SEM-EDS of sample GP/1E10501. **(a)** General view of the hind leg region of the fossil showing fine projections distributed across the surface. **(b)** Magnification of the same area, highlighting the dense and aligned pattern of these structures. **(c)** High-magnification detail revealing a single elongated and pointed structure, with morphology consistent with preserved cuticular trichomes or spines. **(d)** General view of the insect's abdominal region showing parallel muscle bundles with a regular linear pattern. **(e)** Detail of the bundles showing slightly rough surface texture and micrometric spacing between fibers. **(f)** Higher magnification revealing fiber individualization with well-defined contours, consistent with preserved filamentous muscle morphology. **(g)** EDS of muscle fibers. **(h)** Corresponding EDS spectrum showing a predominance of oxygen (O), calcium (Ca), and phosphorus (P), with the presence of sulfur (S) and iron (Fe), suggesting mineralization by calcium phosphates and a contribution from iron sulfates.

Figure 14. SEM-EDS of sample GP/1E10836. **(a)** Sample with measurement areas marked: blue – wing; red – thoracic region; and green – abdominal region. **(b)** Framboidal pyrite

preserving the veins of the left wing highlighted by the blue rectangle in “a”. **(c)** Juxtaposition of euhedral microcrystals, forming a rhombohedral texture. **(d)** Cluster of placoid crystals organized in rosette habits, covered by crystals in a finely crystalline mineral phase. **(e)** Well-developed rosette with preserved radial organization and defined contours. **(f)** Granular, prismatic, and acicular nanocrystals cover previously formed rosette structures, suggesting a process of surface alteration or late-stage diagenetic remineralization. The rosettes are indicated by a red dotted rectangle. **(g-h)** Pyrite framboids covered by structures outlined with a red dotted rectangle, which may represent mineralogical transitions to iron sulfates or exopolysaccharides (EPS) secreted by sulfate-reducing bacteria. **(i)** External ornamentation of exoskeleton preserved by pyrite framboids. **(j - k)** Euhedral crystals. **(l)** SEM-EDS analysis of crystals covering rosettes. **(k)** Spectra of iron sulfate. **(i)** SEM-EDS of euhedral crystals. **(m)** EDS spectrum of the euhedral crystals.

Figure 15. Integrative taphonomic model representing the mineralization processes in fossilized insects from the Crato Formation. Schematic representation of an insect with enlarged zones (a–d), showing the spatial distribution and interaction between different mineral phases throughout preservation. **(a)** Initial composition of the organism and taphonomic microenvironment, with abundant presence of organic matter, primary calcium phosphate, chemical elements and salts dissolved in the interstitial water, crossing the sulfate reduction zone to the interior of the carcass. **(b)** Internal mineralization by FeS_2 (iron sulfide), associated with phosphorus and barium. **(c)** Oxidative transition zone, where the oxidation of framboidal pyrite promotes the release of elements previously retained during its primary precipitation, giving rise to sulfated mineral phases, mainly from the jarosite group. **(d)** Final stage of preservation after stabilization of the paleoenvironment, with iron sulfates preserving soft tissues, calcium phosphate on muscle fibers and relic pyrite crystals inside the fibers. Some parts of the organs were preserved by barium sulfate and non-oxidized framboidal pyrite, restricted to the cuticle, in addition to the residual presence of organic matter.

Sumário

INTRODUÇÃO

A Formação Crato é considerada um depósito do tipo *Konservat Lagerstätte*. O termo *Fossil-Lagerstätte* foi criado por Seilacher (1970), definido como 'corpos rochosos que, em qualidade e quantidade, preservam uma quantidade incomum de informação paleontológica'. Dentro dessa classificação, os *Konservat-Lagerstätten* se destacam pela preservação excepcional de tecidos moles, quitina e esqueletos articulados, em contraste com os *Konzentra Lagerstätten*, definidos pelo acúmulo de restos desarticulados. Mais recentemente, Kimmig & Schiffbauer (2024) propuseram uma definição moderna e utilitária de *Konservat-Lagerstätten*, que estabelece critérios objetivos: (i) a preservação morfológica excepcional de fósseis completos ou quase completos, incluindo tecidos moles; (ii) a exigência de que ao menos 5% dos fósseis do depósito apresentem preservação excepcional; e (iii) a caracterização do modo mineralógico e tafonômico predominante, como fosfatização, piritização ou silicificação. Essa abordagem permite padronizar comparações entre depósitos.

Os fósseis excepcionalmente preservados são particularmente encontrados no Membro Nova Olinda, que representa um lago hipersalino, estratificado de fundo anóxico. Sob tais condições ambientais, que reforçam o desenvolvimento microbiano e a preservação de tecidos moles (Varejão et al., 2019b), onde comunidades microbianas puderam se estabelecer, A ocorrência de microbialitos, neste caso, foi registrada em associação a condições interpretadas como de aumento progressivo da lâmina d'água (Assine et al., 2014a, 2014b; Fambrini et al., 2020; Varejão et al., 2021a, 2021b). A presença de pseudomorfos de halita e de gipsita nas camadas revela episódios de hipersalinidade das águas de fundo sob condições extremamente secas do ambiente durante a deposição da Formação Crato (Heimhofer e Martill, 2007).

A paleobiodiversidade do Membro Nova Olinda inclui insetos, crustáceos, aracnídeos, miriápodes, peixes, anfíbios, tartarugas, lagartos, crocodilomorfos, pterossauros, dinossauros, pássaros, cobras, além de representantes do reino vegetal como pteridófitas, coníferas, gnetófitas e angiospermas (Martill e Wilby, 1993; Martill e Bechly, 2007; Martill et al., 2007) que oferecem uma janela única para o estudo de informações morfológicas e ecológicas raramente preservadas no registro fóssil (Osés et al., 2016 e 2017).

O estudo dos processos de fossilização constitui a ciência da Tafonomia, sendo fundamental para se compreender o enviesamento dos processos geológicos na morfologia

e composição originais dos organismos (*e.g.*, Gueriau et al., 2016). Para isso, a fidelidade de preservação morfológica e a composição mineralógica e química dos fósseis são caracterizadas por técnicas da Física e Química, preferencialmente não destrutivas, constituindo a Paleometria (Riquelme et al., 2009; Delgado et al., 2014; Gomes et al., 2019; Prado et al., 2021). Dentre as técnicas paleométricas, a microscopia eletrônica de varredura, a microespectroscopia Raman e a fluorescência de raios-X (XRF) têm sido largamente utilizadas para a caracterização de fósseis. Elas são complementares, pois enquanto o imageamento por microscopia eletrônica e técnicas associadas (*e.g.*, espectroscopia por energia dispersiva) permitem a investigação da morfologia, arranjo e composição química de cristais de minerais, a microespectroscopia Raman possibilita a identificação dos minerais e compostos orgânicos e XRF permite a caracterização da composição elementar (Osés et al., 2016; Osés et al., 2017).

Esta pesquisa investigou a preservação excepcional de insetos fósseis na Formação Crato, explorando processos microbianos na fossilização dos organismos. Assim, buscou-se entender, preliminarmente, a composição química e a mineralogia dos fósseis em função do tipo de rocha em que são encontrados, com ênfase na preservação em calcário cinza (*grey limestone*) *sensu* Osés et al. (2017). Os resultados apresentados contribuem para a compreensão de processos tafonômicos e paleoambientais responsáveis pela preservação desses fósseis de insetos. Essa descoberta possibilitou o refinamento de modelos de preservação propostos anteriormente (*e.g.*, Osés et al., 2017), que consideravam apenas preservação por querogenização no calcário cinza.

CONTEXTO GEOLÓGICO

A Formação Crato, situada na bacia sedimentar do Araripe, é um dos registros paleobiológicos continentais mais completos do período Cretáceo, aflorante principalmente no estado do Ceará (Assine, 2007) (Fig. 1). A formação dessa bacia está intrinsecamente ligada aos eventos tectônicos associados à abertura do Atlântico Sul (Matos, 1992). Durante os estágios *pós-rift*, ocorreu a deposição de carbonatos em um sistema lacustre com episódios de hipersalinidade, resultando na formação dos calcários laminados característicos da Formação Crato (Assine et al., 2014ab; Fambrini et al., 2020; Varejão et al., 2021b).

A Formação Crato é datada como sendo do estágio Aptiano final (Rios-Netto et al., 2012; Arai e Assine, 2018 e 2020; Melo et al., 2020; Coimbra e Freire, 2021). As camadas finamente laminadas de calcário da unidade são distintas e revelam um paleoambiente

lacustre com mudanças sazonais e um gradiente semiárido da base ao topo parte do Cretáceo Inferior, dividido em quatro membros: Caldas, Jamacaru, Casa de Pedra e Nova Olinda (Martill e Heimhofer, 2007). Esta unidade engloba seis associações de fácies (FA-3 a FA-8) com base na geometria, textura, estruturas sedimentares, paleocorrentes, conteúdo fóssil, tafonomia e dados geoquímicos (Varejão et al., 2021b).

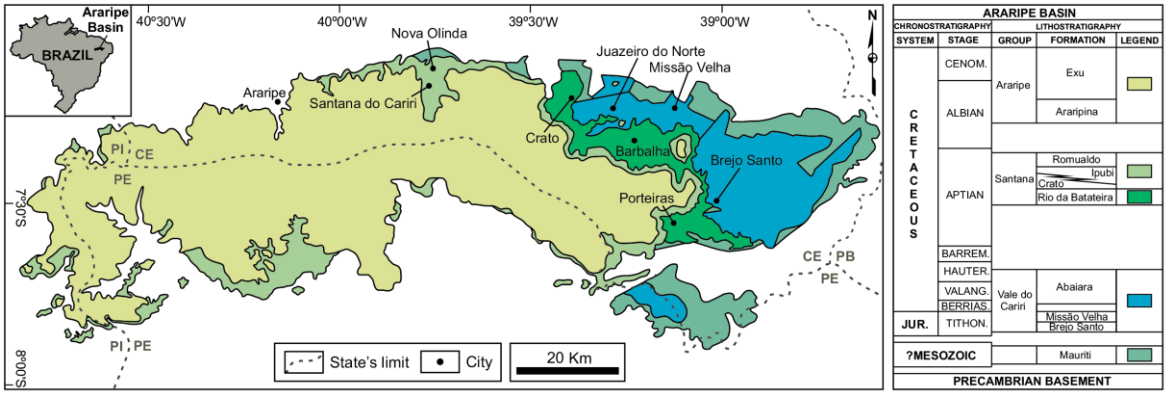

Figura 1. Os fósseis de insetos analisados são provenientes da Formação Crato (Grupo Santana), de idade Aptiana final. PI: Estado do Piauí; PE: Estado de Pernambuco; CE: Estado do Ceará; PB: Estado da Paraíba; JUR.: Jurássico; TITHON.: Tithoniano; BERRIAS.: Berriasiano; VALANG.: Valanginiano; HAUTER.: Hauteriviano; BARREM.: Barremiano; CENOM.: Cenomiano. A nomenclatura das unidades litoestratigráficas segue Assine et al. (2014) e Carvalho et al. (2024a, b). O mapa geológico foi adaptado de Assine (2007) e Dias et al. (2022).

Estado da Arte sobre a preservação de insetos fósseis da Formação Crato (Cretáceo), Brasil.

A paleoentomofauna da Formação Crato representa um dos mais completos depósitos registrados do Cretáceo no mundo. Até o ano de 2018, foram descritas 79 espécies de insetos fósseis, distribuídas em 121 famílias (Moura-Júnior et al., 2018). Os insetos fósseis são notáveis pela preservação excepcional (Martill e Wilby, 1993; Assine et al., 2014a) de estruturas delicadas de detalhes morfológicos do exoesqueleto que incluem escamas, sensilas, omatídias e estruturas superficiais da cutícula, além de tecidos originalmente moles, como fibras musculares e estruturas genitais (Barling et al., 2015; Osés et al., 2016; Dias e Carvalho, 2020) sendo fundamentais para a compreensão da diversificação de insetos sociais e da coevolução de insetos e angiospermas (Labandeira e Eble, 2000; Soares et al., 2013). Estes insetos são encontrados em calcários finamente laminados originados por ação microbiana (Catto et al., 2016; Warren et al., 2017; Varejão et al., 2019). Os calcários da Formação Crato são pouco intemperizados, com alta

continuidade lateral, geometria tabular, de granulometria fina a muito fina, com laminações planas e onduladas bem marcadas e variação vertical de cor amarelada a cinza. No plano de estratificação, estes litotipos podem exibir estruturas sedimentares induzidas por atividade microbiana (MISS) (Dias e Carvalho, 2022).

Estudos pioneiros foram realizados a fim de investigar os processos geobiológicos envolvidos na preservação, muitas vezes tridimensional, desses insetos (Barling et al., 2015; Osés et al., 2016). Basicamente, os fósseis são preservados por dois mecanismos distintos, (1) óxi-/hidróxidos de ferro formados após a oxidação de pirita (sulfeto de ferro), sendo essa condição frequente nos calcários beges (*beige limestone*) e (2) por transformação da matéria orgânica em hidrocarbonetos (querogenização), típico dos calcários cinzas (*grey limestone*) (Bezerra et al., 2018; Dias et al., 2023). Algumas replicações de morfologias internas também podem ocorrer por fosfatização (Osés et al., 2016 e 2017). Portanto, o modelo piritização-querogenização que foi observado inicialmente em vertebrados (Osés et al., 2017) pode ser atribuído também aos insetos fósseis da Formação Crato (Bezerra et al., 2018 e 2021; Dias e Carvalho, 2020).

Os tipos de preservação dos fósseis da Formação Crato fornecem informações sobre as condições paleoambientais do ambiente deposicional (Osés et al., 2017, Varejão et al., 2019, Dias e Carvalho, 2022). No que diz respeito aos fósseis de ortópteros, por exemplo, Dias e Carvalho (2022) propuseram duas condições paleoambientais e paleoclimáticas diferentes com base na análise de sua preservação, especialmente da cutícula: os fósseis piritizados tridimensionais são encontrados predominantemente em *beige limestone*; e os fósseis bidimensionais querogenizados, são preservados como um microfilme carbonáceo amorfo e principalmente associados a *grey limestone*. Fósseis piritizados podem indicar condições climáticas mais secas em um ambiente lacustre raso, salino e estagnado. Os fósseis querogenizados, por outro lado, estariam associados a condições mais úmidas, com o ambiente lacustre suscetível a grandes descargas de sedimentos trazidas pelos influxos dos rios, o que aumentava a profundidade e diminuia a salinidade da água sem uma forte influência dos tapetes microbianos. As condições ambientais e climáticas associadas aos calcários amarelados são mais favoráveis à formação e disseminação de esteiras microbianas, aumentando diretamente o potencial de preservação excepcional de fósseis (Dias et al., 2023).

Em ambos os processos de fossilização, observações detalhadas revelaram a presença de evidências de atividade microbiana em íntima associação com os fósseis, sugerindo que

a preservação excepcional desses insetos é resultado de um complexo processo de organomineralização influenciado por essas esteiras (Delgado et al., 2014; Barling et al., 2015; Osés et al 2016 e 2017; Dias e Carvalho 2021; Dias e Carvalho, 2022; Dias et al., 2023). Segundo Seilacher et al. (1985), as esteiras microbianas são um dos principais fatores responsáveis pela preservação excepcional de fósseis, incluindo tecidos moles. Este processo envolve o encapsulamento dos restos orgânicos por biofilmes após a morte do organismo. A estagnação e o soterramento rápido, por sua vez, são processos que também desempenham papéis cruciais na preservação, mas em contextos distintos. A influência das esteiras microbianas como um fator importante na preservação de tecidos moles em fósseis pôde ser demonstrada pelos estudos de Iniesto et al. (2015 e 2021) e de Schiffbauer et al. (2014). Com base nos dados de Dupraz et al. (2009), Schiffbauer et al. (2014), Muscente et al. (2015), e Varejão (2019), propõe-se então que o modelo para explicar a preservação de insetos fósseis seja controlado pelo papel das zonas microbianas estratificadas geoquimicamente na preservação. Por fim, os processos de mineralização associados a esteiras microbianas, como a fosfatização e a piritização, que ocorreram nos insetos da Formação Crato, são discutidos como processos significativos na preservação de tecidos moles, com estudos de Briggs (2003) e Muscente et al. (2015, 2017) que fornecem suporte a esta hipótese.

Os insetos fósseis originalmente piritizados possuem tridimensionalidade evidente (Dias e Carvalho., 2022), apresentam coloração marrom-alaranjada, resultante da substituição da pirita por óxidos e hidróxidos de ferro, como hematita, goethita e limonita (Menon e Martill, 2007; Delgado et al., 2014; Barling et al., 2015; Osés et al., 2016) sendo semelhantes aos insetos da biota de Jehol, China (Wang et al., 2012). A mineralogia é essencialmente de pseudomorfos de pirita framboidal (Osés et al., 2016), ocasionalmente recobertos por texturas que indicam a presença de substâncias poliméricas extracelulares (EPS) (Delgado, et al., 2014; Osés et al., 2016; Dias e Carvalho, 2022). A preservação de tecidos moles e de estruturas extremamente delicadas dos insetos fósseis foram favorecidas pela precipitação eodiagenética da pirita, em condições deposicionais de baixa energia, em ambientes anóxicos e sulfídicos, onde a decomposição dos organismos é realizada por bactérias sulfato-redutoras (BSR). Essas bactérias utilizam sulfato para respiração anaeróbia, produzindo sulfeto de hidrogênio como subproduto. Esse sulfeto reage com ferro dissolvido no ambiente, precipitando como pirita (FeS_2). Esse processo é então favorecido pela presença de esteiras microbianas, que criam um microambiente anóxico, que encapsulam os

restos orgânicos, protegendo-os da decomposição rápida e favorecendo a precipitação da pirita pelas BSR (Osés et al., 2016; 2017).

A pirita pode substituir diretamente os tecidos orgânicos ou preencher cavidades internas dos fósseis, preservando detalhes finos da morfologia original (Osés et al., 2016; Delgado et al., 2014; Barling et al., 2015). Os framboides de pirita apresentam um gradiente no tamanho desde o exoesqueleto até a matriz (Delgado et al., 2014). Os framboides maiores que replicam o exoesqueleto se formam a partir da taxa de difusão de íons mais intensa, enquanto os microframboides que preenchem o interior das carcaças são resultado da redução do influxo de íons devido à barreira imposta pelo exoesqueleto. Foi proposto que a preservação dos insetos foi influenciada pela composição química original do exoesqueleto, especialmente a quitina, que oferece uma afinidade química específica, facilitando a incorporação de Cu e Zn no exoesqueleto (Osés et al., 2016).

Os insetos fósseis querogenizados são mais delicados, geralmente bidimensionais, e exibem uma coloração escura, com altas contagens de carbono, o que indica a retenção de componentes orgânicos originais (Barling et al., 2015; Osés et al., 2017; Bezerra et al. 2018 e 2021; Dias e Carvalho, 2020 e 2022). A preservação por querogenização ocorre pela formação de hidrocarbonetos cíclicos e componentes alifáticos que passaram por transformação química do material orgânico original, na formação do registro fóssil (McNamara et al., 2013; Schiffbauer et al., 2014). Esse processo de fossilização ocorre de maneira distinta à proposta em *beige limestone*, preservando tecidos delicados, porém biologicamente mais resistentes, como fibras musculares e tecidos tegumentares. Este tipo de preservação está associado ao tempo em que esses fósseis foram expostos a zona de metanogênese (Schiffbauer et al., 2014), condicionada por um soterramento mais rápido (em relação às amostras piritizadas) em condições anóxicas de zonas não-sulfídicas, ricas em matéria orgânica associadas a biofilmes capazes de transformar essa matéria orgânica em metanos e outros compostos, incluindo o querogênio (Osés et al., 2017). Notavelmente, quando comparado aos espécimes que foram mineralizados por pirita, que possuem alta fidelidade às estruturas biológicas internas e externas originais, a qualidade de preservação dos insetos querogeneizados é consistentemente inferior (Bezerra et al., 2021; Dias e Carvalho, 2022).

REFERÊNCIAS BIBLIOGRÁFICAS

Arai, M., & Assine, M. L. (2018). Novas datações palinológicas da Formação Romualdo (Bacia do Araripe): sua implicação no arcabouço estratigráfico da sucessão aptiano–albiano das bacias brasileiras. In XXXIX Congresso Brasileiro de Geologia (p. 1306). Rio de Janeiro: SBG.

Arai, M., & Assine, M. L. (2020). Chronostratigraphic constraints and paleoenvironmental interpretation of the Romualdo Formation (Santana Group, Araripe Basin, Northeastern Brazil) based on palynology. *Cretaceous Research, 116*, 104610. https://doi.org/10.1016/j.cretres.2020.104610

Assine, M. L., Perinotto, J. D. J., Custódio, M. A., Neumann, V. H., Varejão, F. G., & Mescolotti, P. C. (2014). Sequências deposicionais do andar Alagoas da Bacia do Araripe, nordeste do Brasil. *Boletim de Geociências da PETROBRAS, 22*(1), 3-28.

Barling, N., Martill, D. M., Heads, S. W., & Gallien, F. (2015). High fidelity preservation of fossil insects from the Crato Formation (Lower Cretaceous) of Brazil. *Cretaceous Research, 52*(B), 605-622.

Bezerra, F. I., Silva, J. H. D., Paula, A. J. D., Oliveira, N. C., Paschoal, A. R., Freire, P. T. C., & Mendes, M. (2018). Throwing light on an uncommon preservation of Blattodea from the Crato Formation (Araripe Basin, Cretaceous), Brazil.

Bezerra, F. I., Solórzano-Kraemer, M. M., & Mendes, M. (2021). Distinct preservational pathways of insects from the Crato Formation, Lower Cretaceous of the Araripe Basin, Brazil. *Cretaceous Research, 118*, 104631.

Catto, B., Jahnert, R. J., Warren, L. V., Varejão, F. G., & Assine, M. L. (2016). The microbial nature of laminated limestones: Lessons from the Upper Aptian, Araripe Basin, Brazil. *Sedimentary Geology, 341*, 304-315.

Coimbra, J. C., & Freire, T. M. (2021). Age of the Post-rift Sequence I from the Araripe Basin, Lower Cretaceous, NE Brazil: Implications for spatio-temporal correlation. *Revista Brasileira de Paleontologia, 24*(1), 37-46.

Delgado, A. de O., Buck, P. V., Osés, G. L., Ghilardi, R. P., Rangel, E. C., & Pacheco, M. L. A. F. (2014). Paleometry: A brand-new area in Brazilian science. *Materials Research, 17*, 1434-1441.

Dias, J. J., & de Souza Carvalho, I. (2020). Remarkable fossil crickets' preservation from Crato Formation (Aptian, Araripe Basin), a Lagerstätten from Brazil. *Journal of South American Earth Sciences, 98*, 102443.

Dias, J. J., & de Souza Carvalho, I. (2022). The role of microbial mats in the exquisite preservation of Aptian insect fossils from the Crato Lagerstätte, Brazil. *Cretaceous Research, 130*, 105068.

Dias, J. J., de Souza Carvalho, I., Buscalioni, Á. D., Umamaheswaran, R., López-Archilla, A. I., Prado, G., & de Andrade, J. A. F. G. (2023). Mayfly larvae preservation from the Early

Cretaceous of Brazilian Gondwana: Analogies with modern mats and other Lagerstätten. *Gondwana Research, 124*, 188-205.

Fambrini, G. L., Silvestre, D. D. C., Barreto Junior, A. M., & Silva-Filho, W. F. D. (2020). Estratigrafia da Bacia do Araripe: estado da arte, revisão crítica e resultados novos. *Revista do Instituto de Geociências - USP, Geologia USP, Série Científica, 20*(4), 16-212. http://doi.org/10.11606/issn.2316-9095.v20-163467

Freire, P. T. C., Silva, J. H., Sousa-Filho, F. E., Abagaro, B. T., Viana, B. C., Saraiva, G. D., et al. (2014). Vibrational spectroscopy and X-ray diffraction applied to the study of Cretaceous fish fossils from Araripe Basin, Northeast of Brazil. *Journal of Raman Spectroscopy, 45*, 1225-1229.

Gomes, A. L. S., et al. (2019). Paleometry as a key tool to deal with paleobiological and astrobiological issues: Some contributions and reflections on the Brazilian fossil record. *International Journal of Astrobiology*, 1-15. https://doi.org/10.1017/S1473550418000538

Gueriau, P., Bernard, S., & Bertrand, L. (2016). Advanced synchrotron characterization of paleontological specimens. *Elements, 12*, 45-50.

Iniesto, M., Gutiérrez-Silva, P., Dias, J. J., Carvalho, I. S., Buscalioni, A. D., & López-Archilla, A. I. (2021). Soft tissue histology of insect larvae decayed in laboratory experiments using microbial mats: Taphonomic comparison with Cretaceous fossil insects from the exceptionally preserved biota of Araripe, Brazil. *Palaeogeography, Palaeoclimatology, Palaeoecology, 564*, 110156.

Iniesto, M., Zeyen, N., López-Archilla, A. I., Bernard, S., Buscalioni, Á. D., Guerrero, M. C., & Benzerara, K. (2015). Preservation in microbial mats: Mineralization by a talc-like phase of a fish embedded in a microbial sarcophagus. *Frontiers in Earth Science, 3*, 51.

Labandeira, C., & Eble, G. J. (2000). The Fossil Record of Insect Diversity and Disparity. In J. Anderson et al. (Eds.), *Gondwana Alive: Biodiversity and the Evolving Biosphere*. Witwatersrand University Press. Available at: http://www.santafe.edu/media/workingpapers/00-08-044.pdf (Accessed: 01 March 2011).

Lima, K. D. A., Moraes, M. N. C. M., & Martins-Neto, R. G. (2007). The diversity of the Santana Formation paleoentomofauna (Lower Cretaceous, Northeast Brazil). 8° Congresso de Ecologia do Brasil, Caxambu. Available at: http://seb-ecologia.org.br/viiiceb/pdf/528.pdf (Accessed: 01 March 2011).

Martill, D. M., & Bechly, G. (2007). Introduction to the Crato Formation. In D. M. Martill, G. Bechly, & R. F. Loveridge (Eds.), *The Crato fossil beds of Brazil: Window into an ancient world* (pp. 3-7). Cambridge University Press.

Martill, D. M., & Wilby, P. (1993). Stratigraphy. In D. M. Martill (Ed.), *Fossils of the Santana and Crato Formations, Brazil* (pp. 20-50). Dorchester: Palaeontological Association.

Martill, D. M., Loveridge, R., & Heimhofer, U. (2007). Halite pseudomorphs in the Crato Formation (Early Cretaceous, late Aptian–early Albian), Araripe Basin, northeast Brazil: Further evidence for hypersalinity. *Cretaceous Research, 28*(4), 613-620.

Martill, D., & Heimhofer, U. (2007). Stratigraphy of the Crato formation. In D. M. Martill, G. Bechly, & R. F. Loveridge (Eds.), *The Crato fossil beds of Brazil: Window into an ancient world* (pp. 15-30). Cambridge University Press.

Matos, R. M. D. (1992). The Northeast Brazilian Rift System. *Tectonics, 11*, 766-791.

McNamara, M. E., Orr, P. J., Kearns, S. L., Alcalá, L., Anadón, P., & Peñalver Mollá, E. (2009). Soft-tissue preservation in Miocene frogs from Libros, Spain: Insights into the genesis of decay microenvironments. *Palaios, 24*(2), 104-117. https://doi.org/10.2110/palo.2008.p08-017r

Melo, R. M., Guzmán, J. G., Lima, D. S. A., Piovesan, E. K., Neumann, V. H. M. L., & Sousa, A. J. (2020). New marine data and age accuracy of the Romualdo Formation, Araripe Basin, Brazil. *Scientific Reports, 10*, 15779. https://doi.org/10.1038/s41598-020-72789-8

Menon, F., & Martill, D. (2007). Taphonomy and preservation of Crato Formation Arthropods. In *The Crato fossil beds of Brazil: Window into an ancient world* (pp. 79-96). Cambridge University Press.

Muscente, A. D., Hawkins, A. D., & Xiao, S.(2015). Fossil preservation through phosphatization and silicification in the Ediacaran Doushantuo Formation (South China): A comparative synthesis. *Palaeogeography, Palaeoclimatology, Palaeoecology, 434*, 46-62.

Muscente, A. D., Schiffbauer, J. D., Broce, J., Laflamme, M., O'Donnell, K., Boag, T. H., ... & Xiao, S. (2017). Exceptionally preserved fossil assemblages through geologic time and space. *Gondwana Research, 48*, 164-188.

Osés, G. L., Petri, S., Becker-Kerber, B., Romero, G. R., de Almeida Rizzutto, M., Rodrigues, F., ... & Pacheco, M. L. A. F. (2016). Deciphering the preservation of fossil insects: A case study from the Crato Member, Early Cretaceous of Brazil. *PeerJ, 4*, e2756.

Osés, G. L., Petri, S., Voltani, C. G., Prado, G. M., Galante, D., Rizzutto, M. A., ... & Pacheco, M. L. A. F. (2017). Deciphering pyritization-kerogenization gradient for fish soft-tissue preservation. *Scientific Reports, 7*(1), 1468.

Prado, G., Arthuzzi, J. C. L., Osés, G. L., Callefo, F., Maldanis, L., Sucerquia, P., ... et al. (2021). Synchrotron radiation in palaeontological investigations: Examples from Brazilian fossils and its potential to South American palaeontology. *Journal of South American Earth Sciences*. https://doi.org/10.1016/j.jsames.2020.102973

Rios-Netto, A., Regali, M. D. S. P., de Souza Carvalho, I., & de Freitas, F. I. (2012). Palinoestratigrafia do intervalo Alagoas da Bacia do Araripe, nordeste do Brasil. *Revista Brasileira de Geociências, 42*(2), 331-342.

Riquelme, F., Ruvalcaba-Sil, J. L., & Alvarado-Ortega, J. (2009). Palaeometry: Non-destructive analysis of fossil materials. *Boletín de la Sociedad Geológica Mexicana, 61*(2), 177-183.

Schiffbauer, J. D., Xiao, S., Cai, Y., Wallace, A. F., Hua, H., Hunter, J., ... & Kaufman, A. J. (2014). A unifying model for Neoproterozoic–Palaeozoic exceptional fossil preservation through pyritization and carbonaceous compression. *Nature Communications, 5*(1), 5754.

Seilacher, A. (1985). Sedimentary structures and evolution of the Cambrian biota. In H. B. Whittington & S. Conway Morris (Eds.), *The Cambridge History of Early Life* (pp. 123-144). Cambridge University Press.

Varejão, F. G., Silva, V. R., Assine, M. L., Warren, L. V., Matos, S. A., Rodrigues, M. G., Fürsich, F. T., & Simões, M. G. (2021a). Marine or freshwater? Accessing the paleoenvironmental parameters of the Caldas Bed, a key marker bed in the Crato Formation (Araripe Basin, NE Brazil). *Brazilian Journal of Geology, 51*(1). https://doi.org/10.1590/2317-4889202120200009

Varejao, F. G., Warren, L. V., Simoes, M. G., Buatois, L. A., Mangano, M. G., Bahniuk Rumbelsperger, A. M., & Assine, M. L. (2021b). Mixed siliciclastic–carbonate sedimentation in an evolving epicontinental sea: Aptian record of marginal marine settings in the interior basins of north-eastern Brazil. *Sedimentology, 68*(5), 2125-2164.

Varejão, F. G., Warren, L. V., Simões, M. G., Fürsich, F. T., Matos, S. A., & Assine, M. L. (2019). Exceptional preservation of soft tissues by microbial entombment: Insights into the taphonomy of the Crato Konservat-Lagerstätte. *Palaios, 34*(7), 331-348. https://doi.org/10.2110/palo.2019.041

Wang, B., Zhao, F., Zhang, H., Fang, Y., & Zheng, D. (2012). Widespread pyritization of insects in the Early Cretaceous Jehol Biota. *Palaios, 27*(10), 707-711.

HIPÓTESES

A preservação excepcional de insetos fósseis na Formação Crato está diretamente relacionada à presença de esteiras microbianas que contribuíram para a piritização e fossilização dos organismos. A composição mineralógica dos fósseis pode variar dependendo do tipo de rocha em que são encontrados, com fósseis piritizados (calcário bege – BL) apresentando uma preservação com maior grau de detalhes em relação àqueles preservados por querogênio (calcário cinza – GL).

Portanto, hipotetizou-se que (1) a piritização desempenhou um papel central na preservação excepcional de insetos nas rochas de calcário-cinza da Formação Crato, representando um fenômeno tafonômico até então não documentado neste tipo de rocha; (2)

tecidos moles se preservaram por piritização; e, (3) microambientes diagenéticos controlam as assinaturas tafonômicas em micro e nano escalas.

OBJETIVOS

Investigar os processos de preservação de fósseis de insetos no calcário "GL" da Formação Crato, a fim de compreender os mecanismos tafonômicos que atuaram em sua fossilização e propor um modelo atualizado de preservação para esse contexto.

Objetivos específicos

1. Caracterizar as composições mineralógica, química e orgânica dos fósseis e da matriz rochosa, visando identificar os principais componentes responsáveis pela preservação.

2. Investigar a preservação de tecidos moles nos fósseis de insetos, com o objetivo de avaliar sua contribuição para a compreensão dos mecanismos tafonômicos.

3. Refinar e propor um modelo de preservação para os fósseis da Formação Crato, considerando a atuação de processos como fosfatização, piritização e sulfatização, de modo a aprofundar o entendimento das condições que favoreceram a fossilização em calcário "GL".

MATERIAIS E MÉTODOS

As amostras analisadas possuem código "GP/1E", que indica fósseis de invertebrados depositados na Coleção Científica de Paleontologia do Instituto de Geociências da Universidade de São Paulo (IGc-USP) (Figs. 2). Não foram necessárias permissões para o estudo descrito, uma vez que este foi realizado após as amostras terem sido depositadas na referida coleção científica. Os resultados aqui apresentados consistem na análise e cinco espécimes de fósseis de insetos da Formação Crato, Aptiano da Bacia do Araripe: GP/1E 11237c (Fig. 1a), GP/1E 10501 (Fig. 1b), GP/1E 10836 (Fig. 1c), GP/1E 10609 (Fig. 1d) e GP1E 10776 (Fig. 1f).

As fotografias foram realizadas utilizando-se microscópio Olympus DSX110 microscope, no Laboratório de Estudos Paleobiológicos, Instituto de Geociências da Universidade de São Paulo (IGc-USP).

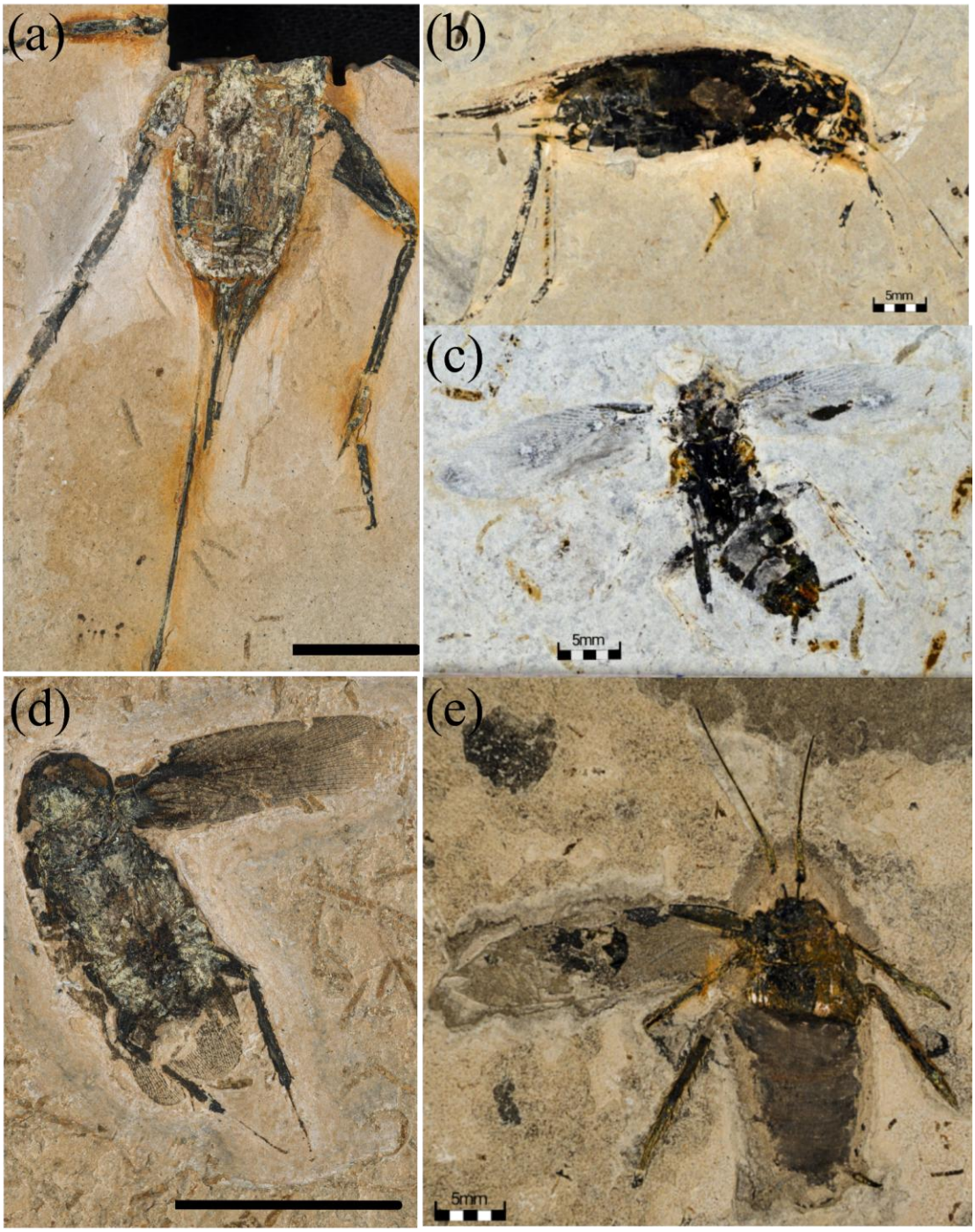

Figura 1. Amostras analisadas neste estudo. A. Amostra GP/1E11237c (Orthoptera). B. Amostra GP/1E 10501 (Ortheoptera); C. Amostra GP/1E 10836(Blattodea); D. Amostra GP/1E10609 (Blattodea); E. Amostra GP/1E 10776 (Blattodea).

FLUORESCÊNCIA DE RAIO X POR DISPERSÃO DE ENERGIA

ASPECTOS TEÓRICOS GERAIS

A técnica de Fluorescência de Raios X (EDXRF, sigla em inglês de *X-Ray Fluorescence*) constitui uma ferramenta analítica não destrutiva, usada para determinar a composição elementar de materiais. Esta técnica é aplicável em múltiplos contextos, incluindo a análise de materiais geológicos e arqueológicos. O princípio físico do EDXRF baseia-se na interação entre fótons de alta energia (provenientes de uma fonte de raios X) e os átomos presentes na amostra, processo que induz o efeito fotoelétrico (Fig. 2). Quando um fóton de raios X atinge um átomo, ele pode expulsar um elétron de uma das camadas internas do átomo, levando à emissão de energia quando um elétron de uma camada superior ocupa a vaga deixada. Essa liberação de raios X é conhecida como fluorescência e cada emissão durante esse rearranjo eletrônico tem uma energia específica, que é captada por um detector, e indica qual elemento atômico foi excitado, permitindo a identificação e a quantificação desse elemento presente na amostra. Sua grande utilidade vem da capacidade de medir múltiplos elementos ao mesmo tempo, *in situ*, não sendo necessária a destruição da amostra e nem uma grande quantidade dela.

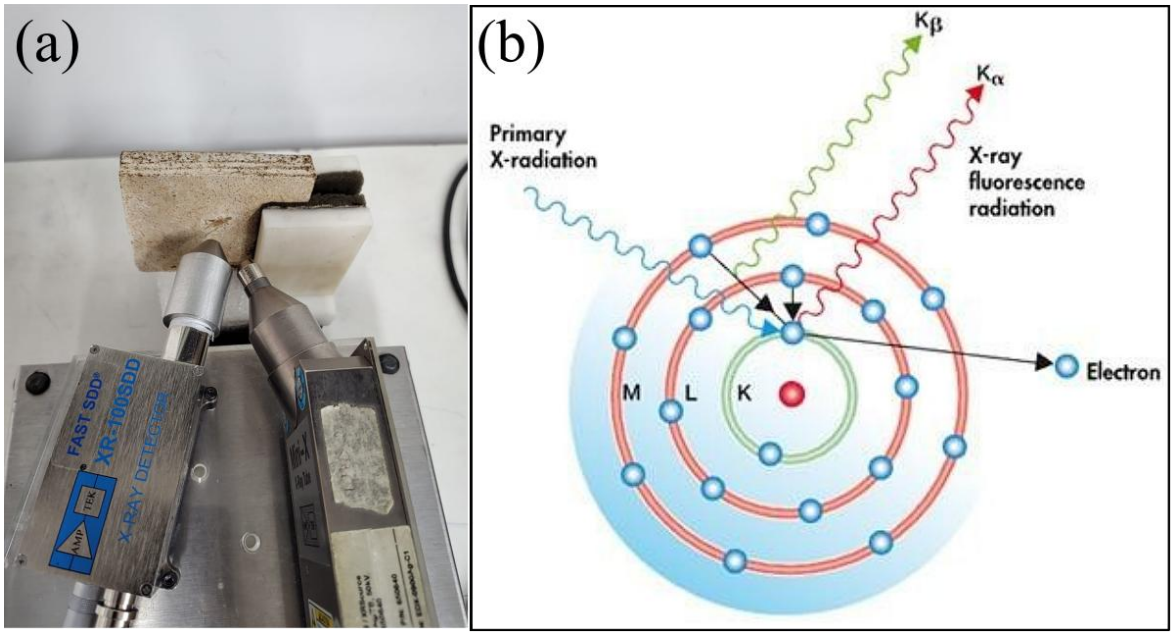

Figura 2. Equipamento e funcionalidade do XRF. A. Sistema de fluorescência de raio-x (XRF) com amostras sob análises. Foto: Sabrina Belatto. B. ilustração do efeito fotoelétrico. Fonte: Google imagens.

MÉTODO EMPREGADO

A análise de fluorescência de raios X por dispersão de energia (EDXRF) foi empregada aos fósseis com o objetivo de obter a caracterização elementar e distribuição desses elementos em diferentes pontos das amostras, tomando como critério diferentes áreas das amostras: pontos mais claros (bege) e mais escuros (marrom à preto) no interior do fóssil; pontos próximos ao exoesqueleto, na margem entre fóssil-matriz; e pontos na matriz. A EDXRF foi utilizada primeiramente, para selecionar as amostras e pontos que iriam para a análise de microespectroscopia Raman.

As medidas foram realizadas em equipamento portátil de EDXRF disponível no Laboratório de Arqueometria e Ciências Aplicadas ao Patrimônio Cultural (LACAPC), do Instituto de Física da USP (IF-USP). Esse sistema consiste em um tubo de raios X de ânodo de prata mini (Amptek) e um detector *fast silicon drift detector* (SDD) de 125eV FWHM para a linha de 5.9KeV do Mn. As medições foram realizadas com uma tensão de 30kV e uma corrente de tubo de 5μA, com um tempo de excitação/detecção de 100s.

A visualização dos espectros medidos, a identificação dos elementos químicos em cada medida (espectro), o *fitting* dos espectros e a determinação das contagens foram realizados no software WinQxas. Ainda utilizando o mesmo software, em conjunto com o software qxasreader, foram gerados arquivos Excel com a contagem dos elementos em cada medida na amostra.

Após a identificação dos elementos em todos os pontos medidos, os softwares Spectragryph 1.2, Excel e Inkscape *Draw Freely* v.1.3.2, foram utilizados para gerar versão em log dos espectros e elaborar figuras, assim como para construir gráficos de barras com as contagens *versus* medidas para diferentes elementos, para posteriores análises comparativas dos espectros.

Para o tratamento estatístico dos dados, utilizamos a programação R, aplicando o teste de normalidade Shapiro-Wilk e, posteriormente, o teste de correlação de Spearman para variáveis não-paramétricas, gerando um Heatmap de correlações.

TESTES ESTATÍSTICOS UTILIZADOS

SHAPIRO-WILK (SHAPIRO E WILK, 1965)

O teste de Shapiro-Wilk é uma ferramenta estatística usada para avaliar a normalidade de um conjunto de dados. Esse teste é particularmente eficaz e amplamente

recomendado para amostras de tamanho pequeno a moderado. O teste examina se uma amostra provém de uma população normalmente distribuída, comparando a ordenação dos dados amostrais com a de uma amostra perfeitamente normal. A fórmula do Shapiro-Wilk é:

$$W = \frac{(\sum_{i=1}^{n} a_i x_{(i)})^2}{\sum_{i=1}^{n}(x_i - \underline{x})^2}$$

Nesta fórmula, $x_{(i)}$ são os dados ordenados da amostra, a_i são constantes derivadas dos valores esperados da ordem estatística de uma amostra normal e é a média da amostra. O resultado W é o valor estatístico do teste, onde valores próximos a 1 sugerem que a amostra pode ser considerada como proveniente de uma distribuição normal. Valores substancialmente menores que 1 indicam desvios da normalidade. Este teste é amplamente utilizado devido à sua sensibilidade a desvios de normalidade, mesmo em amostras pequenas.

COEFICIENTE DE CORRELAÇÃO DE SPEARMAN (SPEARMAN, 1910)

A correlação de Spearman, aqui representada por *R*, é uma métrica não paramétrica de associação entre variáveis que se baseia na ordenação dos dados, apropriado para dados que não seguem uma distribuição normal, ou que contenha *outliers* significativos, como no caso dos dados de XRF, onde mede a força e a direção da associação entre duas variáveis (Kassambara, 2017). O método de correlação de Spearman calcula a correlação entre a classificação de *x* e a classificação das variáveis *y*, é comumente representada pela fórmula:

Onde:

$$r_s = 1 - \frac{6\sum d_i^2}{n(n^2 - 1)}$$

- r_s é o coeficiente de Spearman
- $\sum$ é a soma dos quadrados das diferenças entre os postos correspondentes das duas variáveis observadas
- d_i é a diferença entre os postos de cada par de observação entre as duas variáveis
- *n* é o número total de observações (pares de postos).
- *6* é o fator de normalização que garanta os limites esperados entre 1 e -1.

Onde:

- x' e y' são os rankings das variáveis x e y, respectivamente.

- mx' e my' são as médias dos rankings de x e y.

Ao empregar o método de Spearman, os dados dos elementos são ranqueados, permitindo uma análise mais flexível capaz de investigar as tendências de associação entres as variáveis, mesmo que essas relações não sejam linearmente definidas, visto que o coeficiente captura relações monotônicas entre as variáveis (ao aumentar ou diminuir uma variável, a outra também segue uma tendência clara e previsível, mantendo sempre a direção, de maneira crescente ou decrescente) que ajuda a determinar a significância estatística da correlação entre duas variáveis. Esse coeficiente é uma medida não paramétrica que avalia a força e a direção da associação entre as variáveis, baseando-se nos rankings dessas variáveis, ao invés de seus valores reais. O já o *p-valor,* por sua vez, indica a probabilidade de observar uma correlação tão forte quanto a calculada, sob a hipótese nula de que não existe associação entre as variáveis. Um p-valor baixo (<0,05) sugere que a correlação observada não é devida ao acaso, indicando uma associação significativa entre as variáveis.

MICROESPECTROSCOPIA RAMAN

ASPECTOS GERAIS

A espectroscopia Raman é uma técnica analítica que permite a caracterização molecular e, consequentemente, a análise de materiais através do espalhamento inelástico de luz, que ao interagir com as moléculas de uma amostra, emite fótons de energia diferente dos fótons originais. Esse processo resulta na transição entre diferentes estados vibracionais (Figura 3), possibilitando a identificação da composição química e mineralógica da amostra, já que a diferença de energia é diagnosticada pelo composto analisado.

A incidência de um feixe de luz monocromática sobre uma amostra causa excitação molecular, fornecendo energia correspondente aos seus níveis vibracionais e o espalhamento da luz pode ocorrer de duas formas principais: de maneira elástica, conhecida como espalhamento *Rayleigh*; e inelástica, chamada de espalhamento Raman, ou, efeito Raman. O espalhamento inelástico pode ser subdividido em espalhamento Stokes, quando há um deslocamento para frequências mais baixas, e anti-Stokes, para frequências mais altas que a radiação incidente (Lewis e Edwards, 2001).

O processo se inicia com a interação de um fóton, portador de energia hv0, com uma molécula no seu estado fundamental. Esta interação pode elevar temporariamente a molécula

a um estado energético mais alto, conhecido como estado virtual. A partir deste estado, a molécula pode retornar ao estado fundamental, emitindo um fóton com a mesma energia do incidente ($E_0 \rightarrow E_0$), caracterizando o espalhamento Rayleigh. Alternativamente, o material pode não voltar ao seu estado fundamental, e a molécula transitar para um estado de excitação vibracional ($E_0 \rightarrow E_1$); o fóton emitido terá energia menor, resultando em um espalhamento Stokes. Por outro lado, se uma molécula já em estado excitado (E_1) interage com o fóton, ela retorna para um estado com menos energia que o anterior à absorção do fóton (E_0), perdendo energia para o fóton, caracterizando o espalhamento anti-Stokes (Vandenabeele, 2013).

O espalhamento anti-Stokes é mais raro, uma vez que na maioria das condições ambientais, as moléculas se encontram no estado fundamental, resultando predominantemente em linhas Stokes, que são mais intensas do que as anti-Stokes. Os espectros Raman são analisados medindo-se os deslocamentos energéticos dos fótons espalhados em relação à energia da radiação de excitação, expressos em números de ondas (cm^{-1}). Portanto, nas amostras estudadas, a análise da energia dos fótons que são dispersados inelasticamente em relação à energia dos fótons que incidem, se relaciona com os modos de vibração normal do material. Estes deslocamentos fornecem informações sobre as transições vibracionais e rotacionais das moléculas, permitindo uma análise precisa da composição e estrutura molecular das amostras (Courtois, 1996).

MÉTODO EMPREGADO

A aplicação da microespectroscopia Raman no estudo de amostras fósseis destinou-se primariamente à determinação da composição mineralógica e orgânica.

As análises foram realizadas no Laboratório de Astrobiologia, no Instituto de Química, da USP. O equipamento Raman, *inVia Renishaw* (Figura 7B), foi ajustado com um espectro estático centrado em 800 cm^{-1}, um valor que indica o número de onda principal visado pelo laser, equipado com objetivas de 50 a 100x, proporcionando diferentes níveis de ampliação para observação detalhada da amostra, com laser em 785nm. O tempo de exposição variou de 5 a 30s, ajustado para equilibrar a intensidade do sinal e o tempo necessário para uma boa qualidade de espectro. A potência do laser ajustável de 0.1 a 1.0 permitiu um controle fino sobre a quantidade de energia irradiada, minimizando danos enquanto maximiza a detecção de sinais. O número de acumulações por medição, variando

entre 1 e 5, foi configurado para melhorar a relação sinal-ruído, otimizando assim a precisão dos dados coletados.

Para o processamento e interpretação dos dados, utilizou-se o software SpectraGryph 1.2, que permitiu um baseline *fitting* espectral eficiente, comparando-se os picos observados com referências validadas no banco de dados online RRUFF criada pelo mineralogista americano Dr. Robert T. Downs na Universidade do Arizona, que abrangente coleção de espectros Raman característicos de diversos minerais.

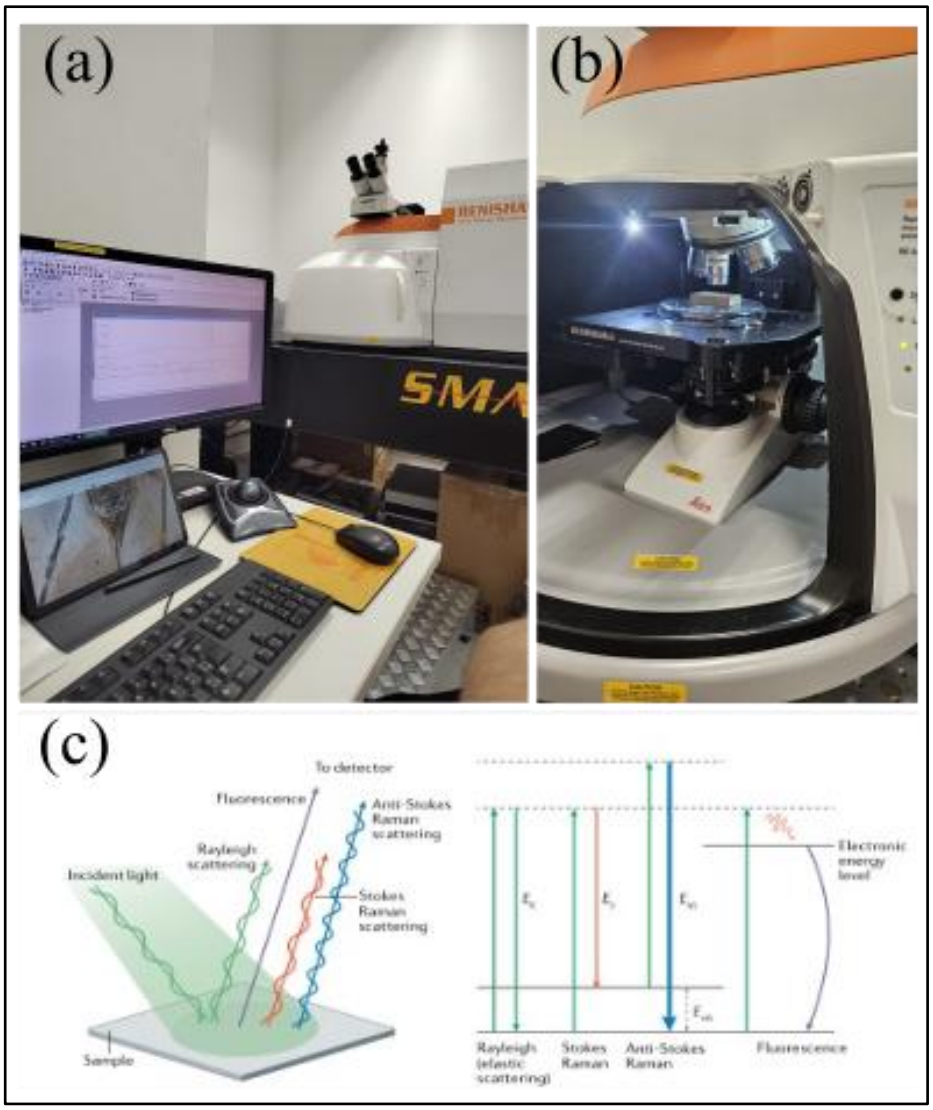

Figura 3. Espectroscopia Raman A-B. Equipamento de microespectroscopia Raman utilizado com a amostra sob anaálise. Fonte: Google Imagens (Fotos: Sabrina Belatto e Silvio Limeira Jr.). C. Espalhamento Raman, onde, E_{AS}, energia do fóton anti-Stokes; E_R, energia do fóton espalhado de Rayleigh; E_S, energia do fóton de Stokes; E_{vib}, energia da transição vibracional molecular. Retirado de Mosca et al., 2021.

MICROSCOPIA ELETRÔNICA DE VARREDURA (MEV) E FLUORESCÊNCIA POR DISPERSÃO DE ENERGIA (EDS) (FIGURA 8)

ASPECTOS GERAIS

O microscópio eletrônico de varredura (MEV) é utilizado em diversas áreas da ciência e engenharia para analisar a morfologia e composição de materiais em escalas microscópicas. Funciona por meio de um feixe de elétrons que é direcionado sobre a superfície de uma amostra operando em um vácuo para prevenir que os elétrons se dispersem no ar. À medida que o feixe varre a amostra, ele interage com os átomos da superfície, emitindo sinais que podem ser captados para formar uma imagem detalhada (Thermo Fisher, 2023).

A geração de imagens no MEV ocorre quando os elétrons que incidem sobre a amostra provocam a emissão de elétrons secundários, raios X e outros tipos de radiações e partículas, dependendo das características da superfície analisada. Esses sinais são captados por detectores específicos. Por exemplo, os elétrons secundários são utilizados para criar imagens de alto contraste das topografias superficiais, enquanto os raios X são analisados para obter informações sobre a composição elementar da amostra. As configurações do microscópio, como a tensão e *spot size* do feixe de elétrons, podem ser ajustados para realçar diferentes características da amostra.

Além de sua capacidade de fornecer imagens de alta resolução da superfície de amostras, o MEV quando tem o EDS acoplado é também extremamente útil para análises quantitativas e qualitativas da composição de materiais. Ele pode ser equipado com sistemas como a espectroscopia por energia dispersiva de raios X (EDS), que permite a identificação dos elementos presentes na amostra. Quando os elétrons do feixe de MEV interagem com os átomos da amostra, além de gerar elétrons secundários, também induzem a emissão de raios X característicos da composição elementar do material. O detector EDS é capaz de analisar esses raios X, medindo a energia e a intensidade de cada pico espectral para determinar quais elementos estão presentes e em que proporções (Egerton et al., 2023).

MÉTODO EMPREGADO

As medidas foram realizadas com equipamentos distintos em duas instituições:

microscópio eletrônico de varredura (MEV) FEI Quanta 250 FEG com detector de EDS Si (Li) da marca Oxford com software AZTec da marca Oxford (Instituto de Geociências da USP); e, MEV FEI Quanta 650 FEG com detector EDS da Oxford controlado pelo mesmo software (Laboratório Nacional de Nanotecnologia, LNNano).

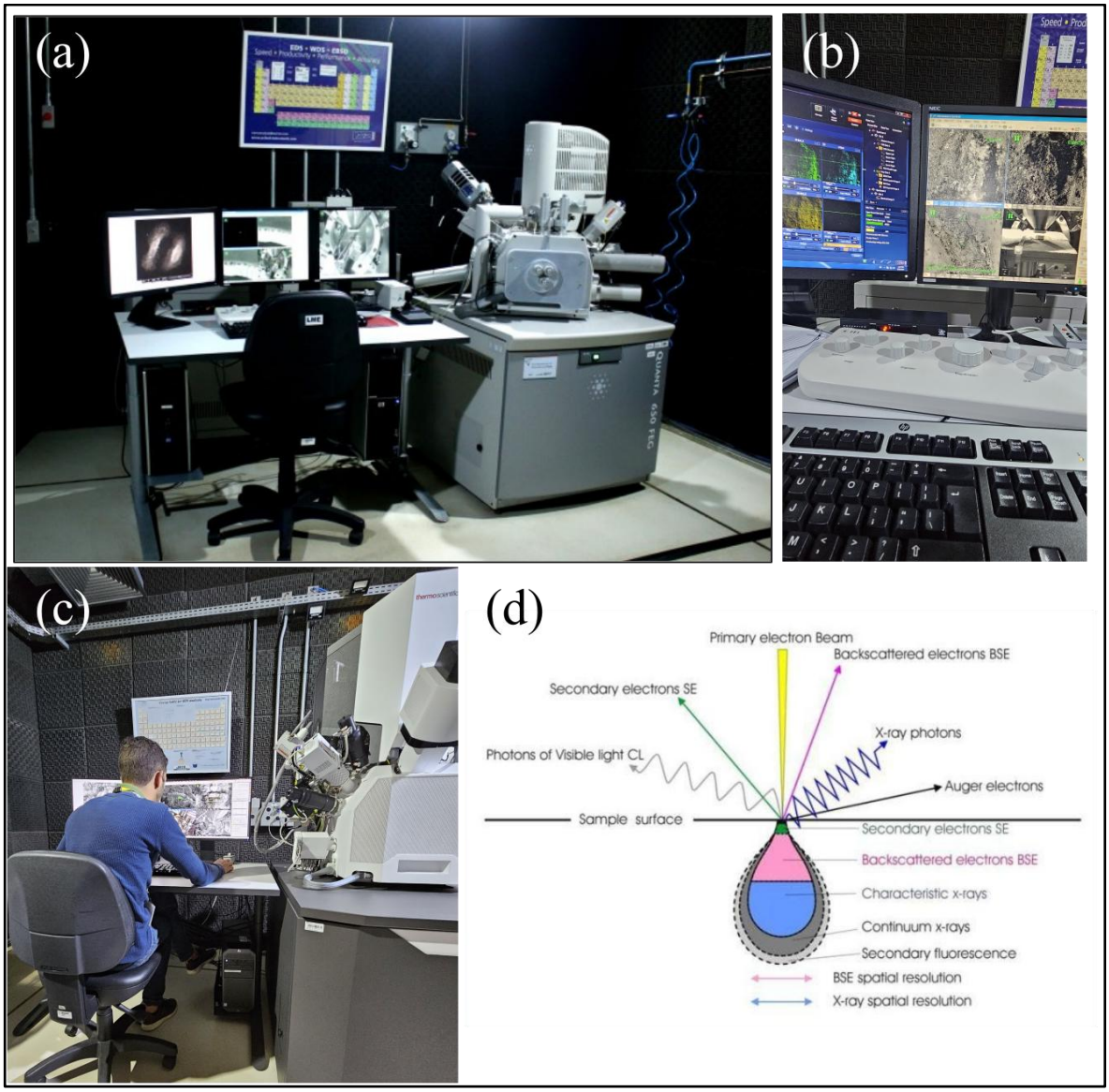

Figura 4. A-C. Equipamento de microscopia eletrônica de varredura com detector de fluorescência de dispersão de energia. Fonte: Website LNNano e Sabrina Belatto. D. Ilustração dos efeitos da interação de feixe de elétrons com amostra. Fonte: Website University of Glasgow.

Além das análises convencionais em MEV-EDS, foram também realizadas microusinagens por feixe de íons focalizados (FIB, *Focused Ion Beam*) para o preparo de lamelas ultrafinas, posteriormente utilizadas em microscopia eletrônica de transmissão com varredura (STEM-EDS) (Fig. 5). O sistema FIB permite a remoção controlada de material

em escala nanométrica por meio da aplicação de um feixe de íons (geralmente de gálio, Ga^{+}), que incide sobre a amostra com alta precisão. Esse feixe interage com a superfície, promovendo o sputtering de átomos e permitindo o corte de regiões específicas com espessura adequada para análise em transmissão.

As microusinagens foram conduzidas no sistema dual beam FEI Helios NanoLab 660, localizado no Laboratório Nacional de Nanotecnologia (LNNano/CNPEM), o qual integra em uma única câmara tanto a coluna de feixe de íons (FIB) quanto a de feixe de elétrons (MEV). Esse sistema permite a visualização simultânea da área de interesse por elétrons secundários e o fresamento controlado por íons. Após a extração da lamela por FIB, esta foi afixada em grid de cobre por micromanipulador e posteriormente afinada até espessuras inferiores a 100 nm. Esse procedimento é essencial para a obtenção de informações de composição e estrutura interna em escala submicrométrica por STEM-EDS.

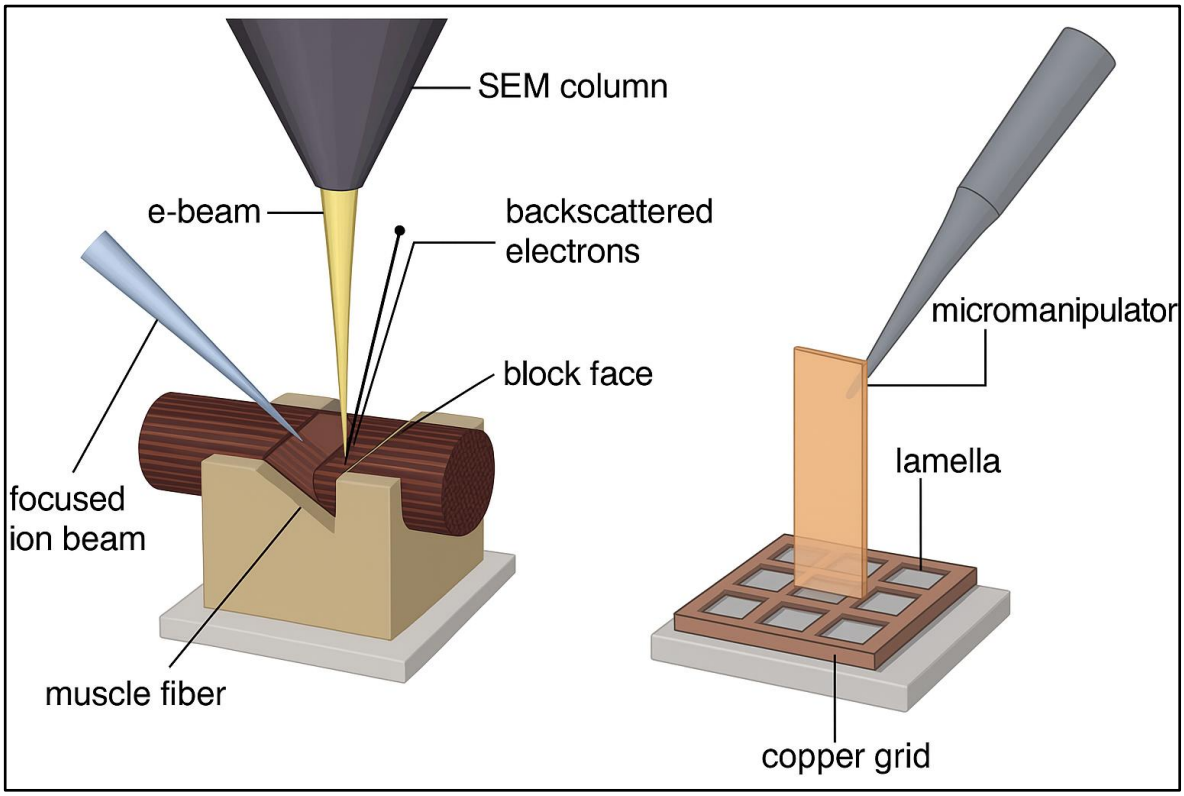

Figura 5. Esquema ilustrando o preparo de lamela ultrafina de fibra muscular por feixe de íons focalizados (FIB). À esquerda, o feixe de íons realiza o fresamento preciso da amostra sob visualização simultânea por MEV. À direita, a lamela obtida é fixada em um suporte de cobre (grid) com auxílio de um micromanipulador, etapa essencial para posterior análise em STEM-EDS (Foto confeccionada pelo aplicativo android IBIS-Paint pela autora).

CAPÍTULO ÚNICO

INVESTIGATING THE COMPLEXITY OF EXCEPTIONAL FOSSIL PRESERVATION: AN INTEGRATIVE MODEL FOR INSECTS FROM THE CRATO FORMATION.

Sabrina Larissa Belatto[1,2,3], Sílvio Cesar Marqui Limeira Junior[2,4], Gabriel Gonçalves[5], Alexandre Ribeiro Cardoso[6], Jaime Joaquim Dias[7], Mírian Liza Forancelli Pacheco[8], Gustavo Prado[9], Marcia de Almeida Rizzutto[2,4], Gabriel Leite dos Santos[10], Gabriel Ladeira Osés[1,2,4]

[1]Universidade Federal de São Carlos, Programa de Pós-Graduação Em Ecologia e Recursos Naturais, Rodovia Washington Luís, Km 235, 13565-905, São Carlos, SP, Brasil

[2]Laboratório de Arqueometria e Ciências Aplicadas ao Patrimônio Cultural, Instituto de Física, Universidade de São Paulo (USP), São Paulo, SP, Brasil

[3]Laboratório de Paleobiologia e Astrobiologia, Universidade Federal de São Carlos. Rodovia João Leme dos Santos, Km 110, 18052780, Sorocaba, São Paulo, Brasil

[4] Programa de Pós-Graduação em Física, Instituto de Física, Universidade de São Paulo, São Paulo, Brasil;

[5]Instituto Tecnológico de Paleoceanografia e Mudanças Climáticas (itt Oceaneon), Universidade do Vale do Rio dos Sinos (UNISINOS), Avenida Unisinos, 950, Cristo Rei, São Leopoldo - RS, Brasil;

[6]Universidade Federal dos Vales do Jequitinhonha e Mucuri, Instituto de Ciência e Tecnologia, Campus JK, MGC 367 - Km 583, nº 5000, 39100-000, Alto da Jacuba, Diamantina, Minas Gerais

[7]Universidade Federal do Rio de Janeiro, Centro de Ciências Matemáticas e da Natureza, Instituto de Geociências, Departamento de Geologia, J2-16, 21.949-900, Cidade Universitária – Ilha do Fundão, Rio de Janeiro, Brasil

[8]Universidade Federal de São Carlos -UFSCar, Rodovia João Leme dos Santos – Parque Reserva Fazenda Imperial, Sorocaba, SP 18052-780, Brasil

[9]Universidade de São Paulo, Instituto de Geociências, Rua do Lago, 562, 05508-080, Butantã, São Paulo, São Paulo, Brasil

[10]Instituto Federal de Educação, Ciência e Tecnologia de São Paulo, Câmpus São Paulo, Rua Pedro Vicente, 625, 01109-010, Canindé, São Paulo, São Paulo, Brasil

Acknowledgements

This study was supported by FAPESP grants 2022/06485-5, 2023/14250-0, 2023/17293-2 and 2023/04501-6. This study was financed in part by the Coordenação de Aperfeiçoamento de Pessoal de Nível Superior – Brazil (CAPES) – Finance Code 001 (PROAP/CAPES–PPGERN). We also acknowledge Gabriel Eduardo Baréa de Barros for assistance with statistical scripts, Evandro Silva, Fabio Rodrigues and the Quimiosfera Laboratory (LNLS), Isaac Jamil Sayeg (IGc–USP), Fernanda (IF–USP), as well as João and Fabiano for technical support under LNNano project collaborations.

ABSTRACT

The replication of biological structures by authigenic minerals during fossilization is well-known for yielding detailed preservation of soft tissues. It is challenging to understand the sequence of mineralization since late diagenetic processes superimpose upon early diagenetic and original compositions. This scenario is applied to recently discovered fossil insects from the grey limestone facies from the lower Cretaceous Crato Formation Lagersätte, Brazil. These have so far been largely described as kerogenized impressions with lower preservation relative to the originally pyritized insects from this unit. In order to test the hypothesis that preservation is more complex in such facies, we have employed a multi-technique approach using XRF, Raman micro spectroscopy and electron/ionic microscopy-based techniques (SEM, FIB, STEM and EDS). We show that insects have been also replicated by pyrite and phosphates, while sulfates (jarosite, barite and gypsite) are most likely alteration phases, yielding exquisitely preserved muscles and putative digestive structures. Statistical approach of XRF data supports previously only hypothesized elemental distribution that mineralogical identification with independent Raman and microscopy analyzes. We also argue that the identification of organic matter by Raman spectroscopy can be controversial in such samples, as data may be related to the luminescence of rare-earth elements in carbonates and phosphates. A new integrative model is proposed for the Crato Formation insects, shedding light on the importance of disentangling mixed processes, by providing a sequential precipitation of minerals.

Keyword:

1 INTRODUCTION

The analysis of how fossilization leads to exceptional preservation, particularly the authigenic mineralization of soft tissues, is challenging due to the complexity of data kept in fossils. It is a hard task to disentangle primary, early, and late diagenetic mineralogies and purported original organic signals [1-2]. An effective strategy to deal with this task involves using a multi-technique approach, in which complementary methods provide morphological, chemical, and mineralogical data, yet being independent in validating distinct information. Different techniques may rely on different physical principles and methodologies, thus when yielding similar information, data is more reliable.

Paleobiodiversity of the Crato Formation Lagerstätte includes bacteria, fungi, insects, crustaceans, arachnids, myriapods, fish, amphibians, turtles, lizards, crocodylomorphs, pterosaurs, non-avian dinosaurs, birds, snakes, as well as representatives of the plant kingdom such as pteridophytes, conifers, gnetophytes, and angiosperms [3-7), that offer a unique window for the study of morphological and ecological information rarely preserved in the fossil record [8-12]. The Crato Lagerstätte represents a complex lake system, colonized by microbial communities and microbialites whose morphology indicates progressive deepening of the water column [13-15). The presence of halite pseudomorphs in the layers reveals episodes of hypersalinity under dry environmental conditions [16], which reinforces favorable conditions for preservation of soft tissues [15].

The study of fossilization processes constitutes the science of taphonomy, being fundamental to understanding the bias of geological processes in the original morphology and composition of organisms [17]. To this end, the fidelity of morphological preservation, the chemical and mineralogical composition of fossils are commonly characterized by non-destructive paleometry techniques [18-21]. This research aimed to investigate the preservation of fossil insects from the grey limestone facies of the Crato Lagerstätte, evaluating the role of microbial processes in the fossilization through a multi-technique approach, focusing on statistical analysis to test previous hypotheses regarding elemental distribution in fossils. We provide a new integrative and sequential model for the preservation of these fossils, refining previous approaches, thus showing the importance of disentangling mineralogical processes from different diagenetic stages.

1.2 GEOLOGICAL CONTEXT

The Crato Formation, located in the Araripe Basin (NE Brazil), records one of the most complete continental biotas of the Cretaceous [22]. The basin is of the pull-apart rift type, formed by tectonic events associated with the opening of the South Atlantic and the reactivation of basement structures [23]. The Crato deposits are approximately 90 meters thick, with laminated limestones, shales and sandstones, reflecting lacustrine environments witha brief marine incursion [13, 15]. The Nova Olinda member corresponds to post-rift deposits, with laminated limestones, salt pseudomorphs and isotopic signatures indicative of hypersaline, restricted and lacustrine conditions with limited freshwater input and elevated evaporation rates [15]. Catto *et al.* [24] and Warren *et al.* [25] pointed to the microbial

influence on the origin of these laminated limestones, suggesting an organomineralization process mediated by microbial mats. These deposits configure a Lagerstatte with broad faunal and flora diversity [3-4). The unit is attributed to the upper Aptian [26-29] (Fig. 1).

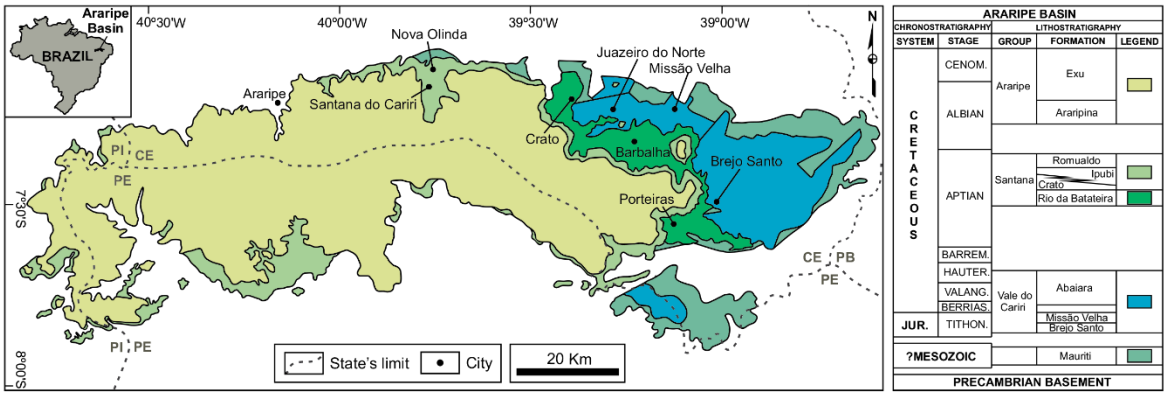

Figure 1. Legend: Geological map and the stratigraphic chart of the Araripe Basin. The insect fossil specimens are from the late Aptian Crato Formation (Santana Group). PI: Piauí State; PE: Pernambuco State; CE: Ceará State; PB: Paraíba State; JUR.: Jurassic; TITHON.: Tithonian; BERRIAS.: Berriasian; VALANG.: Valanginian; HAUTER.: Hauterivian; BARREM.: Barremian; CENOM.: Cenomanian. The nomenclature of the lithostratigraphic units is based on Assine et al. (2014). The geological map is modified from [22] and [6].

2 MATERIALS AND METHODS

The fossil insects in this study comprised two specimens of the order Orthoptera – GP/1E11237c (Fig. 2a-b) and GP/1E10501 (Fig. 2c); and two specimens of the order Blattodea – GP/1E10609 (Fig. 2d-e) and GP/1E10836 (Fig. 2f). The samples are deposited in the Scientific Collection of Paleontology of the Institute of Geosciences, University of São Paulo (USP) and were analyzed for morphological, chemical and mineralogical characterization, using different analytical techniques.

2.1 EDXRF AND STATISTICAL ANALYSIS

We used the energy-dispersive X-ray fluorescence (EDXRF) technique, with the aim of identifying the elements present and their distribution in different regions of the samples. In samples GP/1E11237c and GP/1E10609, the selection of points was based on the visual distinction of coloration, including beige-colored areas, black-colored areas and the host rock. On the other hand, samples GP/1E10501 and GP/1E10836 did not present visible chromatic variations; therefore, the measurement points were defined considering two distinct fossiliferous regions and a region corresponding to the embedding rock.

The measurements were performed using portable EDXRF equipment at the Laboratory of Archaeometry and Sciences Applied to Cultural Heritage (LACAPC), of the Institute of Physics of USP (IF-USP). The system consists of a mini X-ray tube with silver anode (Amptek) and a 125 eV FWHM fast silicon drift detector (SDD) for the 5.9 KeV Mn line. Measurements were performed in situ at a voltage of 30 kV and a current of 5 μA, with an excitation/detection time of 100 s.

Initially, we used the WinQXas software to process the data and generate brief reports with the element counts. We performed the visual representation of the raw spectra to observe the absolute intensities and the general pattern of the elemental counts. The data were then normalized using Argon (Ar), correcting for possible instrumental variations between the acquisitions. From this corrected matrix and with the data transformed into $\log_{10}$, we used the RStudio 4.3.1 software for all the statistical methods of the study. We previously generated scatter plots between the elements, allowing a preliminary visual analysis of the possible associations or geochemical co-occurrences. Subsequently, we applied the Shapiro-Wilk normality test to the raw data for each element to verify whether the distributions adhered to the normal curve. Given the predominance of nonparametric distributions, we adopted the Spearman demonstration test, which enabled the identification of monotonic associations between pairs of elements without pressure or linearity, accompanied by their respective *p-values*.

In a subsequent step, we focused on the comparative statistical analysis of samples GP/1E11237c and GP/1E10609, as they are the only ones that present visually distinct chromatic areas at the fossils (beige and black). In these two samples, we applied the Kruskal-Wallis test to investigate whether there are significant differences in the elemental composition between beige, black and rock regions. This nonparametric approach was chosen because it does not require a normal distribution and is robust to data with different scales and variances.

2.2 RAMAN MICRO SPECTROSCOPY

Raman micro spectroscopy was performed to identify minerals and organic matter. The measurements were performed in situ with Renishaw *inVia* equipment, with a static spectrum centered at 1500 cm^{-1} with a 50x objective lens and a 785 nm laser. The exposure time varied from 5 to 30 s and the number of accumulations per measurement varied between

1 and 5, to improve the signal-to-noise ratio. The laser power varied from 0.1 to 1.0% (nominal laser power of 320 mW), enhancing the control over the amount of irradiated energy, minimizing damage and maximizing signal detection. Raman spectra were identified using the RRUFF database and the references compiled in Table 2 (Supplementary Material).

2.3 Electron microscopy and Ion beam sample preparation (SEM-EDS-FIB-STEM)

For the morphological and compositional characterization of fossil microstructures and mineralogical habits and textures, a FEI Quanta 250 FEG scanning electron microscope (SEM) with an Oxford Si (Li) energy dispersive spectroscopy (EDS) detector and Oxford AZTec software (Institute of Geosciences, USP) was used, as well as a FEI Quanta 650 FEG SEM with an Oxford EDS detector and the same control software (National Nanotechnology Laboratory – LNNano, CNPEM). All analyzed samples (GP/1E11237c (Fig. 2a; b), GP/1E10609 (Fig. 2d; e), GP/1E10501 (Fig. 2c) and GP/1E10836 (Fig. 2f) were examined by SEM with coupled energy dispersive spectroscopy (EDS) for the qualitative and semi-quantitative analysis of the elemental composition of the regions of interest (the sample GP/1E10836 was coated by gold/palladium). This approach allowed the identification of the elements present with greater spatial resolution in relation to the data obtained by X-ray fluorescence (XRF).

In the GP/1E11237c sample, the focused ion beam (FIB) technique was used to prepare an ultra-thin lamella of a fossilized muscle fiber from a fragment removed from the left hind leg. The lamella was subsequently analyzed by STEM-EDS, allowing morphological and compositional characterization at the nanometric scale of the preserved structures. These analyzes were performed at the LNNano in a Thermo Fisher Scientific Helios NanoLab 660 dual beam microscope.

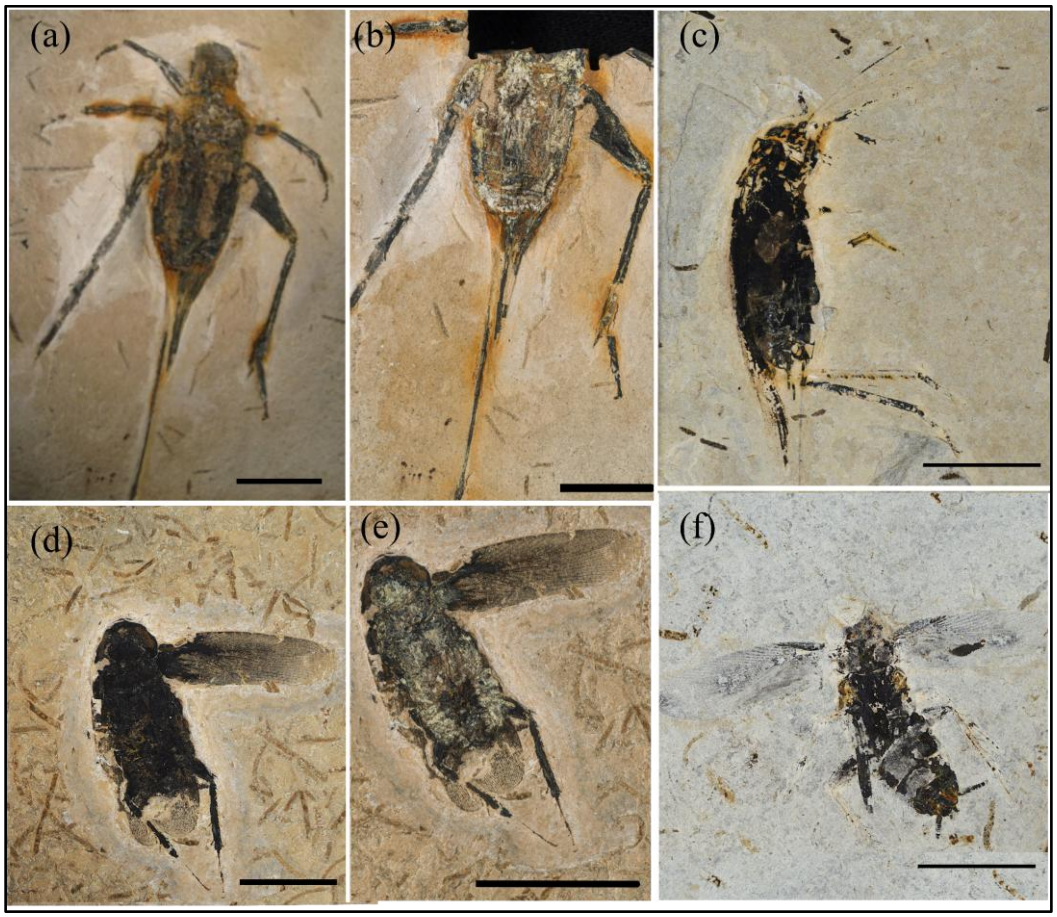

Figure 2. Photographs of the samples analyzed. Scale (1 cm): **(a - b)** sample GP/1E11237c - Orthoptera; **(c)** sample GP/1E10501 - Orthoptera; **(d - e)** sample GP/1E10609 - Blattodea; **(f)** sample GP/1E10836 - Blattodea.

3 RESULTS

3.1 X-RAY FLUORESCENCE (XRF)

3.1.1 XRF SPECTRA

Iron (Fe), calcium (Ca) and sulfur (S) are the most abundant elements in all samples, both in the host rock and in the fossils. Ca presents a relatively uniform distribution among the analyzed areas. The occurrence of iron (Fe), sulfur (S), chromium (Cr), cobalt (Co), copper (Cu) and lead (Pb) is associated with fossils, with low content or absence of them in the rocks. Phosphorus (P) is a minor component, but in all cases, it occurs in the fossils, and barium (Ba) was recorded at specific points of the sample GP/1E11237c (Fig. 3a - d).

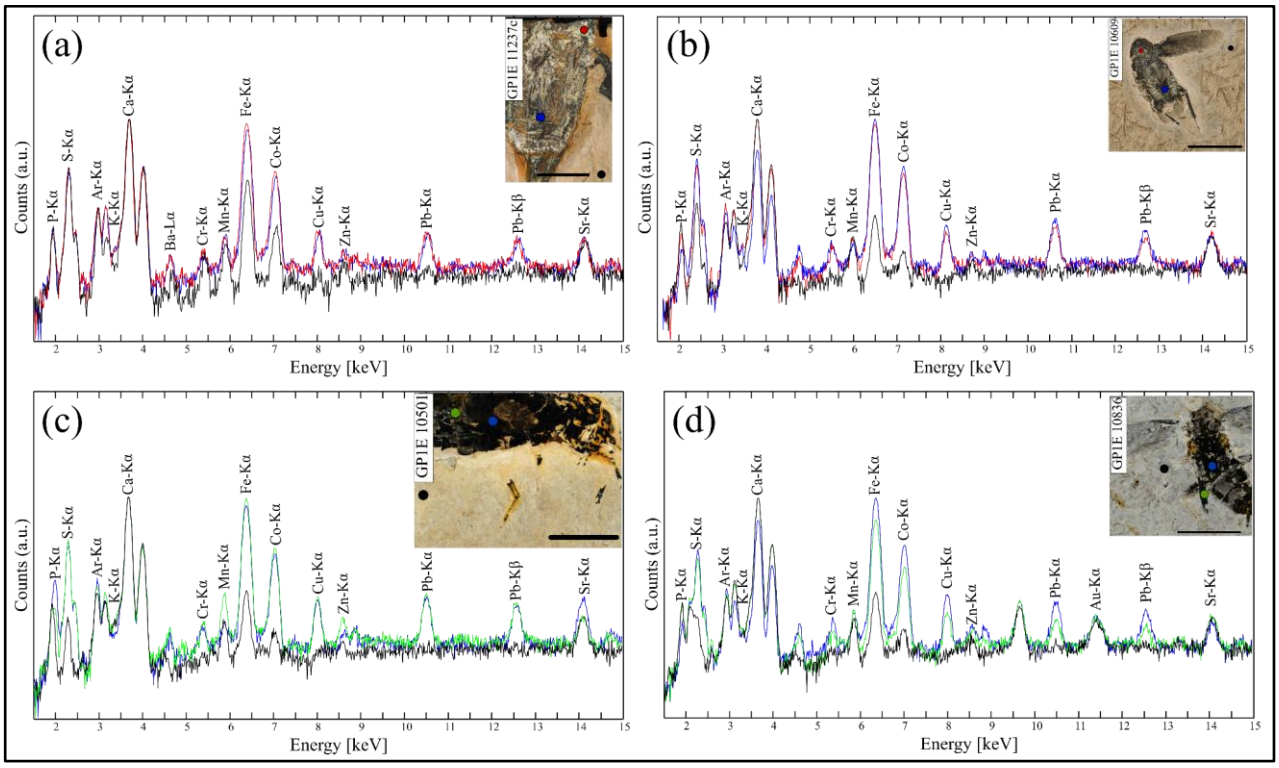

Figure 3. X-ray fluorescence (XRF) spectra from samples **(a)** GP/1E11237c, **(b)** GP/1E10609, **(c)** GP/1E10501, and **(d)** GP/1E10836, showing element distribution as a function of energy (x-axis, in keV). The spectra correspond to the color-coded points indicated in the photographic insects for each sample. The Ar is naturally detected during XRF analysis, while the gold (Au) signal results from gold-palladium coating for SEM imaging. Scale (5mm).

3.1.2 Scatter plots

After observing possible patterns of variation in the spectra as a function of analyzed areas, scatter plots with linear regression lines were constructed to statistically investigate the relationships between the elements, with a special focus on the influence of Fe, S and Ca (Fig. 4).

Manganese (Mn), strontium (Sr) and potassium (K) does not show a clear trend of increase or decrease in relation to Fe (Fig. 4a). P showed a positive slope in relation to Fe, but the P counts are too low to consider a direct trend between these elements (Fig. 4a). On the other hand, S shows a direct and strongly directed trend towards Fe, that is, as Fe increases, S also increases consistently (Fig. 4a). Fe also exhibits a strong positive slope and association with the elements Co, Cr, Cu, Pb and zinc (Zn) (Fig. 4b); however, the association of Fe and Zn exhibits a relatively weak increasing trend.

Sulfur shows similar associations to Fe, whereas Mn, Sr and K are constantly independent of S (Fig. 4c). The strong positive association with Co, Cr, Cu, Fe and Pb (Fig.

4c) is evidenced by a well-defined linear regression, the same occurring with Zn in these observations, which despite positive linearity, exhibits a relatively weak trend (Fig. 4d).

Regarding Ca, a completely independent behavior is observed regarding the elements to which it was compared. The positive associations are very weak in relation to Sr and Mn, and those with P and K have a neutral association (Fig. 4e). Ca has a slight tendency towards a negative association, comparing with the elements strongly positively correlated with S and Fe (Fig. 6f).

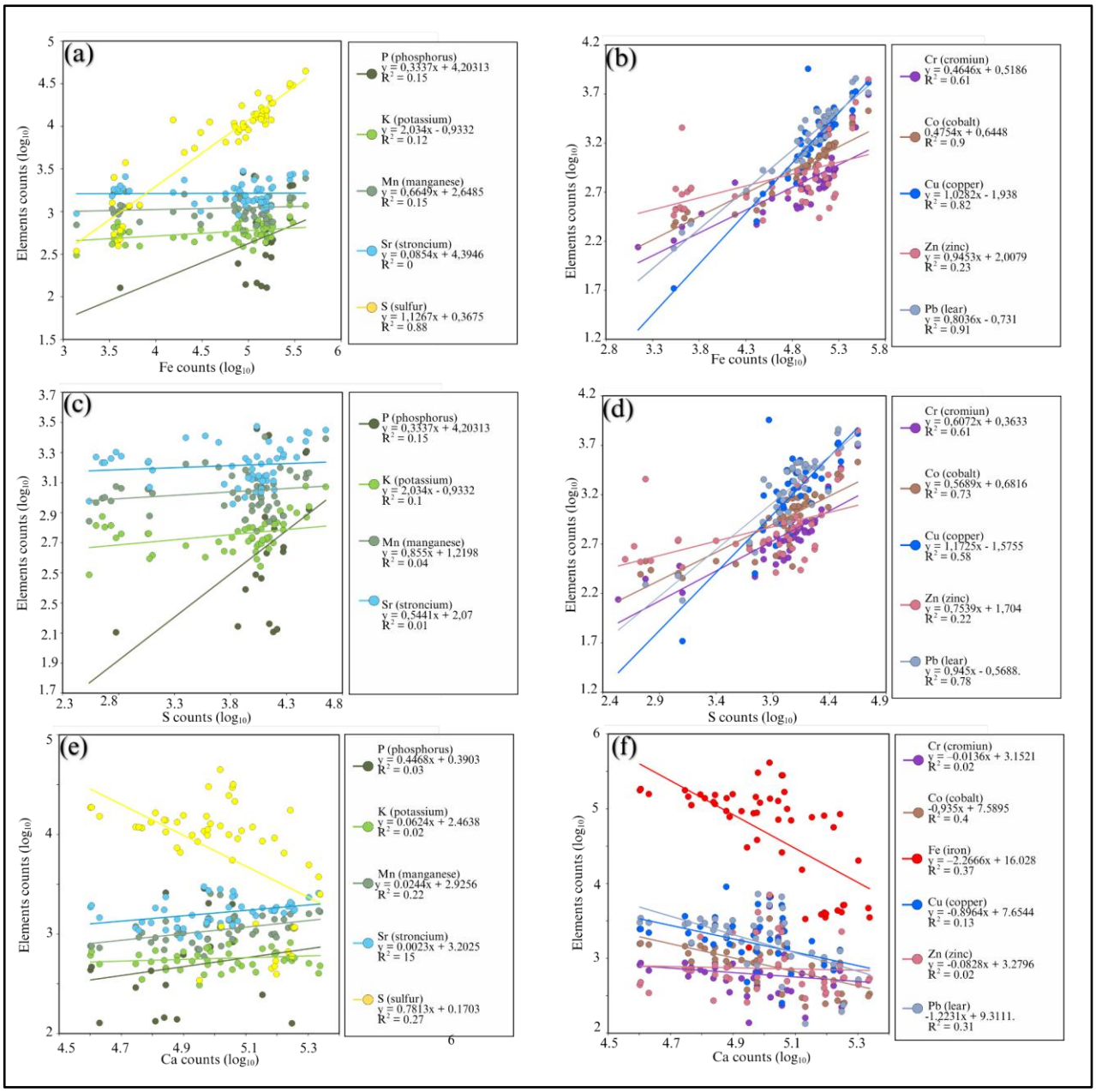

Figure 4. Scatter plots with linear regressions between major and trace elements as a function of Fe **(a–b)**, S **(c–d)**, and Ca **(e–f)**, with corresponding R^2 values indicated. Each element is represented by a distinct color. Data obtained from normalized XRF analyses.

Based on the XRF spectra and scatter diagrams, we applied statistical tests to evaluate the correlations between the chemical elements in all samples. The normality of the data was verified using the Shapiro-Wilk test, and the results (W and *p-values*) indicate that all elements present $p < 0.05$, supporting non-normal distributions and justifying the adoption of non-parametric statistical methods. W values range from 0.59 to 0.97, indicating varying degrees of adherence to normality. Full results are provided in Supplementary Material (Table 1).

3.1.4 KRUSKAL-WALLIS TEST

Statistical analysis (Fig. 5) indicates significant differences in elemental counts between host rock and fossils ($p < 0.001$), with the former presenting lower values and more consistent composition. There was no difference between beige and black areas of fossils ($p > 0.05$), indicating similar geochemical patterns. Fe presents high counts at fossils, while Ca is homogeneously distributed among all groups.

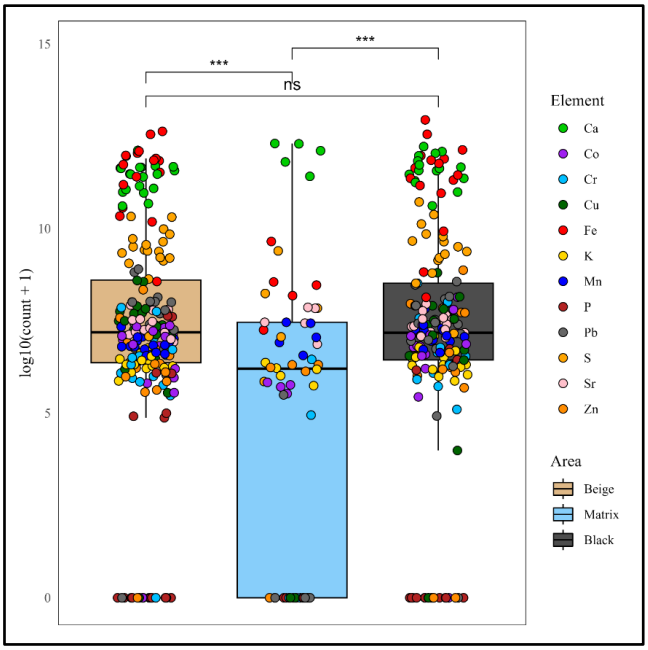

Figure 5. Representation of chemical elements count in the beige, matrix, and black areas of the fossils on a logarithmic scale. The points correspond to an individual chemical element measurement, as indicated in the legend on the right (Ca, Co, Cr, Cu, Fe, K, Mn, P, Pb, S, Sr, Zn). The boxes illustrate the dispersion of the data in each area, with the inner line indicating the median of the distributions. Statistical comparisons between areas are represented at the top of the figure, with significant levels indicated by asterisks (*** for $p < 0.001$; ns for not significant).

3.1.5 SPEARMAN CORRELATION

The correlation test between pairs of chemical elements indicated statistically significant correlation (p-values < 0.05) (Fig. 6a), with correlation coefficients (ρ) ranging from –0.59 to +0.98 (Fig. 6). Among the results, a very strong positive correlation was observed between the pairs Fe-Cu, Fe-Pb, Cu-Pb, Co-Cu, Fe-Co, Co-Pb, and Cr-Fe, with coefficients ranging from ρ = 0.98 for Fe-Cu to ρ = 0.74 for Co-Cr, all with significant p-values. S showed a significant positive correlation with Fe, Cu, Pb, Cr, and Co, and near-zero but slightly positive correlations with K, P, and Zn, suggesting a tendency toward weak or neutral associations (Fig. 6). Ca showed negative correlations with all elements strongly correlated with Fe, all corroborated by the p-values. Despite that, it showed a tendency towards positive correlation with Mn and Sr. Mn showed positive correlation only with Sr, Zn and K. The correlation between Sr and Zn is weakly positive (Fig. 6a).

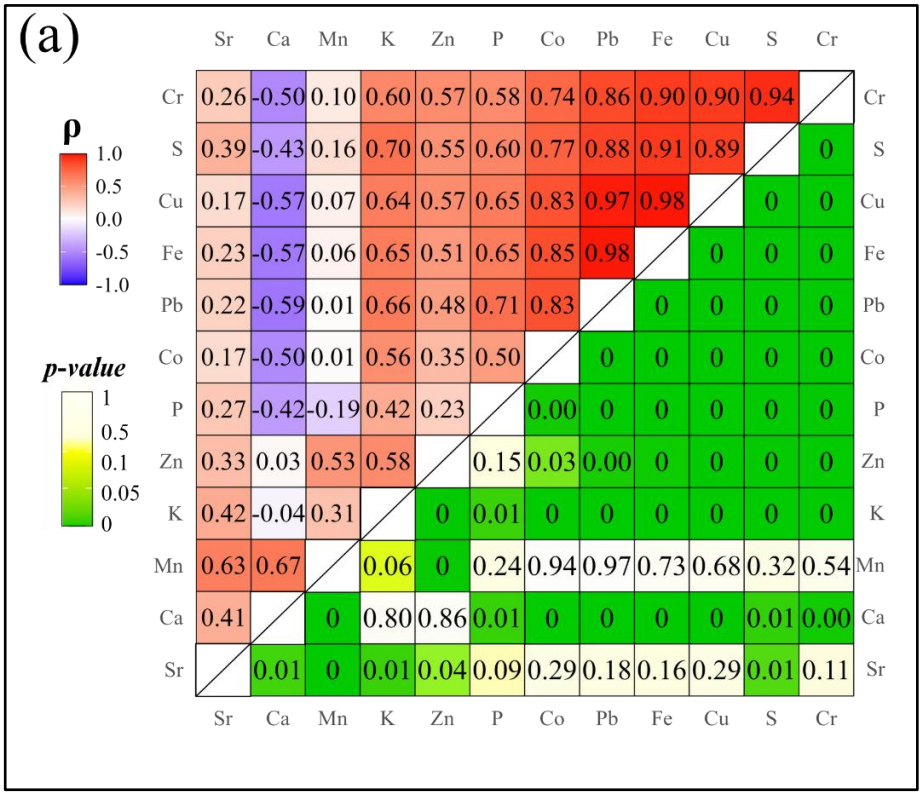

Figure 6. Spearman Correlation Heatmap in the upper triangle, with p-values in the lower triangle. The upper triangle displays Spearman correlation coefficients (ρ), ranging from +1 (strong positive correlation – elements increase together, shown in red tones) to –1 (strong negative correlation – one element increases as the other decreases, shown in bluish tones). Values close to 0 indicate no monotonic correlation (white). The lower triangle shows the p-values associated with each correlation. Values of $p \leq 0.05$ (in green) indicate statistically significant correlations, meaning the association is unlikely to have occurred. P-values > 0.05

(from yellow to white) indicate non-significant correlations, suggesting the observed association may not be statistically robust.

3.3 Raman Micro spectroscopy

In the black-colored points "BP" of samples GP/1E11237c (Fig. 7a3 - P2) and GP/1E10609 (Fig. 7b3 - P4), the spectra are similar, presenting bands attributed to pyrite (FeS_2) (342-343 cm^{-1} and 379 cm^{-1}) and to calcium sulfate (gypsum; $CaSO_4 \cdot 2H2O$) (1005-1008 cm^{-1}) (Table 2) (Fig. 7a-c). The beige-colored points "BeP", in turn, present predominantly iron sulfate composition, identified here for the first time in the fossils of the Crato Lagerstatte as minerals from the jarosite group (Table 2; Fig. 7a3 - P1; 7b3 - P3). The jarosite group composition is XFe3+3(SO4)2(OH)6, with X usually representing a monovalent cation (such as K+, NH4+, H3O+, etc.), the most common being the potassic member, known simply as jarosite [30]. The band at 982 cm^{-1}, observed in both zones (Fig. 7a; b), was attributed to the ν_1 mode (symmetric stretching of SO_4^{2-}), indicating the presence of the sulfate ion and suggesting the possibility of the presence of sulfate-rich minerals, such as, for example, hydrated phases of magnesium sulfate [31]. (Supplementary Table 2).

In sample GP/1E10501, we identified FeS_2 (339-340 cm^{-1}) (Fig. 7c3; P5 - P6), $CaSO_4 \cdot 2H2O$ (1008 cm^{-1}), and calcite $CaCO_3$, characterized by the intense symmetric stretching band of the carbonate group at 1089 cm^{-1} (Fig. 7c3 – P6). A weak band at 960 cm^{-1} (Fig. 7c3 – P5) corresponds to the ν_1 PO_4^{3-} mode of calcium phosphate, possibly apatite [$Ca_5(PO_4)_3X$, where X = F^-, Cl^-, OH^-, etc.]. No other phosphate-related bands were clearly observed, which limits the precision of the mineralogical identification.

The broad bands at approximately 1186 and 1293 cm^{-1} (Table 2; Fig. 7c3 - P5) are most likely indicative of laser-induced photoluminescence of rare-earth elements (REEs). These bands are the first of a pattern of six or more bands recurrently observed in fossils in Crato Formation (e.g. [32-33]) and elsewhere (e.g. [34-35]) and often associated with vibrational modes of organic molecules. However, extended Raman spectra of minerals naturally containing REEs show this same pattern when analyzed using the 785 nm laser, e.g. phosphates such as monazite (RRUFF ID: R040106) and fluorapatite (RRUFF ID: R060333). The combination of 785 nm laser and the region between 1000 - 2000 cm^{-1} for the bands is an indication that the photoluminescence may be caused by the presence of the Nd3+ ion [36-39].

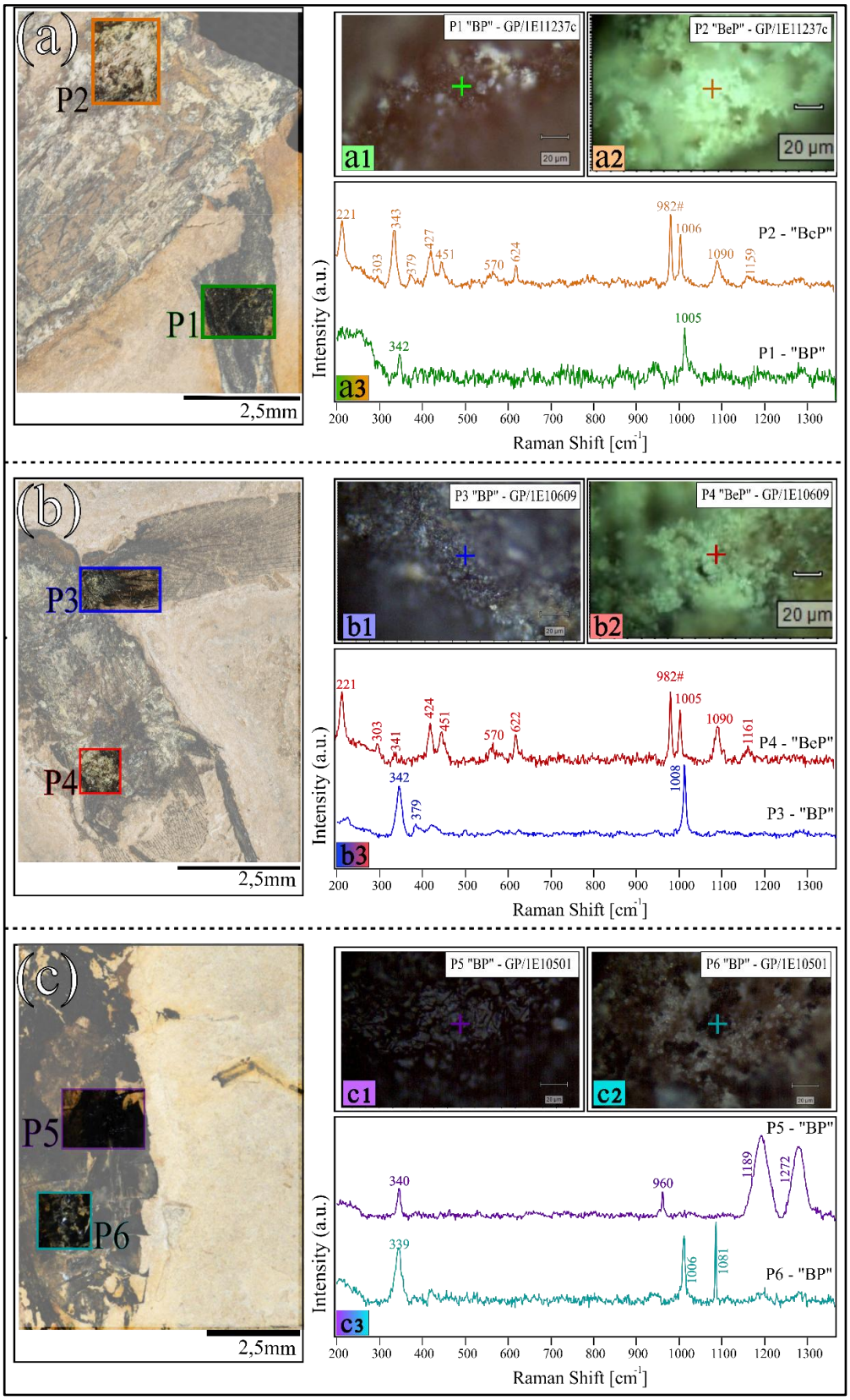

Figure 7. (a) Samples GP/1E11237c and **(b)** GP/1E10609, highlighting the points analyzed by Raman spectroscopy: P1 and P3 (black-colored points – "BP"), P2 and P4 (beige-colored points – "BeP"). **(a1–a2, b1–b2)** Photomicrographs of the measurement points. **(a3–b3)** Raman spectra obtained from the marked regions, with mineral identification: pyrite (FeS_2) in P1 and P3; jarosite in

P2 and P4 and sulfate bands. **(c)** Sample GP/1E10501 highlighting the points analyzed by Raman spectroscopy: P5 and P6 (black-colored points – "BP"). **(c1–c2)** Photomicrographs of the measurement points. **(c3)** Raman spectra from the marked regions, with mineral identification: in P5, pyrite (FeS_2), calcium phosphate, and luminescence signals; in P6, pyrite, gypsum, and calcite.

3.4 SCANNING ELECTRON MICROSCOPY (SEM), FOCUSED ION BEAM (FIB), SCANNING TRANSMISSION ELECTRON MICROSCOPY (STEM), AND ENERGY DISPERSIVE SPECTROSCOPY (EDS)

3.4.1 SAMPLE GP/1E11237C (ORTHOPTERA)

The analyses of the GP/1E11237c sample were conducted in two distinct anatomical regions of the fossil: a fragment detached from the left hind leg (Fig. 8b - k) and at the abdomen (Fig. 8m - o). In the fragment of the left hind leg, muscle fibers are preserved by different micrometric crystal habits, such as elongated, subhedral prismatic crystals, rhombohedral, and euhedral granular crystals (Figs. 8l - n). Additionally, a possible digestive organ was identified, exhibiting a morphology like gastric ceca (Fig. 8m - o).

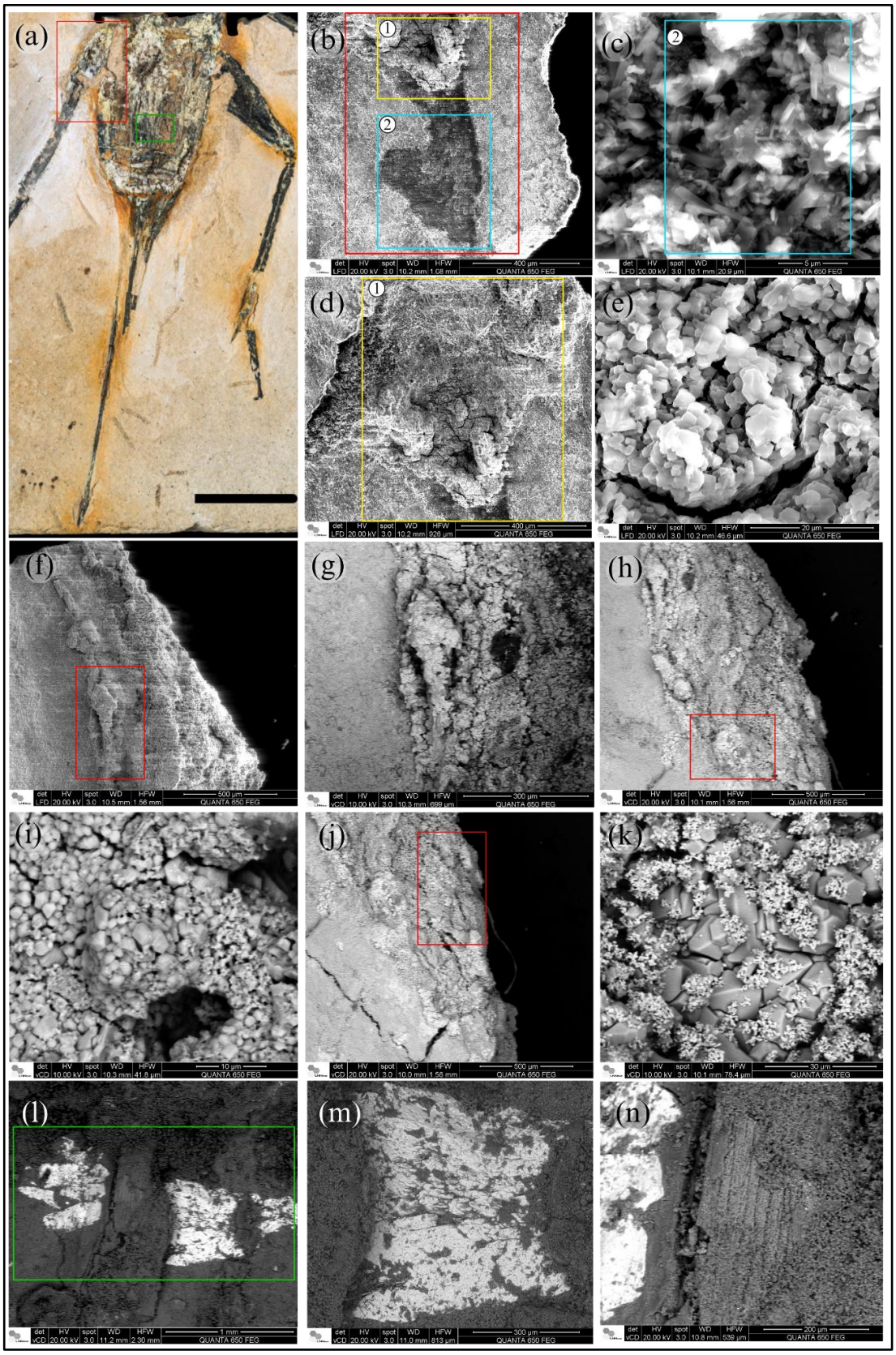

Figure 8. Micrographs of sample GP/1E11237c. **(a)** General view of the sample, with rectangles marked to indicate the areas where the micrographs were obtained, divided into three regions: area 1 — red rectangle (left hind leg); area 2 — green rectangle (abdomen). **(b)** Fragment of area 1 containing preserved muscle fiber, subdivided into two positions with distinct textures: (b1) yellow

rectangle and (b2) light blue rectangle. **(c)** Elongated, subhedral micrometric crystals, slightly covered by anhedral microcrystals, corresponding to position b1. **(d)** Enlargement of position b2. **(e)** Enlarged detail of d, showing rhombohedral, micrometric, euhedral iron sulfide crystals with fine growth striations. **(f)** Preserved muscle fiber. **(g)** Detail of "f". **(h)** Detail of the muscle fiber observed in "f" and "g". **(i)** Microcrystals preserving the muscle fiber of "h", like the crystals in "e", with evident growth striations. **(j)** View another region of muscle fiber. **(k)** Enlargements of "j", showing micrometric, euhedral pyrite crystals covered by granular iron sulfide nanocrystals, with morphologies ranging from subhedral to anhedral. **(l)** Non-identified preserved abdominal organ. **(m)** Magnification of "l". **(n)** Muscle fibers covering the abdominal organ.

The elongated crystals (Fig. 9a) revealed a predominance of S, Ca and O, being identified as calcium sulfate, possibly gypsum ($CaSO_4.2H_2O$) and/or anhydrite ($CaSO_4$) (Fig. 9b). The rhombohedral crystals (Fig. 9c) are composed elementally of Fe and S (Fig. 9d), compatible with the presence of minerals belonging to the iron sulfide and/or sulfate classes.

Granular crystals (Fig. 9e) revealed a majority composition of Pb and S, suggesting the possibility of the presence of galena (PbS) or similar phases (Fig. 9f). In the abdominal region, the mineralized characteristics appear to be of biological origin. The shape of the fragment suggests preservation possibly related to the gastric ceca — organs involved in the digestive process together with the proventriculus [40]. This is a sclerotized region, which could have favored its preservation, as occurs with the proventriculus themselves (e.g. [11]) (Figs. 9l; m). However, due to the limited state of preservation, it is not possible to reliably identify the nature of the biological structure. Abdominal muscle fibers can be observed partially covering the mineralized biological fragment (Fig. 9n).

The digestive organ (Fig. 9g) shows an elemental composition dominated by Ba and S, consistent with barium sulfates and suggesting the possible presence of barium sulfate, perhaps barite ($BaSO_4$) (Fig. 9h).

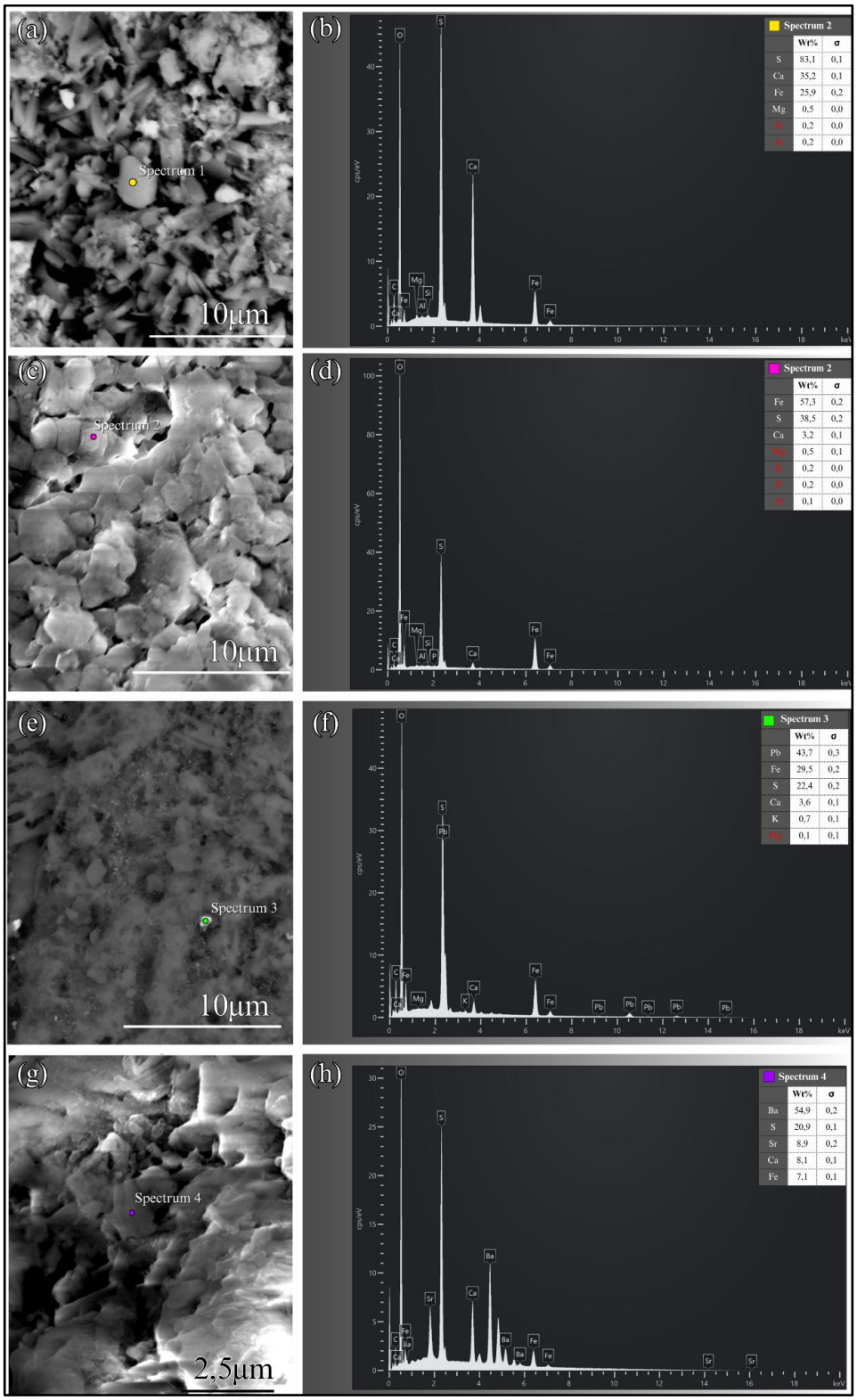

Figure 9. SEM-EDS of the localized crystals preserving the muscle fiber (a -e) and the possible organ (g -h) of the samples GP1E11237c. **(a)** Granular nanocrystals observed covering the prismatic crystals. **(b)** Spectra of the prismatic crystals **(c)** Euhedral crystals. **(d)** Spectra of the elemental compositions of rhombohedral crystals. **(e)** The right hind leg, tibiofemoral joint. **(f)** Spectrum of the elemental composition of the crystalline microplot. **(g)** Barium sulfate crystals. **(h)** Spectrum showing the presence of barium sulfate.

FIB-STEM-EDS analyses of a lamella extracted from a muscle fiber from the hind leg (Fig. 10a; b; c) revealed differences between the mineralogical composition of the external (Fig. 16b) and internal (Fig. 10c) portions of this structure. At the top of the lamella (outermost region of the fiber) exhibits Ca and S, but no Fe, indicating a calcium sulfate composition, possibly gypsum ($CaSO_4$ $2H_2O$) (Fig. 10b1; b2). In contrast, the base of the lamella (inside the fiber), Fe, S, and Cu were detected in a nano granular texture, suggesting a sulfide composition, possibly chalcopyrite ($CuFeS_2$) or copper-enriched pyrite (Fig. 10c1 - c3).

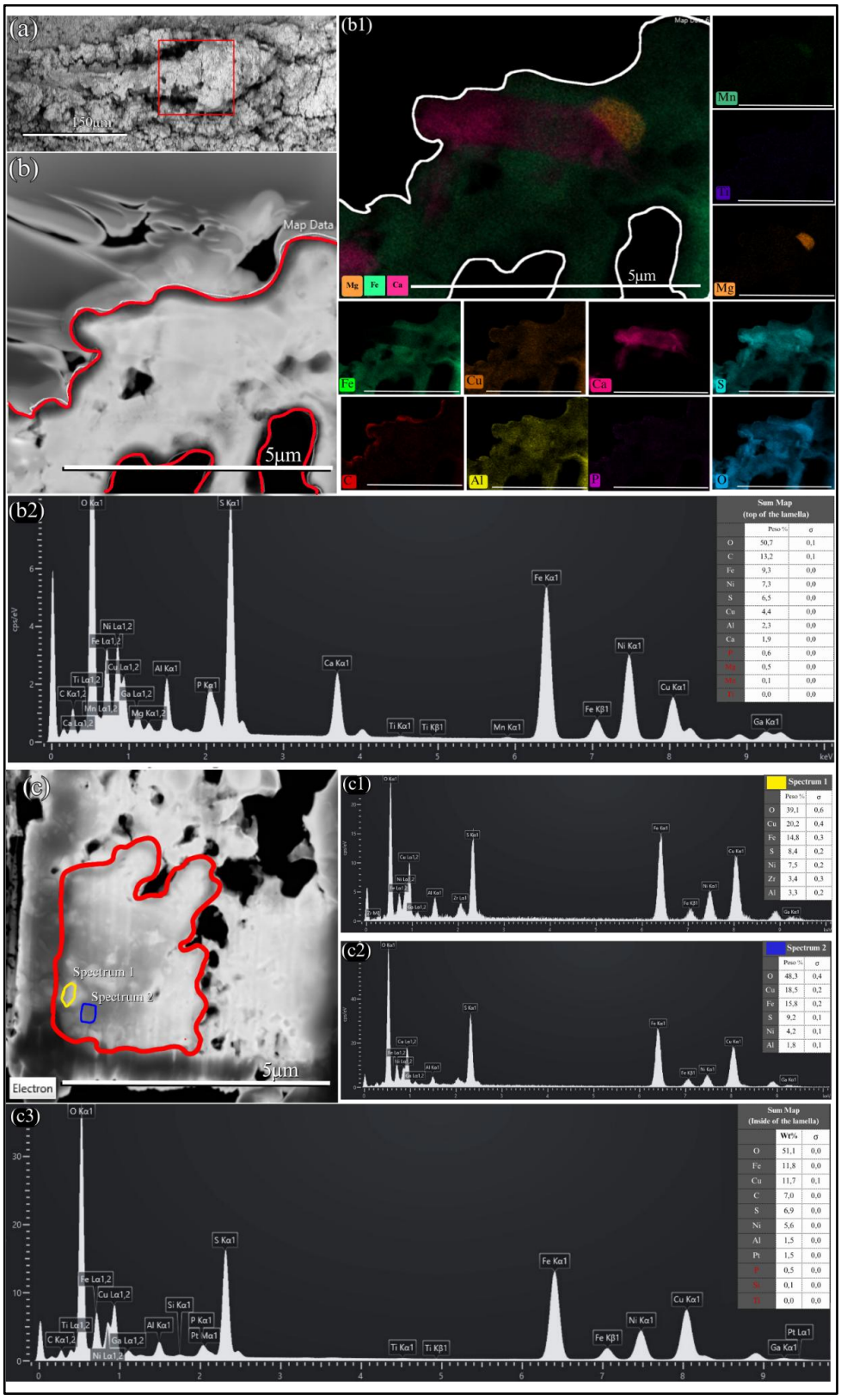

Figure 10. FIB-SEM-STEM-EDS analyses fossilized muscle fiber from the sample GP/1E11237c. **(a)** Micrograph of the muscle fiber from which the lamella was extracted by FIB (Focused Ion Beam); the red rectangle indicates the extraction region. **(b)** STEM image showing the top of the lamella, corresponding to the external part of the fiber. **(b1)** Map with superimposition of the distributions of Mg, Fe, and Ca and elemental maps obtained from the top of the lamella (scale - 5µm). **(b2)** EDS

sum spectrum **(c)** STEM image of the base of the lamella, which represents the internal portion of the fiber.; the blue and yellow circles mark the region of spectral acquisition. **(c1)** EDS spectrum of the areas marked in “c”. **(c3)** Sum spectrum of the analyzed area at the base of the lamella indicated in figure "c". The area marked by the red line in “b - c” in was analyzed by EDS.

3.4.2 Sample GP/1E10609 (Blattodea)

The analyses of sample GP/1E10609 were conducted on an exploratory basis, in several anatomical areas of the fossil insect (Fig. 11a): mainly head (Fig. 11b), abdomen (Fig. 11c; d), cuticle (Figs. 11e; f) and hind limbs (Figs. 11g - i).

The nanometric crystals covering the posterior portion of the head (Fig. 12a) have Fe, Pb and S, which leads to the identification of iron sulfide and/or sulfate, such as pyrite and/or jarosite group minerals enriched in Pb. However, the presence of Pb may suggest the presence of lead sulfide, such as galena (PbS) or similar phases (Figs. 12b; c).

Some crystals of subhedral to euhedral morphology that cover the hip joint region of the right hind leg (Fig. 12c) have a high concentration of Ca, being most likely calcium carbonate, perhaps contamination from host rock calcite ($CaCO_3$) (Fig. 12d).

Still in the same region, a porous texture with euhedral crystals is observed, (Fig. 12e), it is possible to observe a dominant composition of O, S, Fe, and Pb, along with traces of N, indicating complex mineral phases. These phases were identified as iron sulfates (possibly ammoniated) and lead sulfides, the latter potentially corresponding to galena (Fig. 12f; g).

In the metathorax/abdomen region, the shape of the crystals matches that of preserved biological structures, supporting the interpretation of a biological origin (Fig. 12h) composed of O, Fe, S, but with a considerable presence of C and N (Fig. 12i), once again suggesting the presence of sulfated iron mineral phases. Due to the presence of N, we consider the presence of ammoniojarosite ($(NH_4)Fe_3(SO_4)_2(OH)_6$) as a possibility, alongside other potential members of the jarosite group. The detected carbon may be associated with carbonate phases or, alternatively, with organic compounds.

The minerals that preserve the muscle fibers in the right hind leg of the fossil (Fig. 12j) are composed mainly of O, C, Ca, S and P (Fig. 12k). A significant presence of calcium and phosphorus is possibly associated with calcium phosphates. The detected C may indicate remnants of organic matter, but it is more likely related to contamination or interference from the host rock.

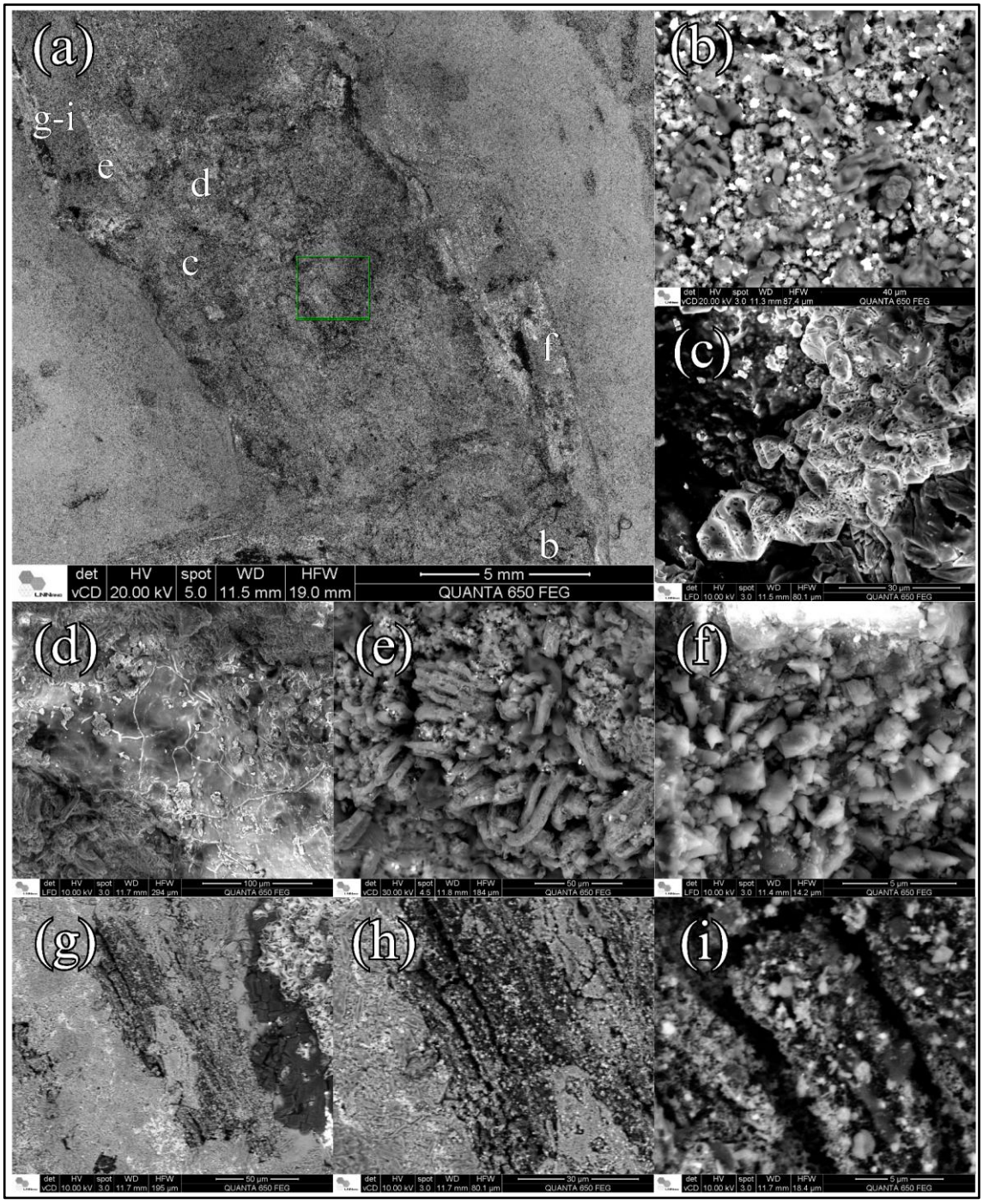

Figure 11. SEM micrographs of sample GP/1E10609**. (a)** General view of the fossil with highlighted regions shown in panels (b–i). **(b)** Fine dispersed anhedral crystals with high brightness over a granular substrate. **(c)** Porous texture with predominantly anhedral crystals. **(d)** Preserved surface with branched linear structures over granular regions, suggesting fine fractures distributed on the cuticle or, alternatively, poorly preserved cuticular ornamentations with secondary infill. **(e)** Thin, elongated, and parallel structures preserved within the internal region of the fossil. The observed organization and morphology are consistent with structures of possible biological origin. **(f)** Compact texture with euhedral crystals. **(g–i)** Muscle fibers preserved in the posterior femoral region of the fossil, showing parallel orientation and a continuous filamentous pattern. **(g)** General view of the region showing organized elongated bundles. **(h)** Intermediate magnification highlighting the linear

texture and parallel arrangement of the fibers. **(i)** High-magnification detail revealing well-defined contours.

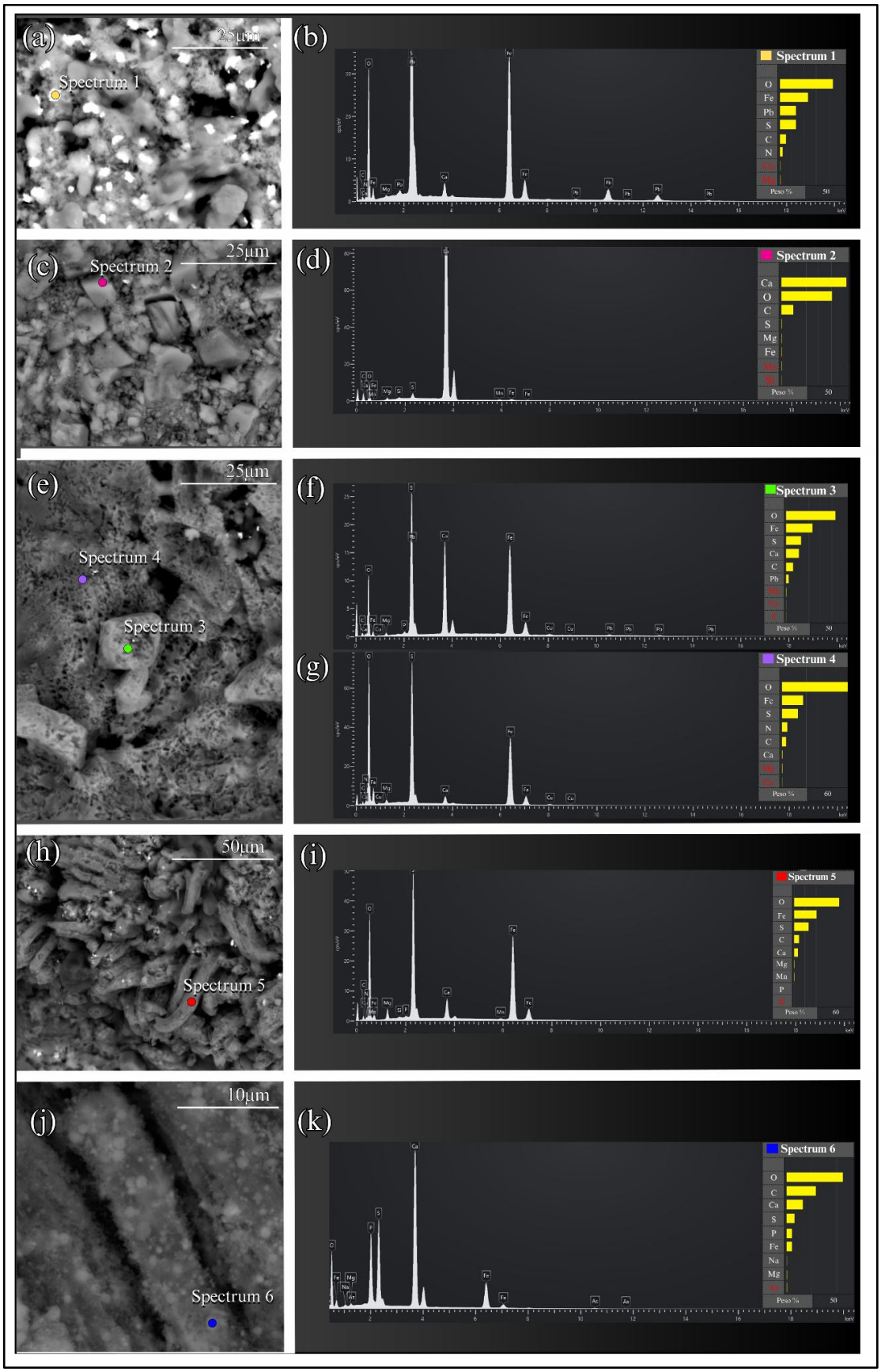

Figure 12. SEM-EDS of sample GP/1E10609. **(a)** Euhedral nanometric crystals covering rhombohedral crystals. (b) Spectrum of micrometric crystals possible galena, or iron sulfate enriched

in Pb. **(c)** Crystals with subhedral to euhedral morphology that preserve the inner part of the cuticle. **(d)** Spectrum of micrometric crystals, possible galena, or iron sulfate enriched in Pb. **(e)** Micrograph of porous textured crystals, with euhedral crystals **(f - g)** Spectrum of porous texture. **(h)** Structures suggestive of biological origin. **(i)** EDS spectrum of organic material. **(j)** Muscle fiber **(k)** Spectrum of muscle fiber showing calcium phosphate present on the surface of the fibers.

3.4.3 GP/1E10501 (ORTHOPTERA)

In the hind legs region, delicate structures such as “trichomes” or spines (“arrows”) are observed on the hind legs of the fossilized insect (Figs. 13a - c). In addition, muscle fibers are preserved throughout the abdominal region (Figs. 13d - f). These structures occur as elongated and parallel bundles, with a rough surface texture and regular micrometric spacing between units. The observed morphology is characteristic of fossilized muscle fibers, whose organization in continuous lines strongly resembles the architecture of muscle bundles with longitudinal patterns (e.g., [41-42]).

The muscle fibers (Fig. 13g) are dominantly composed of O, Ca, P, followed by lower counts of Fe and C (Fig. 13h). The predominance of calcium (Ca) and phosphorus (P) suggests a contribution of calcium phosphates in the preservation of muscle fibers. The presence of Fe and S suggests sulfur-bearing iron minerals, such as pyrite (FeS_2) or derived oxidative forms, such as minerals from the jarosite group (XFe3+3(SO4)2(OH)6), considering the important contribution of oxygen.

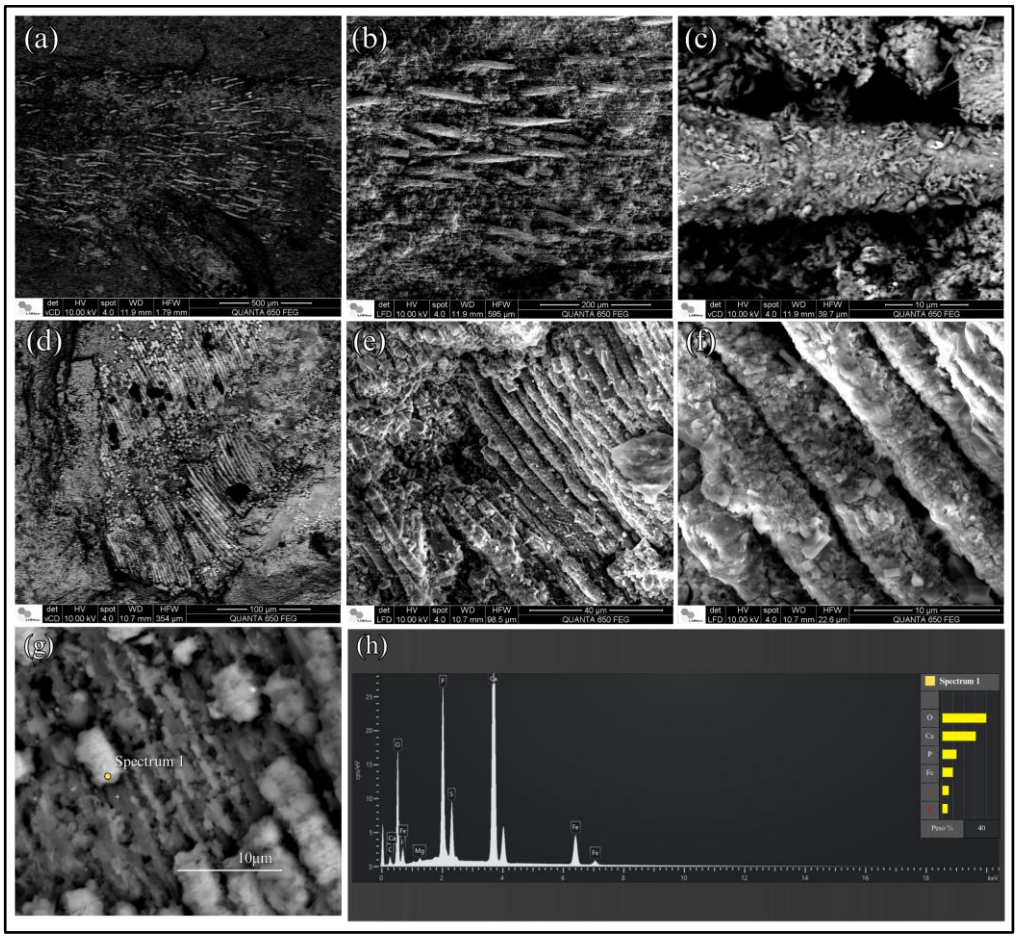

Figure 13. SEM-EDS of sample GP/1E10501. **(a)** General view of the hind leg region of the fossil showing fine projections distributed across the surface. **(b)** Magnification of the same area, highlighting the dense and aligned pattern of these structures. **(c)** High-magnification detail revealing a single elongated and pointed structure, with morphology consistent with preserved cuticular trichomes or spines. **(d)** General view of the insect's abdominal region showing parallel muscle bundles with a regular linear pattern. **(e)** Detail of the bundles showing slightly rough surface texture and micrometric spacing between fibers. **(f)** Higher magnification revealing fiber individualization with well-defined contours, consistent with preserved filamentous muscle morphology. **(g)** EDS of muscle fibers. **(h)** Corresponding EDS spectrum showing a predominance of oxygen (O), calcium (Ca), and phosphorus (P), with the presence of sulfur (S) and iron (Fe), suggesting mineralization by calcium phosphates and a contribution from iron sulfates.

3.4.4 GP/1E10836 (BLATTODEA)

In the micrographs of sample GP/1E10836 (Fig. 14), three main areas of the fossil were analyzed, the wing, the thoracic region, and the left side of the posterior portion of the abdomen (Fig. 14a).

In some areas of the thorax, juxtaposed euhedral micrometric crystals are observed, forming a rhombohedral texture (Fig. 14c).

During characterization by optical microscopy, it was possible to observe details of the insect's wing, in which the pyrite framboids, with their original yellowish coloration, are exceptionally well preserved, outlining the wing veins (Fig. 14b).

In the abdominal region, crystals arranged in rosette-like textures occur locally (Figs. 14d; e), partially covered in some areas by nanocrystalline phases that suggest alteration processes (Fig. 14f), and gradually merge into framboidal pyrite aggregates, which may indicate that the rosettes result from the progressive oxidation of framboids (Figs. 14g; h). These framboids exhibit filamentous structures resembling webs, which could be interpreted as EPS, but are more likely to represent the initial stages of oxidative alteration, eventually evolving into rosette-like textures. Framboidal pyrite predominates across most of the exoskeleton and exceptionally preserves its original ornamentation (Fig. 14i).

The well-developed rosette morphology suggests high crystallinity, compatible with primary sulfate precipitation, but their association with framboidal pyrite and local signs of mineral alteration may also point to diagenetic transitions. Although studies show that jarosite rosettes can form rapidly under controlled conditions [43-44], such environments differ markedly from natural settings. Therefore, both possibilities remain open.

In addition, other abdominal regions are composed of aggregates of elongated subhedral to anhedral crystals, some of which display euhedral terminations (Figs. 14j, k).

The rosette-like textures that partially cover the framboidal pyrite crystals (Figs. 14c) are, in turn, overlain by granular, prismatic, or acicular crystals (Fig. 14f). These crystals are composed of O, S, and Fe, with a considerable amount of Na (Fig. 14l). This composition may correspond to sodium sulfates, such as mirabilite ($Na_2SO_4 \cdot 10H_2O$) or thenardite (Na_2SO_4), or to gypsum ($CaSO_4 \cdot 2H_2O$). Alternatively - though less likely - they may represent iron sulfates of the jarosite group enriched in sodium, such as natrojarosite ($NaFe^{3+}_3(SO_4)_2(OH)_6$) (Fig. 14m).

There is also a considerable contribution of C in the composition of these sulfates, which may indicate the presence of organic matter or interference from the carbonate host rock (Fig. 14o). The surface of pillar-shaped crystals is composed entirely of O, Fe and S elements, evidencing the presence of iron oxide-hydroxide such as goethite or hematite, however, morphology is like jarosite crystals enriched in Cr (e.g. [45]).

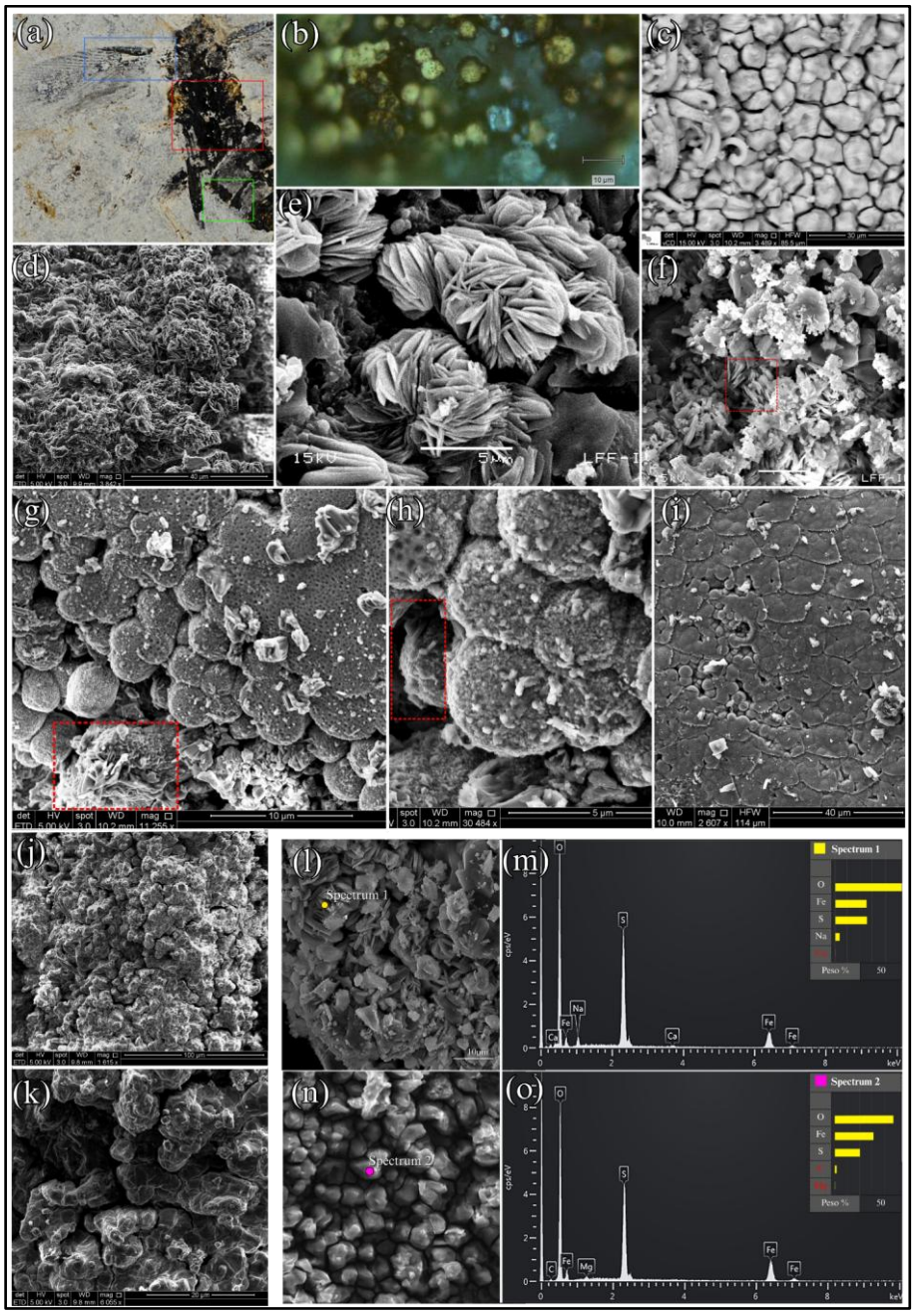

Figure 14. SEM-EDS of sample GP/1E10836. **(a)** Sample with measurement areas marked: blue – wing; red – thoracic region; and green – abdominal region. **(b)** Framboidal pyrite preserving the veins of the left wing highlighted by the blue rectangle in "a". **(c)** Juxtaposition of euhedral microcrystals, forming a rhombohedral texture. **(d)** Cluster of placoid crystals organized in rosette habits, covered by crystals in a finely crystalline mineral phase. **(e)** Well-developed rosette with preserved radial organization and defined contours. **(f)** Granular, prismatic, and acicular nanocrystals cover previously formed rosette structures, suggesting a process of surface alteration or late-stage diagenetic remineralization. The rosettes are indicated by a red dotted rectangle. **(g - h)** Pyrite framboids covered by structures outlined with a red dotted rectangle, which may represent mineralogical transitions to iron sulfates or exopolysaccharides (EPS) secreted by sulfate-reducing bacteria. **(i)** External ornamentation of the exoskeleton preserved by pyrite framboids. **(j - k)** Euhedral crystals. **(l)** SEM-EDS analysis of crystals covering rosettes. **(k)** Spectra of iron sulfate. **(i)** SEM-EDS of euhedral crystals. **(m)** EDS spectrum of the euhedral crystals.

4 DISCUSSIONS

4.1 PRESERVATION OF MORPHOLOGICAL FIDELITY

The insect fossils from the Crato Lagerstätte present structures preserved with high anatomical fidelity, mainly muscle fibers (Figs. 8; 11; 13). Two processes are responsible for this exceptional preservation in the Crato Fm. - kerogenization in “GL” and pyritization in “BL” [09, 46]. The pyritized fossil insects are three-dimensional, have a reddish-brown coloration with orange oxidation halos, and tend to present a greater degree of disarticulation. This aspect reflects advanced decomposition before mineralization or rupture of the tegument, enabling the entrance of reagents in the carcasses [47]. In addition, soft tissues and internal structures, such as muscle fibers, ommatidia, proventriculi and reproductive organs, such as ovaries, can also be preserved [6, 7, 10, 12, 47, 48]. Despite the frequent disarticulation observed in many specimens, the anatomical fidelity is notably superior to that observed in kerogenized fossils from gray limestone [47].

Kerogenized fossil insects are two-dimensional and exhibit black coloration in specimens, resulting from the concentration of amorphous carbonaceous material. They are generally less disarticulated, due to rapid burial, and exhibit preservation of limited morphological structures, restricted mainly to the general silhouette of the body [46]. They usually include fragments of ornamented cuticle, all preserved limbs, wings and antennae, although with a low degree of detail, resulting in less anatomical fedelity [6, 10, 33, 46, 47].

The preservation of fossil insects analyzed in this study (GP/1E11237c; GP/1E10609; GP/1E10501; GP/1E10836) reveals the coexistence of pyritization, sulphatization, and subordinate phosphatization. Although kerogenization is traditionally associated with fossils from the “GL” subfacies in the Crato Lagerstätte [6, 8, 9, 33, 46], no carbonaceous films were identified in the specimens examined here. The samples exhibit chromatic variations ranging from black, which may resemble kerogen, to reddish-brown with orange oxidation halos - all related to pyritization and its subsequent oxidation - and to white-beige tones associated with sulphatization and subordinate phosphatization [7, 9]

According to Dias & Carvalho [6], the beige limestone “BL” subfacies, where pyritization occurs, reflects arid paleoenvironmental conditions, associated with shallow and isolated lakes, with low water renewal rates and limited hydrodynamic activity, which favored the proliferation of microbial mats. These conditions created anoxic microenvironments inside the mats, rich in iron and sulphate, ideal for sulfate-reducing

bacteria that induced the early precipitation of pyrite in decomposing organic tissues. In contrast, the gray limestone "GL" subfacies is associated with preservation by kerogenization, in which organic matter is transformed into kerogen — an amorphous and insoluble carbonaceous material, originating from the incomplete degradation of organic compounds. Although the schematic model proposed by Bezerra *et al.* [33] suggests that kerogen formation in the dark/blue-colored limestone ("DL") occurs through acetoclastic methanogenesis, in which acetate (CH_3COO^-), produced by bacterial activity, is converted into methane (CH_4) and bicarbonate (HCO_3^-), the authors do not provide detailed justification for the inclusion of this process. The rapid migration of the carcass to deeper sedimentary layers limits the complete oxidation of organic matter and favors its stabilization in the form of carbonaceous films [33]

The coexistence of these different taphonomic signatures in a single fossil specimen hosted within gray limestone represents an unprecedented condition in the Crato Lagerstätte, offering empirical evidence for the hypothesis of a taphonomic gradient acting on the depositional setting. These observations challenge the dichotomy previously proposed (e.g., [6, 9, 46]), which considered the existence of two distinct taphonomic regimes — one associated with pyritization in beige limestones and the other with kerogenization in gray limestones.

4.2 Distribution of chemical elements and taphonomic implications

Spearman correlation analyses of chemical elements quantified by XRF confirmed patterns of geochemical compartmentalization between fossils and host rock in samples GP/1E11237c and GP/1E10609 (Fig. 6). However, internal color variations within the fossils did not show statistically significant differences in elemental composition (Kruskal-Wallis test) (Fig. 7).

In the heatmap of Spearman correlations (Fig. 6), relevant patterns were observed. The strongest positive correlations occurred between Fe and S ($\rho \approx +0.91$), Fe and Cu ($\rho \approx +0.98$), Fe and Pb ($\rho \approx +0.98$), and Fe and Cr ($\rho \approx +0.90$), followed by associations between Fe and Co ($\rho \approx +0.85$) and, to a lesser extent, between Co, S, and Pb ($\rho \approx +0.83$). All these pairs exhibited p-values near zero, indicating statistically robust associations consistent with pyritization processes during early reducing diagenesis.

These elements form a cohesive group with strong intercorrelation, suggesting codistribution and possible coprecipitation in sulfidogenic environments. Manganese (Mn) showed a moderate positive correlation with Sr ($\rho \approx +0.63$), which may indicate joint mobilization in specific microenvironments, although with weaker statistical support. Notably, Mn and Sr were the only elements to display near-neutral correlations with Ca; however, the high p-values rendered these associations statistically insignificant (see Fig. 6). In contrast, calcium (Ca) showed negative correlations with Fe ($\rho \approx -0.57$) and Pb ($\rho \approx -0.59$), reflecting a geochemical behavior opposite to that of the pyrite-associated group. It is important to emphasize that negative correlations do not necessarily imply direct chemical antagonism but rather indicate spatial dissociation — for example, between fossils and the surrounding matrix. Elements such as P, K, and Zn showed weak or inconsistent correlations with the main identified groups ($\rho < 0.7$), suggesting more localized and less systematic incorporation mechanisms. In the case of phosphorus, its potential involvement in internal phosphatization processes may explain this variability; however, the low P counts in several samples likely limited the statistical strength of the observed correlations.

Iron and sulfur were enriched in fossil-bearing regions, along with trace elements such as chromium, cobalt, copper, lead, and zinc, suggesting pyritization and possible metal incorporation into pyrite or presence of undetected mineral phases [49-51]. Cobalt replaces Fe^{2+} via isomorphic substitution in reducing environments [52], while lead tends to precipitate as sulfide (PbS, galena), and can also be incorporated into pyrite, affecting the incorporation of other ions [53].

The copper initially binds to organic matter and may be released into sediment pores during decay, reacting with sulfide ions to form copper sulfides [49, 54]. It may be incorporated into pyrite under slow, stable growth, or precipitate as chalcopyrite inclusions under unstable chemical conditions [53]. In some cases, Cu^{2+} is incorporated when As^{3-} replaces S in the structure, creating favorable sites [55].

Zn appears as submicroscopic sphalerite (ZnS) inclusions or via coupled substitution with Cu^{+} and As^{3-} [56]. It can be remobilized during pyrite oxidation and retained by iron oxides [57] or react with sulfur to form new sphalerite [58]. The absence of As in the samples

suggests these elements occur as inclusions or diagenetic products, not through crystallographic substitution.

Chromium may be adsorbed or coprecipitated with sulfides [55], while Íons potássio (K^+), além de estarem presentes em minerais detríticos, podem favorecer ativamente a formação de jarosita em zonas oxidantes ao intensificar a oxidação bacteriana de ferro ferroso (Fe^{2+}) para ferro férrico (Fe^{3+}), como observado em sistemas do tipo $FeSO_4$–K_2SO_4–H_2O [59]. Phosphorus appears in preserved soft tissues, consistent with early phosphatization [8]. Barium occurs locally and suggests barite precipitation in reducing microenvironments [60]. Mn, Ca, and Sr are correlated and likely undergo mutual substitution in carbonate phases [61-62] Further discussion of these geochemical processes is provided in (Supplementary 1. Geochemistry).

4.3 Mineralogy and textural aspects of the Crato insect fossils

Raman analyses performed on samples GP1E11237c, GP1E10609 and GP1E10501 revealed mineralogical variation at black and beige-colored areas of the fossils. Raman analyses of the beige-colored spots in samples GP/1E11237c and GP/1E10609 revealed bands characteristic of minerals of the jarosite group [$XFe_3(SO_4)_2(OH)_6$, with X representing, usually, a monovalent cation such as K+, NH4+, H3O+, etc.]. In contrast, the dark-colored areas are dominated by gypsum ($CaSO_4$) and pyrite (FeS_2), the latter widely recognized as a recurrent early diagenetic product in the Crato Lagerstätte fossils [08-09]. In this work, we describe for the first time the presence of jarosite as a mineral phase associated with the pyritization of the Crato paleolake fossils. Jarosite belongs to the group of alunite-type ferric sulfates, with general formula $XFe_3(SO_4)_2(OH)_6$, and is typically formed in acidic and slightly oxidizing environments, by oxidation of pyrite in the presence of oxygenated waters [63-68].

The co-precipitation of pyrite and minerals of the jarosite group (whether natro, plumbo, ammonium or hydronium jarosite) in sedimentary environments is unlikely since these mineral phases form under contrasting geochemical conditions. Pyrite precipitates in anoxic contexts rich in organic matter, typical of the sulfate reduction zone [69-70], while jarosite group minerals tend to form later, during acidification of the environment resulting from the retrograde oxidation of pyrite [64]. Thus, it is more appropriate to interpret the presence of iron sulfate minerals of the jarosite group as being the product of post-

pyritization phases in systems with dynamic redox gradients. Although we considered the presence of minerals from the jarosite group ($XFe_3(SO_4)_2(OH)_6$) in the Raman spectra and were able to infer its presence in the fossils, we did not observe the presence of potassium in the SEM-EDS analyzes. This aspect may suggest that jarosite occurs as substitutions of the K+ ion by Na^+, $Pb^{2+,}$ $NH4^+$ and even H_3O^+, forming natrojarosite ($NaFe_3(SO_4)_2(OH)_6$), plumbojarosite ($Pb_{0.5}Fe_3(SO_4)_2(OH)_6$), ammoniojarosite ($(NH_4)Fe_3(SO_4)_2(OH)_6$) and/or hydroniumjarosite ($(H3O)Fe_3(SO_4)_2(OH)_6$) since we were able to observe iron sulfates with Na, Pb and N. The origin of the incorporated NH_4^+ to jarosite is still uncertain, as there are no reports that the sedimentary environment where the fossils are located is naturally enriched with this ion. However, the formation of the potassic member of the jarosite group is highly favored [71] and, according to [66], ammonium jarosite is very rare in natural environments, as it requires ammonium sources from the decomposition of organic matter or from microbial activity in the near absence of potassium.

Although it is well established that iron sulfates precipitate from the oxidation of sulfides, the data obtained from the samples suggest that this process may, in fact, have occurred inside the fossils. Iron sulfate crystals were observed exclusively in internal regions of beige-colored areas, often associated with soft tissues or degraded organic structures, while framboidal pyrite remains preserved especially in the cuticle region.

Pyritized fossils in beige limestone (BL) underwent more intense oxidative processes and present the formation of hematite (Fe_2O_3) [8] and goethite ((FeOOH) pseudormorphs [33]. On the other hand, pyritized fossils in gray limestone (GL) in this study indicate that minerals of the jarosite group can form as subsequent phases to pyritization. This suggests that, while in the BL fossils pyrite tends to be transformed into iron oxides and hydroxides under oxidation, in the GL fossils jarosite may represent an intermediate phase of oxidation in microenvironments richer in organic matter. Jarosite is not a stable mineral and, when hydrolyzed and exposed to a more neutral to acidic pH environment, it can be replaced by ferric phases such as goethite [72] and hematite, in the case of Martian jarosite when exposed to moderate temperature increases and drier environments [73-74].

The presence of a band at 982 cm^{-1} in the Raman spectrum is indicative of the sulfate group but is not exclusive to a single mineral. Several hydrated sulfates share bands in this range, which can lead to ambiguities in mineralogical identification based solely on this band [75]. For an accurate assignment, it is recommended to consider other characteristic bands in the Raman spectrum. Sample GP/1E10501 is completely black-colored and presents

pyrite (341 and 342 cm^{-1}), characteristic bands of calcium phosphate (960 cm^{-1}), gypsum (1008 cm^{-1}) and calcite (1081 and 1089 cm^{-1}), in addition to the sulfate band at 982 cm^{-1}.The typical calcium phosphate band with a weak signal at 960 cm^{-1} corroborates the subordinate fossilization seen in previous studies preserving soft tissues at the Crato Lagerstätte [7, 8, 48]. Calcite ($CaCO_3$) is identified in samples from the Crato Formation as part of the carbonate host rock, both in the beige limestone and in the gray limestone [8, 10].

Some areas of sample GP1E10501 exhibited broad bands at 1192 and 1272 cm^{-1}. Similar bands (1211 and 1296 cm^{-1}) were identified in insect fossils from the Crato Formation as typical of amorphous carbonaceous compounds, being associated with the D4 defect band and the CH_2 fold, respectively [33]. These bands are interpreted as indicative of kerogenization, reflecting possible structural remnants of biomolecules subjected to diagenetic degradation under anoxic conditions.

In the samples analyzed here, such bands appear exclusively in dark-colored areas exhibiting well-preserved fossil morphology, which favors the hypothesis of differential preservation of organic compounds. This interpretation is supported by [76], who describes bands in this range (~1186–1200 cm^{-1}) as associated with C–C and C–O stretching modes, frequent in bacterial polysaccharides and exopolysaccharides. Additionally, [77] point out that the band close to 1293 cm^{-1} can be attributed to the Amide III mode of peptide chains, reinforcing the possibility of preservation of biopolymers such as chitin or collagen [78] observed a band at 1284 cm^{-1} associated with the CH_2 vibration in organic inclusions in amber, supporting the possibility that bands in this range represent preserved molecular residues. However, it is important to consider an alternative interpretation, as discussed by [36]. These authors observed that similar bands, in the range of 1190 to 1300 cm^{-1}, may appear in Raman spectra obtained with a 785 nm laser due to fluorescence associated with the presence of rare earth elements, especially Nd^{3+} (neodymium), which can be incorporated into minerals such as calcium phosphate or even adsorbed on crystalline surfaces. In these cases, the bands do not represent real vibrational modes, but secondary emissions induced by laser excitation. Despite this caveat, the morphology of the bands at 1192 and 1272 cm^{-1} in the samples studied here — symmetrical, with regular contours and systematic occurrence only in fossiliferous areas — differs from the typical spectral patterns of spontaneous fluorescence [36-39]. The absence of emission tails, erratic fluctuations and lateral artifacts, combined with the co-occurrence with phases such as pyrite and calcium phosphate, suggests that these bands are of legitimate vibrational origin, although their exact attribution remains

partially ambiguous. Thus, although considering previous studies [33, 77, 78], the influence of secondary optical effects, such as fluorescence induced by Nd^{3+} or other luminescent ions, is the most plausible interpretation. Confirmation of the nature of these bands therefore requires complementary approaches.

The SEM analyses revealed mineralization patterns that are in line with the results obtained in XRF and Raman micro spectroscopy, both in terms of chemical composition and spatial distribution of the minerals. In the fossil cuticle, we observed framboidal pyrite preserving the cuticle (black-colored areas) (*e.g.* Figs. 14g; h), which is corroborated by the high Fe and S counts in these regions by XRF (Fig. 3) and by the strong statistical correlations between these elements (Fig. 6a), as well as by the Raman bands around 340 cm^{-1} (Figs. 7). Inside the specimens (beige-colored areas), especially along preserved muscle fibers, EDS and Raman data revealed jarosite-type iron sulfate (*e.g*. Figs. 8; 11; 13). Despite the identification by other techniques, only SEM imaging demonstrated the occurrence of calcium phosphate mainly to the interior of the fossil.

The framboids (Fig. 14g) are comparable to those described by [8], for the cuticle of insects from the Crato Lagerstätte (BL facies). These crystals were also described in fossil insects from the Jehol Biota, China, as observed in the cuticle and covered by web-like structures attributed to EPS [79]. In our material, we also observed that these crystals are covered by elongated structures with undefined morphologies, which may suggest post-depositional alteration or possible remnants of EPS (Figs. 14g; h). However, we interpret that it is a transitional phase of the pyrite framboids to form iron sulfate with a rosette habit like jarosite (that could be alternatively gypsite), representing the early stages of oxidation, possibly mediated by microbial activity [80]. The euhedral crystals (Figs. 14j; l) are very similar to the jarosite crystals with Cr inclusions described by [45]. Studies indicate that framboidal pyrite is highly susceptible to oxidation [81-82], which would be even more critical in the outermost portion of the fossil, which is closer to fractured zones and weathering. In this scenario, there may be oxidation of sulfide to iron sulfates such as goethite and hematite, a process already recorded in beige limestone fossils from the same formation [6, 8, 24, 33]. However, this oxidation may not occur or may be delayed in environments that remain anoxic, with high BSR activity and poorly permeable fine sedimentation associated with calcitic carbonates [83-86]. The partial integrity of framboidal pyrite, with only subtle oxidative overprinting, supports the interpretation that local redox conditions were not fully oxidizing, having remained reducing at least in the cuticle.

STEM-EDS images of the FIB-prepared lamellae revealed that the interior of the muscle fibers contains nanocrystals enriched in Fe, S and Cu, perhaps pyrite or chalcopyrite, which were not detected by surface EDS. This suggests that jarosite may have formed secondarily during post-early diagenesis, by oxidation of primary sulfides since there is trace evidence of these phases still preserved within the tissues.

The distribution of framboidal pyrite at the cuticle of the fossils, whereas soft tissues have finer pyrite textures internally, covered by sulfates and phosphates, reveal the complexity of the preservational pathways in the Crato Lagerstätte. In this sense, this work demonstrates that complex taphonomic signatures require integration of techniques, able to recognize distinct processes that can occur within a single fossilized specimen.

4.4 TAPHONOMIC MODEL

4.4.1 REVIEW OF THE CURRENT STATE OF KNOWLEDGE

The current conceptual model of the Crato Lagerstätte considers that the fossils of *Dastilbe* and insects in laminated "yellow-beige" limestone exhibit pyritization (subsequently altered to iron oxides/hydroxides, with a yellow-brown color), whereas fossils in the "blue-gray" limestone were preserved mainly as carbonaceous compressions (kerogenized organic films, dark in color) [8, 9, 46]. Bezerra *et al.,* [46] identified a fossil cockroach preserved exclusively as carbonaceous compression in gray limestone, if this duality would also occur in the insect fossils of the Crato Lagerstätte. These taphonomic pathways are linked to two distinct paleoenvironmental scenarios. The first, associated with the formation of the beige limestones, reflects drier climatic conditions in a shallow, more saline, and stagnant lacustrine environment, favoring the proliferation of microbial mats. The second depositional scenario, associated with the gray limestones, reflects an increased freshwater input into the lake system, resulting in deeper and lower-salinity waters under a more humid climatic regime [6]

Schiffbauer *et al.,* [87] point out that such preservation processes do not always follow rigid stratified divisions. Instead, they propose a unifying model based on the Ediacaran biota of the Gaojiashan Formation, located in southern China, where fossils exhibit a continuous preservational spectrum - from three-dimensional pyritization to two-dimensional carbonaceous compressions. From this context, the authors suggest that pyritization and kerogenization represent extremes of a continuous taphonomic gradient,

controlled mainly by the post-burial sedimentation rate and the thickness of microbial zones (such as the sulfate reduction zone and the methanogenic zone). Thus, the nature of the preservation mode depends not only on the depositional environment itself, but on the dynamics of exposure of the carcass to different redox conditions throughout its *postmortem* trajectory.

Osés *et al.* [9] adapted the taphonomic preservation gradient model of Schiffbauer *et al.* [87] to the fossil record of the Crato Formation, suggesting that pyritization and kerogenization would represent extremes of a continuum controlled by environmental and taphonomic variations. However, this proposal remained in the conceptual field, to be proven by evidence of such a gradient throughout the Crato Lagerstätte.

Later, Bezerra *et al.* [33] described a case of mixed preservation in fossils from this unit, specifically in an Ephemeroptera specimen. The authors observed the coexistence of pyritization and carbonaceous material compatible with kerogenization in the so-called yellow limestone ("YL"). Thus, if the "YL" of Bezerra *et al.* [33] corresponds to the beige limestone (BL) subfacies, then the pyritization described in their study would still be restricted to this subfacies. This spatial and environmental limitation reinforces the interpretation that pyritization, even when accompanied by organic matter, may not occur continuously throughout the basin. However, the evidence presented here indicates insect fossils pyritized in gray limestone.

4.4.2 An Integrative Taphonomic Framework: Pyrite, Sulfates and Phosphates

The new findings of pyritic insects in the gray limestone of the Crato Formation require a reevaluation of the taphonomic models previously proposed for this Lagerstätte. The specimens discussed here might indicate hybrid preservation, combining elements of both pathways (pyritization and kerogenization; but see discussion in the Raman spectroscopy topic). These insects occur at the gray limestone facies (theoretically corresponding to the "kerogenization zone"; [9] but exhibit framboids of fresh pyrite and organic matter in the cuticle coexisting with an internal infilling of sulfates and phosphate. Differently than expected for this facies, this is not just a flat carbonaceous film [33]: there BEare three-dimensional soft tissues preserved by diagenetic minerals, conferring a high degree of preservation. These aspects demonstrate that the lithofacies dichotomy is not absolute for the Crato Lagerstätte since reducing microenvironments provided the necessary

conditions for pyritization during accumulation of beige and dark-colored limestones [9]. Therefore, the two preservation modes represent endmembers of a taphonomic gradient controlled by sedimentation rates and organic matter content. A multistage process is proposed below.

(a) Pyrite: Preservation by pyritization results in the replacement of organic matter by pyrite (FeS_2), a mineral that forms by precipitation in anoxic or hypoxic environments, mediated by the action of sulfate-reducing bacteria. These bacteria degrade organic compounds and release sulfide (H_2S), which reacts with iron (Fe^{2+}) dissolved in the pores of the sediment, promoting the nucleation of pyrite crystals [8, 88]. Mineralization occurs early, during the initial stages of decay, while the carcass remains in the sulfate reduction zone (SSR), enabling detailed replication of soft tissues and delicate anatomical structures [9]. In the study of fishes from the Crato Lagerstätte, [9] argued that slower sedimentation rates in certain microfacies allowed the carcasses to remain longer in the sulfate reduction zone, resulting in extensive pyritization. In the GL microfacies, faster burial placed the carcasses in the methanogenic zone earlier, limiting pyritization and favoring the conservation of organic material (kerogenization).

Applying this rationale to the insects of the Crato Formation, we can imagine that even within the gray limestone (associated with lower sulfate input or higher organic content; Dias & Carvalho [6], certain individuals may have experienced circumstances comparable to those in the beige limestone – for example, residing long enough in the sulfidic zone, or having a local microenvironment with high availability of sulfate. Thus, intermediate preservation emerges naturally in a continuum, and the fossils possibly represent such an intermediate case, comprising pyritized samples (so far characteristic of the BL preservation mode).

Even so, the limiting conditions of pyritization in the gray limestones (see [9]) seem to have restricted this process predominantly to the cuticle region. According to Osés *et al.* [8], the exclusive occurrence of framboidal pyrite in the cuticle, and not inside the fossils, can be explained by the balance between the diffusion rates of ions (Fe^{2+} and SO_4^{2-}) and the nucleation rates of pyrite during the organisms decay. Initially, the rapid decay of the cuticle would have yielded several nucleation sites, leading to the framboidal texture. Since the cuticle maintains greater contact with the sedimentary pores and thus with the continuous influx of ions from the environment, this favors the formation of larger framboids, while the internal regions, with lower diffusion of ions and rapid consumption of more labile organic

matter by sulfate-reducing bacteria, tend to present smaller framboids, a finer texture (Fig. 14g) or even absence of pyrite, with the exhaustion of environmental sulfate and iron, plus the barrier created by the framboids that replicated the cuticle. Indeed, we did not verify the presence of pseudomorphs of pyrite nanoframboids (sensu Osés et al., [8]; inside the insects in BL) within the studied fossils.

(b) Iron sulfates + phosphate: The carcasses were filled by jarosite-type iron sulfate ($XFe_3(SO_4)_2(OH)_6$) in association with calcium phosphate. Jarosite can form biogenically, mediated by iron-oxidizing bacteria in acidic, potassium-rich environments, either through the transformation of precursor phases such as schwertmannite or directly from the oxidation of pyrite. A formação de jarosita como mineral secundário pode ocorrer durante a dissolução microbiana da pirita por *Thiobacillus ferrooxidans* (e.g., [89]). Alternatively, it may also precipitate abiotically through the oxidation of iron sulfides in the presence of K^+ under acidic pH conditions [90]. Evidence of this process was found by Odin *et al.* [91] in O_2-enriched microenvironments within a largely anoxic deposit, leading to the precipitation of iron oxyhydroxides and extensive oxidation of pyrite in an acidic context, which produced jarosite as one of the main secondary minerals. In the case of the Crato Formation insects, the detection of sulfur in the internal regions of the fossils accompanied by lower iron contents, and Raman data may suggest iron sulfates formed after oxidation of the original pyrite [92]. Thus, we suggest that, in this scenario, the interior of the fossil was initially stabilized by early calcium phosphate mineralization, which may have prevented the collapse of internal structures [93-94], followed by early pyrite precipitation [8-9], which was later replaced by jarosite, as reported by Odin *et al.* [91]. This scenario would indicate that, after the initial phase of pyritization of the soft tissues, oxidation occurred inside the carcass in a confined acidic environment. Taphonomically, this requires the conversion of iron in the reduced form (Fe^{2+}) to ferric iron (Fe^{3+}), and its combination with remaining sulfate and potassium, ammonium, lead, sodium or hydronium – viable if we consider late micro-oxygenation and release of these elements from the tissues or primary minerals. Therefore, we suggest that the decomposition of internal soft tissues favored preservation by sulfates through the rapid conversion of sulfides. The framboidal pyrite of the cuticle, a more recalcitrant material, did not change to sulfate. Additionally, it is likely that the more continuous exposure of the cuticle to the supply of sulfate and iron inhibited sulphation. Following this line of reasoning, internal sulphation would have been favored by the limitation of pyritization by the barrier that the cuticle formed for the replenishment of

sulfate and iron. The associated calcium phosphate would be a remnant of the early mineralization of P-rich components of the soft tissues, preserving the interior of the fossils by phosphatization [6].

(c) Mix of calcium, barium and iron sulfate + phosphate: The second scenario corresponds to a heterogeneous internal filling, with a mixture of calcium, barium and iron sulfate accompanied by phosphate. This intermediate situation may reflect a spatial variation in the chemical conditions within the carcass, given that calcium and iron sulfates form under different pH conditions. This would explain why we found both gypsum and jarosite filling different regions, in addition to disseminated calcium phosphate associated with soft tissue remains. The combined genesis involves the same processes already described, occurring simultaneously in different micro regions: portions with greater $CaCO_3$ influx from the sediment would have produced calcium sulfate, while less buffered (more acidic) portions would favor iron sulfate and phosphate. From a taphonomic perspective, internal chemical compartmentalization in insects is plausible, as different body regions such as the abdomen and thorax exhibit pH and ionic variations. These differences affect soft tissue preservation, as shown by [95], who observed intestinal microenvironments favoring phosphatization of internal structures.

A localized occurrence of barium sulfate was also detected preserving a putative digestive structure, suggesting an internal microenvironment enriched in barium (Figs. 9g; h). Ba^{2+} accumulation may be related to bioconcentration in Malpighian tubules, where this element has already been observed in insects (e.g., [96]). This specific ionic context, potentially reactive with SO_4^{2-} released from organic decay or pyrite oxidation, could have promoted early barite precipitation. Osés et al. [9] similarly reported Ba–S correlations in kerogenized *Dastilbe* fossils, interpreted as diagenetic barite formed in sulfate-depleted methanogenic zones.

As discussed by Wilby & Briggs [94], small variations in pH during decomposition can trigger a shift between precipitation of carbonate (calcite) and calcium phosphate (apatite), the latter being favored in more acidic microenvironments generated locally around the decomposing carcass. Both gypsum and jarosite may coexist as oxidation products of pyrite in the same fossil under distinct alteration regimes, either during in situ paleo-weathing or post-excavation degradation, as demonstrated by artificial ageing experiments showing gypsum formation on fossil surfaces and jarosite precipitation within body cavities [91]. Thus, the observed mixing indicates a multistep process in which the internal pyrite

was converted to both types of sulfates. In Fig. 9a, b, calcium sulfate seems to occur at the outermost part of the muscle.

In sum, jarosite is restricted to the internal part of the fossils, associated with soft tissues. Our model considers that jarosite was induced by the decay of organic matter of these tissues, besides considering carbonate buffering to jarosite formation externally, thus explaining this distribution. Fresh framboidal pyrite replaces the cuticle, with minor association with sulfates, despite framboidal texture being prone to oxidation, given the surface area/volume ratio and the nanocrystals [97]. Taking all this evidence together, sulphation could have been an early mineralization stage, occurring soon after pyritization, and mostly restricted to the inner part of the fossils. However, comparing photographs along the last years, it seems that the beige internal regions are formed by alteration (Fig. 2). Indeed, the formation of jarosite is fast under meteoric or laboratory conditions [98]. In that case, remaining organic matter could have fueled pyrite alteration to jarosite and/or acidic conditions were not buffered by host rock carbonate, thus accounting for the observed jarosite distribution. On the other hand, it seems that calcium sulfate was the last phase formed (Fig. 9a; b), only preceding iron oxy/hydroxides forming a halo around the fossils (Fig. 2), while sulphate rosettes in another fossil suggests a more primary precipitation (Fig. 14). Therefore, it remains open to debate as to whether at least some of the sulfates are totally very recent phases.

(d) Residual organic matter and reducing microenvironments: As far as could be observed, the insects pyritized in grays limestone did not retain original organic matter, having been fully degraded and/or mineralized, this indicates that the carcass underwent an intense anaerobic decomposition process, mainly via sulfate reducing bacteria (SRBs), which consumed the tissues and generated sulfide for the precipitation of pyrite, as in the beige limestone facies [8].

Basically, the insects functioned as reducing micro-reactors: when buried in the anoxic sediment, a strong reducing microenvironment was formed around the carcass, where the BSRs proliferated using the organic matter as a substrate and sulfate as a reagent, resulting in enrichment in H_2S and subsequent pyritization [8-9]. This process effectively "burns"/oxidizes most of the carbon in the tissues – converting it into microbial biomass, DIC (dissolved inorganic carbon) and mineral precipitates [99]. The analysis shows that the soft parts of the insects in the beige limestone facies were replaced by iron oxides (after pyrite) and practically do not retain original carbon [6,7,8,11,33,46]. This indicates the

existence of distinct reducing microenvironments within the same organism: the exoskeleton-sediment interface probably maintained sufficiently low redox conditions for a prolonged period, favoring the preservation of a recalcitrant fraction of carbon protected by pyrite mineralization. In contrast, the interior of the body reached less negative redox potentials after the exhaustion of the organic material. In other words, the intense reduction zone was concentrated at the periphery of the insect (where framboidal pyrite nucleated in the cuticle) and depleted all organic matter from adjacent tissues, while the interior, after consuming its nutrients, lost its reducing potential.

This differential decomposition scenario reflects redox microenvironments: strongly reducing immediately after death (during pyritization) and gradually less reducing as organic resources are depleted. The visible consequences are fossils with very high mineral anatomical fidelity, but with an almost total absence of original material, unlike the kerogenized fossils. It is worth noting that in other contexts, when the environment becomes rapidly methanogenic (with low availability of sulfate), residual organic material may remain (kerogenization), as described for other GL fossils [9]. The findings presented here not only provide a more precise understanding of the taphonomic processes involved but also broaden the scope for future investigations into the exceptional preservation of fossils in other Konservat-Lagerstätten.

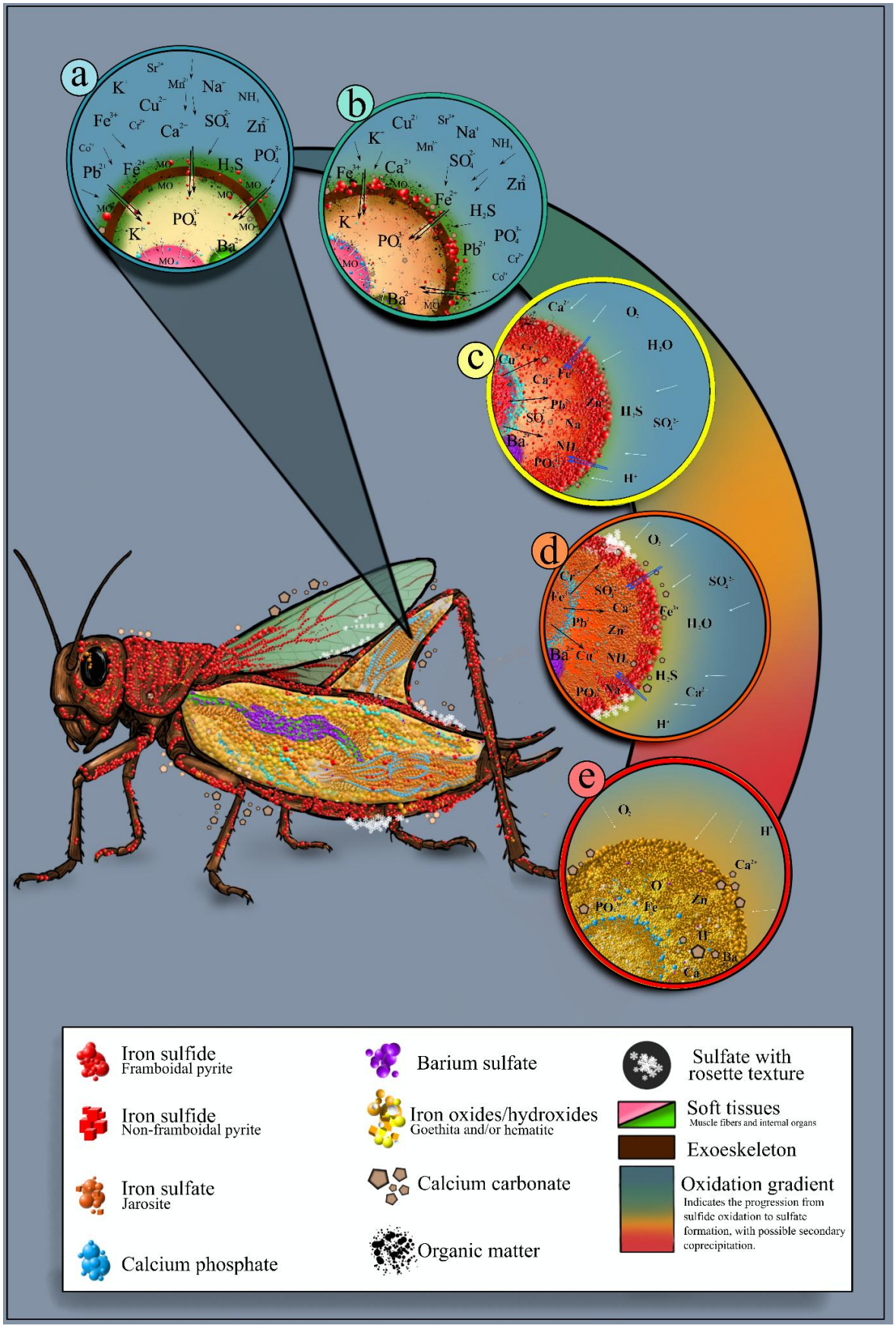

Figure 15. Integrative taphonomic model representing the mineralization processes in fossilized insects from the Crato Formation. Schematic representation of an insect with

enlarged zones (a–d), showing the spatial distribution and interaction between different mineral phases throughout preservation. **(a)** Initial composition of the organism and taphonomic microenvironment, with abundant presence of organic matter, primary calcium phosphate, chemical elements and salts dissolved in the interstitial water, crossing the sulfate reduction zone to the interior of the carcass. **(b)** Internal mineralization by FeS_2 (iron sulfide), associated with phosphorus and barium. **(c)** Oxidative transition zone, where the oxidation of framboidal pyrite promotes the release of elements previously retained during its primary precipitation, giving rise to sulfated mineral phases, mainly from the jarosite group. **(d)** Final stage of preservation after stabilization of the paleoenvironment, with iron sulfates preserving soft tissues, calcium phosphate on muscle fibers and relic pyrite crystals inside the fibers. Some parts of the organs were preserved by barium sulfate and non-oxidized framboidal pyrite, restricted to the cuticle, in addition to the residual presence of organic matter.

Data availability

All relevant data are provided in the article and Supplementary Information file.

5 REFERENCES

1. Brasier, M. D., Antcliffe, J., Saunders, M. & Wacey, D. Changing the picture of Earth's earliest fossils (3.5–1.9 Ga) with new approaches and new discoveries. *Proc. Natl. Acad. Sci. USA* **112**, 4859–4864. https://doi.org/10.1073/pnas.1405338111 (2015).

2. Anderson, R. P., Tosca, N. J., Saupe, E. E., Wade, J. & Briggs, D. E. Early formation and taphonomic significance of kaolinite associated with Burgess Shale fossils. *Geology* **49**, 355–359. https://doi.org/10.1130/G48067.1 (2021).

3. Martill, D. M. & Wilby, P. J. Stratigraphy. In *Fossils of the Santana and Crato Formations, Brazil* (ed. Martill, D. M.) 20–50. Field Guides to Fossils **5** (Palaeontological Association, London, 1993).

4. Martill, D. M., Bechly, G. & Loveridge, R. *The Crato Fossil Beds of Brazil: Window To an Ancient World* (Cambridge University Press, New York, 2007).

5. Martill, D. M. *Fossils of the Santana and Crato formations, Brazil*. Field Guides to Fossils **5**, 158 pp. (Palaeontological Association, London, 1993).

6. Dias, J. J. & Carvalho, I. S. The role of microbial mats in the exquisite preservation of Aptian insect fossils from the Crato Lagerstätte, Brazil. *Cretac. Res.* **130**, 105068. https://doi.org/10.1016/j.cretres.2021.105068 (2022).

7. Barling, N., Martill, D. M., Heads, S. W. & Gallien, F. High fidelity preservation of fossil insects from the Crato Formation (Lower Cretaceous) of Brazil. *Cretac. Res.* **52**, 605–622. https://doi.org/10.1016/j.cretres.2014.05.007 (2015).

8. Osés, G. L. *et al.* Deciphering the preservation of fossil insects: a case study from the Crato Member, Early Cretaceous of Brazil. *PeerJ* **4**, e2756. https://doi.org/10.7717/peerj.2756 (2016).

9. Osés, G. L. *et al.* Deciphering pyritization–kerogenization gradient for fish soft-tissue preservation. *Sci. Rep.* **7**, 1468. https://doi.org/10.1038/s41598-017-01463-z (2017).

10. Dias, J. J. & Carvalho, I. S. Remarkable fossil crickets preservation from Crato Formation (Aptian, Araripe Basin), a Lagerstätten from Brazil. *J. S. Am. Earth Sci.* **98**, 102443. https://doi.org/10.1016/j.jsames.2019.102443 (2020).

11. Storari, A. P. *et al.* Exceptionally well-preserved orthopteran proventriculi from the Cretaceous Crato Formation of Brazil. *J. S. Am. Earth Sci.* **133**, 104737. https://doi.org/10.1016/j.jsames.2023.104737 (2024).

12. Dias, J. J. *et al.* Reproductive organs of a Grylloidea fossil from the Cretaceous Araripe Basin, Brazil. *J. Geol. Soc.* **182**, https://doi.org/10.1144/jgs2024-211 (2025).

13. Assine, M. L., Perinotto, J. A. J., Custódio, M. A., Neumann, V. H., Varejão, F. G. & Mescolotti, P. C. M. Sequências deposicionais do Andar Alagoas da Bacia do Araripe, Nordeste do Brasil. Bol. Geociênc. Petrobras 22, 3–28. https://bgp.petrobras.com.br/bgp/article/view/33 (2014).

14. Varejão, F. G. *et al.* Mixed siliciclastic–carbonate sedimentation in an evolving epicontinental sea: Aptian record of marginal marine settings in the interior basins of north-eastern Brazil. *Sedimentology* **68**, 1457–1482. https://doi.org/10.1111/sed.12846 (2021a).

15. Varejão, F. G. *et al.* Marine or freshwater? Accessing the paleoenvironmental parameters of the Caldas Bed, a key marker bed in the Crato Formation (Araripe Basin, NE Brazil). *Braz. J. Geol.* **51**, e20200009. https://doi.org/10.1590/2317-4889202120200009 (2021b).

16. Martill, D. M., Loveridge, R. & Heimhofer, U. Halite pseudomorphs in the Crato Formation (Early Cretaceous, Late Aptian–Early Albian), Araripe Basin, northeast Brazil: further evidence for hypersalinity. *Cretac. Res.* **28**, 613–620. https://doi.org/10.1016/j.cretres.2006.10.003 (2007).

17. Gueriau, P., Bernard, S. & Bertrand, L. Advanced synchrotron characterization of paleontological specimens. *Elements* **12**, 45–50. https://doi.org/10.2113/gselements.12.1.45 (2016).

18. Riquelme, F., Ruvalcaba-Sil, J. L. & Alvarado-Ortega, J. Palaeometry: Non-destructive analysis of fossil materials. *Bol. Soc. Geol. Mex.* **61**, 177–183 (2009).

19. Delgado, A. O. *et al.* Paleometry: a brand new area in Brazilian science. *Mater. Res.* **17**, 1434–1441. https://doi.org/10.1590/1516-1439.288514 (2014).

20. Gomes, A. L. S. *et al.* Paleometry as a key tool to deal with paleobiological and astrobiological issues: some contributions and reflections on the Brazilian fossil record. *Int. J. Astrobiol.* **18**, 1–15. https://doi.org/10.1017/S1473550418000538 (2019).

21. Prado, G. *et al.* Synchrotron radiation in palaeontological investigations: Examples from Brazilian fossils and its potential to South American palaeontology. *J. S. Am. Earth Sci.* **108**, 102973. https://doi.org/10.1016/j.jsames.2020.102973 (2021).

22. Assine, M. L. Bacia do Araripe. *Bol. Geociênc. Petrobras* **15**, 371–389 (2007).

23. Matos, R. M. D. The Northeast Brazilian Rift System. *Tectonics* **11**, 766–791 (1992).

24. Catto, B., Jahnert, R. J., Warren, L. V., Varejão, F. G. & Assine, M. L. The microbial nature of laminated limestones: Lessons from the Upper Aptian, Araripe Basin, Brazil. *Sediment. Geol.* **343**, 114–132. https://doi.org/10.1016/j.sedgeo.2016.05.011 (2016).

25. Warren, L. V. *et al.* Stromatolites from the Aptian Crato Formation, a hypersaline lake system in the Araripe Basin, northeastern Brazil. *Facies* **63**, 3. https://doi.org/10.1007/s10347-016-0484-6 (2017).

26. Rios-Netto, A., Regali, M. P. S., Carvalho, I. S. & Freitas, F. I. Palinoestratigrafia do intervalo Alagoas da Bacia do Araripe, Nordeste do Brasil. *Rev. Bras. Geociênc.* **42**, 331–342. https://doi.org/10.5327/Z0375-75362012000200009 (2012).

27. Arai, M. & Assine, M. L. Novas datações palinológicas da Formação Romualdo (Bacia do Araripe): sua implicação no arcabouço estratigráfico da sucessão aptiano–albiano das bacias brasileiras. In *Anais do 49º Congresso Brasileiro de Geologia*, 1306 (SBG, Rio de Janeiro, 2018).

28. Melo, R. M. *et al.* New marine data and age accuracy of the Romualdo Formation, Araripe Basin, Brazil. *Sci. Rep.* **10**, 15779. https://doi.org/10.1038/s41598-020-72789-8 (2020).

29. Coimbra, J. C. & Freire, T. M. Age of the post-rift Sequence I from the Araripe Basin, Lower Cretaceous, NE Brazil: implications for spatio-temporal correlation. *Rev. Bras. Paleontol.* **24**, 36–48. https://doi.org/10.4072/rbp.2021.1.03 (2021).

30. Nazari, B., Jorjani, E., Hani, H., Manafi, Z. & Riahi, A. Formation of jarosite and its effect on important ions for *Acidithiobacillus ferrooxidans* bacteria. *Trans. Nonferrous Met. Soc. China* **24**, 1152–1160. https://doi.org/10.1016/S1003-6326(14)63174-5 (2014).

31. Wang, A., Freeman, J. J., Jolliff, B. L. & Chou, I.-M. Sulfates on Mars: A systematic Raman spectroscopic study of hydration states of magnesium sulfates. *Geochim. Cosmochim. Acta* **70**, 6118–6135. https://doi.org/10.1016/j.gca.2006.05.022 (2006).

32. Barros, O. A. *et al.* Physicochemical investigation of shrimp fossils from the Romualdo and Ipubi formations (Araripe Basin). *PeerJ* **7**, e6323. https://doi.org/10.7717/peerj.6323 (2019).
33. Bezerra, F. I. *et al.* Chemical and mineral comparison of fossil insect cuticles from Crato Konservat Lagerstätte, Lower Cretaceous of Brazil. *J. Iber. Geol.* **46**, 61–76. https://doi.org/10.1007/s41513-020-00119-y (2020).

34. Jurašeková, Z. *et al.* Raman spectra and ancient life: vibrational ID profiles of fossilized (bone) tissues. *Int. J. Mol. Sci.* **23**, 10689. https://doi.org/10.3390/ijms231810689 (2022).

35. Wang, S., Ding, N., Ma, W. *et al.* Direct evidence of carnivory in the early-diverging alvarezsaurian *Bannykus*. *Innov. Geosci.* **3**, 100143. https://doi.org/10.59717/j.xinn-geo.2025.100143 (2025).

36. Chen, H. & Stimets, R. W. Fluorescence of trivalent neodymium in various materials excited by a 785 nm laser. *Am. Mineral.* **99**, 332–342. https://doi.org/10.2138/am.2014.4311 (2014).
37. Lenz, C. *et al.* Laser-induced REE^{3+} photoluminescence of selected accessory minerals — An "advantageous artefact" in Raman spectroscopy. *Chem. Geol.* **417**, 46–56. https://doi.org/10.1016/j.chemgeo.2015.09.001 (2015).

38. Culka, A. & Jehlička, J. Sequentially shifted excitation: A tool for suppression of laser-induced fluorescence in mineralogical applications using portable Raman spectrometers. *J. Raman Spectrosc.* **49**, 148–154. https://doi.org/10.1002/jrs.5320 (2018).

39. Fau, A. *et al.* Time-resolved Raman and luminescence spectroscopy of synthetic REE-doped hydroxylapatites and natural apatites. *Am. Mineral.* **107**, 1486–1498. https://hal.science/hal-03775744v3 (2022).

40. Woodring, J. & Lorenz, M. W. Feeding, nutrient flow, and functional gut morphology in the cricket *Gryllus bimaculatus*. *J. Morphol.* **268**, 815–825. https://doi.org/10.1002/jmor.10554 (2007).

41. Martill, D. M. Macromolecular resolution of fossilized muscle tissue from an elopomorph fish. *Nature* **346**, 171–172. https://doi.org/10.1038/346171a0 (1990).

42. McNamara, M. E. *et al.* Soft-tissue preservation in Miocene frogs from Libros, Spain: insights into the genesis of decay microenvironments. *Palaios* **24**, 104–117. https://doi.org/10.2110/palo.2008.p08-017r (2009).

43. Peng, J. *et al.* The synthesis of lead-bearing jarosite and its occurrence characteristic and leaching toxicity evaluation. *Metals* **13**, 941. https://doi.org/10.3390/met13050941 (2023).

44. Liu, J. *et al.* Characterization of the dissolution of tooeleite under *Acidithiobacillus ferrooxidans* relevant to mineral trap for arsenic removal. *Desalin. Water Treat.* **57**, 15108–15114. https://doi.org/10.1080/19443994.2015.1069225 (2016).

45. Buriti, M. D. S., Cézac, P. & Casás, L. Dissolution and precipitation of jarosite-type compounds: state of the art and future perspectives. *C. R. Chim.* **28**, https://doi.org/10.5802/crchim.321 (2025).

46. Bezerra, F. I. *et al.* Throwing light on an uncommon preservation of Blattodea from the Crato Formation (Araripe Basin, Cretaceous), Brazil. *Rev. Bras. Paleontol.* **21**, 245–254. https://doi.org/10.4072/rbp.2018.3.05 (2018).

47. Bezerra, F. I., Solórzano-Kraemer, M. M. & Mendes, M. Distinct preservational pathways of insects from the Crato Formation, Lower Cretaceous of the Araripe Basin, Brazil. *Cretac. Res.* **118**, 104631. https://doi.org/10.1016/j.cretres.2020.104631 (2021).

48. Dias, J. J. *et al.* Mayfly larvae preservation from the Early Cretaceous of Brazilian Gondwana: analogies with modern mats and other Lagerstätten. *Gondwana Res.* **125**, 1–15. https://doi.org/10.1016/j.gr.2023.07.007 (2023).

49. Tribovillard, N., Algeo, T. J., Lyons, T. & Riboulleau, A. Trace metals as paleoredox and paleoproductivity proxies: an update. *Chem. Geol.* **232**, 12–32. https://doi.org/10.1016/j.chemgeo.2006.02.012 (2006).

50. Deditius, A. P. *et al.* A proposed new type of arsenian pyrite: composition, nanostructure and geological significance. *Geochim. Cosmochim. Acta* **72**, 2919–2933. https://doi.org/10.1016/j.gca.2008.03.014 (2008).

51. Gregory, D. D. *et al.* Trace element content of sedimentary pyrite in black shales. *Econ. Geol.* **110**, 1389–1410. https://doi.org/10.5382/econgeo.2015.110.1389 (2015).

52. Dong, W. *et al.* Inquire into Co-doped pyrite crystal structure modifications and implications for flotation behavior: a DFT study. *Appl. Surf. Sci.* **637**, 159404. https://doi.org/10.1016/j.apsusc.2024.159404 (2024).

53. Gregory, D., Meffre, S. & Large, R. Comparison of metal enrichment in pyrite framboids from a metal-enriched and metal-poor estuary. *Am. Mineral.* **99**, 633–644. https://doi.org/10.2138/am.2014.4545 (2014).

54. Tribovillard, N. Re-assessing copper and nickel enrichments as paleoproductivity proxies. *BSGF Earth Sci. Bull.* **192**, 54. https://doi.org/10.1051/bsgf/2021047 (2021).

55. Atienza, N. M. M. *et al.* Refined views of ancient ocean chemistry: tracking trace element incorporation in pyrite framboids using atom probe tomography. *Geochim. Cosmochim. Acta* **349**, 70–89. https://doi.org/10.1016/j.gca.2023.07.013 (2023).

56. Li, Z. *et al.* Sphalerite and pyrite geochemistry from the Pusangguo Co-rich Cu–Zn–Pb skarn deposit, Tibet: implications for element occurrence and mineralization. *Minerals* **13**, 1165. (2023)

57. Bekényiová, A., Štyriaková, I. & Danková, Z. Sorption of copper and zinc by goethite and hematite. *Arch. Tech. Sci.* **12**, 59–66. https://doi.org/10.7251/afts.2015.0712.059B (2015).

58. Liu, W., Zhu, L., Han, J., Jiao, F. & Qin, W. Sulfidation mechanism of ZnO roasted with pyrite. *Sci. Rep.* **8**, 9516. https://doi.org/10.1038/s41598-018-27968-z (2018).

59. Zhou, S., Zhou, L. & Wong, J. W. C. Biosynthesis and characterization of jarosite. *Spectrosc. Spectral Anal.* **24**, 1140 https://www.ncbi.nlm.nih.gov/pubmed/15762545 (2004).

60. Zuo, P., Chen, Q., Xiao, Z., Dong, Y., Sun, J., Sun, X. & Liu, L. Geology and mineral assemblages of the early Cambrian black shales in the South Qinling: Implications for vanadium and barium mineralization. *Ore Geol. Rev.* **161**, 105624 https://doi.org/10.1016/j.oregeorev.2023.105624 (2023).

61. Reeder, R. J. (ed.) *Carbonates: Mineralogy and Chemistry*. (Mineralogical Society of America, 1983).

62. Lorens, R. B. Sr, Cd, Mn and Co distribution coefficients in calcite as a function of calcite precipitation rate. *Geochim. Cosmochim. Acta* **45**, 553–561. https://doi.org/10.1016/0016-7037(81)90188-5 (1981).

63. Bigham, J. M., Carlson, L. & Murad, E. Schwertmannite, a new iron oxyhydroxysulphate from Pyhasalmi, Finland, and other localities. *Mineral. Mag.* **58**, 641–648 (1994).

64. Kawano, M. & Tomita, K. Geochemical modeling of bacterially induced mineralization of schwertmannite and jarosite in sulfuric acid spring water. *Am. Mineral.* **86**, 1156–1165 (2001).

65. Chio, C. H., Sharma, S. K. & Muenow, D. W. Micro-Raman studies of hydrous ferrous sulfates and jarosites. *Spectrochim. Acta A Mol. Biomol. Spectrosc.* **61**, 2428–2433 https://doi.org/10.1016/j.saa.2005.02.021 (2005).

66. Basciano, L. C. & Peterson, R. C. The crystal structure of ammoniojarosite, $(NH_4)Fe_3(SO_4)_2(OH)_6$ and the crystal chemistry of the ammoniojarosite–hydronium jarosite solid-solution series. *Mineral. Mag.* **71**, 427–441 https://doi.org/10.1180/minmag.2007.071.4.427 (2007).

67. Desborough, G. A. et al. Mineralogical and chemical characteristics of some natural jarosites. *Geochim. Cosmochim. Acta* **74**, 1041–1056 https://doi.org/10.1016/j.gca.2009.11.006 (2010).

68. Desborough, G. A. et al. Mineralogical and chemical characteristics of some natural jarosites. *Geochim. Cosmochim. Acta* **74**, 1041–1056 https://doi.org/10.1016/j.gca.2009.11.006 (2010).

69. Raiswell, R. & Canfield, D. E. Sources of iron for pyrite formation in marine sediments. *Am. J. Sci.* **298**, 219–245 https://doi.org/10.2475/ajs.298.3.219 (1998).

70. Rickard, D. Sedimentary iron biogeochemistry. In *Developments in Sedimentology*, vol. **65**, 85–119. https://doi.org/10.1016/B978-0-444-52989-3.00003-9 (2012).

71. Jones, F. S., Bigham, J. M., Gramp, J. P. & Tuovinen, O. H. Synthesis and properties of ternary (K, NH_4, H_3O)-jarosites precipitated from *Acidithiobacillus ferrooxidans* cultures in simulated bioleaching solutions. *Mater. Sci. Eng. C* **44**, 453–464 https://doi.org/10.1016/j.msec.2014.08.043 (2014).

72. Stoffregen, R. E., Alpers, C. N. & Jambor, J. L. Alunite–jarosite crystallography, thermodynamics, and geochronology. In Sulfate Minerals: Crystallography, Geochemistry, and Environmental Significance (eds. Alpers, C. N., Jambor, J. L. & Nordstrom, D. K.) Rev. Mineral. Geochem. 40, 453–479. https://doi.org/10.2138/rmg.2000.40.9 (2000).

73. Squyres, S. W. & Knoll, A. H. Sedimentary rocks at Meridiani Planum: origin, diagenesis, and implications for life on Mars. *Earth Planet. Sci. Lett.* **240**, 1–10 https://doi.org/10.1016/j.epsl.2005.09.038 (2005).

74. Golden, D. C., Ming, D. W., Morris, R. V. & Graff, T. G. Hydrothermal synthesis of hematite spherules and jarosite: implications for diagenesis and hematite spherule formation in sulfate outcrops at Meridiani Planum, Mars. *Am. Mineral.* **93**, 1201–1214 https://doi.org/10.2138/am.2008.2737 (2008).

75. Buzgar, N., Buzatu, A. & Sanislav, I. V. The Raman study on certain sulfates. *An. Ştiint. Univ. "Al. I. Cuza" Iaşi. Geol.* **LV**(1), 1–9 (2009).

76. Schrader, B. Die Möglichkeiten der Raman-Spektroskopie im Nah-Infrarot-Bereich, Teil I. *Chem. Unserer Zeit* **31**, 229–234 https://doi.org/10.1002/ciuz.19970310504 (1997).

77. Gieroba, B., Krysa, M., Wojtowicz, K., Wiater, A., Pleszczyńska, M., Tomczyk, M. & Sroka-Bartnicka, A. The FT-IR and Raman spectroscopies as tools for biofilm characterization created by cariogenic streptococci. *Int. J. Mol. Sci.* **21**, 3811 https://doi.org/10.3390/ijms21113811 (2020).

78. Edwards, H. G. M., Farwell, D. W. & Jorge Villar, S. E. Raman microspectroscopic studies of amber resins with insect inclusions. *Spectrochim. Acta A* **68**, 1089–1095 https://doi.org/10.1016/j.saa.2006.11.037 (2007).

79. Wang, B., Zhao, F., Zhang, H., Fang, Y. & Zheng, D. Widespread pyritization of insects in the Early Cretaceous Jehol Biota. *Palaios* **27**, 707–711 https://doi.org/10.2110/palo.2012.p12-029r (2012).

80. Ivarson, K. C. Microbiological formation of basic ferric sulfates. *Can. J. Soil Sci.* **53**, 279–286 https://doi.org/10.4141/cjss73-046 (1973).

81. Paredes, Á., Acuña, S. M. & Toledo, P. G. AFM study of pyrite oxidation and xanthate adsorption in the presence of seawater salts. *Metals* **9**, 1177 https://doi.org/10.3390/met9111177 (2019).

82. Du, R. et al. Morphology dominated rapid oxidation of framboidal pyrite. *Geochem. Perspect. Lett.* **16**, 2104 https://doi.org/10.7185/geochemlet.2104 (2021).

83. Duverger, A., Berg, J. S., Busigny, V., Guyot, F., Bernard, S. & Miot, J. Mechanisms of pyrite formation promoted by sulfate-reducing bacteria in pure culture. *Front. Earth Sci.* **8**, 588310 https://doi.org/10.3389/feart.2020.588310 (2020).

84. Evangelou, V. P. *Pyrite Oxidation and Its Control*. 1st edn, CRC Press https://doi.org/10.1201/9780203741641 (1995).

85. Qian, G. et al. Strategies for reduced acid and metalliferous drainage by pyrite surface passivation. *Minerals* **7**, 42 https://doi.org/10.3390/min7030042 (2017).

86. Kang, B. et al. Biocementation of pyrite tailings using microbially induced calcite carbonate precipitation. *Molecules* **27**, 3608 https://doi.org/10.3390/molecules27113608 (2022).

87. Schiffbauer, J. D. et al. A unifying model for Neoproterozoic–Palaeozoic exceptional fossil preservation through pyritization and carbonaceous compression. *Nat. Commun.* **5**, 5754 https://doi.org/10.1038/ncomms6754 (2014).

88. Sabeva, R., Velev, S., Kenderov, L., Angelova, B. & Iliev, M. Pyritization of trees from the natural phenomenon Underwater Petrified Forest, Sozopol Bay, Black Sea, Bulgaria. *Rev. Bulg. Geol. Soc.* **85**, 120–123 https://doi.org/10.52215/rev.bgs.2024.85.2.120 (2024).

89. Sasaki, K., Tanaike, O. & Konno, H. Distinction of jarosite-group compounds by Raman spectroscopy. *Can. Mineral.* **36**, 1225–1235 (1998).

90. Saini, S. K., Ransinchung, G. D., Kumar, P. & Ray, S. Investigation of jarosite–cement blends for hydration process and mechanical behavior in PQC mixes. *Innov. Infrastruct. Solut.* **7**, 198 https://doi.org/10.1007/s41062-021-00707-6 (2022).

91. Odin, G. P., Rouchon, V., Béthoux, O. & Ren, D. Gypsum growth induced by pyrite oxidation jeopardises the conservation of fossil specimens: an example from the Xiaheyan entomofauna (Late Carboniferous, China). *Palaeogeogr. Palaeoclimatol. Palaeoecol.* **509**, 104–113 https://doi.org/10.1016/j.palaeo.2018.05.035 (2018).

92. Fellowes, D. & Hagan, P. Pyrite oxidation: the conservation of historic shipwrecks and geological and palaeontological specimens. *Stud. Conserv.* **48**, Suppl. 1, 26–38. https://doi.org/10.1179/sic.2003.48.Supplement-1.26 (2003).

93. Martill, D. M. Preservation of fish in the Cretaceous Santana Formation of Brazil. *Palaeontology* **31**, 1–18 (1988).

94. [94] Wilby, P. R. & Briggs, D. E. Taxonomic trends in the resolution of detail preserved in fossil phosphatized soft tissues. *Geobios* **30**, 493–502. https://doi.org/10.1016/S0016-6995(97)80056-3 (1997).

95. Varejão, F. G., Warren, L. V., Simões, M. G., Fürsich, F. T., Matos, S. A. & Assine, M. L. Exceptional preservation of soft tissues by microbial entombment: insights into the taphonomy of the Crato Konservat-Lagerstätte. *PALAIOS* **34**, 331–348. http://dx.doi.org/10.2110/palo.2019.041 (2019).

96. Waterhouse, D. F. The occurence of barium and strontium in insects. *Aust. J. Biol. Sci.* **4**, 144–162. https://doi.org/10.1071/BI9510144 (1951).

97. Weisener, C. G. & Weber, P. A. Preferential oxidation of pyrite as a function of morphology and relict texture. *N. Z. J. Geol. Geophys.* **53**, 167–176. https://doi.org/10.1080/00288306.2010.499158 (2010).

98. Cruells, M. & Roca, A. Jarosites: Formation, structure, reactivity and environmental. *Metals* **12**, 802. https://doi.org/10.3390/met12050802 (2022).

99. Canfield, D. E. & Des Marais, D. J. Biogeochemical cycles of carbon, sulfur, and free oxygen in a microbial mat. *Geochim. Cosmochim. Acta* **57**, 3971–3984. https://doi.org/10.1016/0016-7037(93)90347-Y (1993).

6 SUPPLEMENTARY MATERIAL

Topic 1. Morphological aspects preserved in the samples

The sample GP/1E11237c is an orthopteran (Fig. 2a,b) and is preserved in gray limestone, in dorsal decubitus, presenting remarkable morphological integrity. The cephalon is preserved, the left foreleg is articulated to the prothorax, with well-preserved femur, tibia and tarsus. The midlegs are connected to the mesothorax, with visible and articulated femurs; on the right leg, the tibial spur is clearly visible. The hindlegs are complete, with femur, tibia and tarsus preserved and connected to the metathorax, with the tibial spur also evident on the right leg. The abdomen is complete and well preserved, and the ovipositor can be clearly seen in its terminal portion, characterizing the specimen as a female. The ovipositor is intact and connected to the dorsal and ventral valves, which in this case are fused and cannot be distinguished morphologically.

The sample GP/1E10501, an orthopteran (Fig. 2c), is preserved in gray limestone, in ventral decubitus. The sample has the head, thorax and the abdomen preserved, both well

defined, with clear abdominal segmentation. The pair of hind legs, part of the pair of forelegs and the antennae, which remain articulated to the head, are also preserved.

The fossil insect of sample GP/1E10609 belongs to Blattodea (Fig. 2d,e) and is preserved in gray limestone in the prone position. The pair of hind legs, including the femur, tibia (with articulated spines) and tarsus, are preserved. The right tegmina is preserved and arranged laterally in an open position. The pair of hind and membranous wings remained closed, in a resting position, retracted over the abdominal dorsum, under the tegmen. Even so, it is possible to observe the apex and the venation veins of these wings, also with excellent preservation. The dorsal view of the fossil reveals the preservation of the head (cephalon), the fused prothorax and mesothorax, and the abdomen. In the terminal portion of the abdomen, under the coxofemoral region, a structure that possibly corresponds to the right cercus can be identified.

The sample GP/1E10836 is also a cockroach (Fig. 2f) and is found in grey limestone, lying prone, with the head preserved, as well as the prothorax, which presents the articulation of the pair of tegmina, which are arranged laterally in an open position. In the mesothorax, the left membranous wing is visible over part of the thorax, abdomen and left hind limb. The impressions of the apex of the wing are faint, but still perceptible between the tibia and the terminal portion of the abdomen. Although partially covered by the matrix or possibly lost in the counterpart of the fossil, the impressions of what would be the pair of left middle legs are visible, located above the pair of hind legs. The latter are better defined, with the femur, tibia (bearing articulated spines) and tarsus clearly preserved. The abdomen displays at least three well-defined tergites and, at its posterior end, a pair of cerci and a single stylet (stylus) are also preserved.

Topic 2. Geochemistry and taphonomic implications

Elements such as iron (Fe) and sulfur (S) presented significantly higher counts in fossiliferous regions, with co-occurrence with the trace elements chromium (Cr), cobalt (Co), copper (Cu), lead (Pb) and zinc (Zn), which indicates pyritization of this material associated with the presence of mineral phases not yet detected and/or incorporation of these elements in pyrite.

Sedimentary pyrite presents a significant enrichment in trace elements such as Co, Pb and Cu, whose incorporation is influenced by complex geochemical processes. Trace metals are mobilized from organic matter and Fe/Mn oxides into pore waters, and arsenic

substitution in the pyrite lattice promotes the uptake of large cations during sediment deposition and early diagenesis (Tribovillard et al., 2006; Deditius et al., 2008; Gregory et al., 2015).

Cobalt replaces iron in pyrite through isomorphic substitution of Fe^{2+} ions by Co^{2+} ions in the crystal lattice. This process is influenced by the geochemical conditions and the availability of cobalt during pyrite formation (Qin et al., 2024; Dong et al., 2024).

Lead (Pb) has a strong affinity for reducing environments, in which it tends to precipitate as sulfide, either in association with diagenetic pyrite or forming its own mineral phases, generally galena (PbS) (Morse & Luther, 1999; Gregory et al., 2015). The incorporation of lead into pyrite occurs at the time of its formation and its concentration in the deposition environment can inhibit the incorporation of other elements into the crystal lattice (Gregory et al., 2014).

In saline-rich waters, copper (Cu) binds to organic particles in the first stages of sedimentation, influencing its distribution and favoring its accumulation in layers rich in organic compounds (Bruland, 1980). During the decomposition of organic matter in the sulfate reduction zone, copper previously bound to organic compounds is released into the sediment pores, where it can react with sulfide ions, forming copper sulfide minerals (Tribovillard et al., 2006; 2021). We can suggest that similar processes are plausible in stratified saline lakes such as the Crato Lagerstätte, in which organic matter and pyrite could equally control copper retention.

Gregory et al. (2015) suggest that the behavior of copper in sedimentary pyrite varies according to environmental conditions, being uniformly incorporated into the crystalline structure under chemically stable environments, which indicates a slow and ordered mineral growth, while in dynamic contexts with rapid chemical fluctuations, Cu is coprecipitated as micro inclusions of copper sulfides, such as chalcopyrite, reflecting faster and more disordered growth.

However, Grand et al. (2018) point out that Cu does not directly replace Fe^{2+} and reinforce that Cu associated with pyrite occurs as inclusions or sulfide nanoparticles, capable of altering the morphology of the crystals. Atienza et al. (2023) demonstrated that Cu can even be incorporated into the crystal structure of pyrite when arsenic (As) replaces sulfur (S) atoms in its structure, modifying the local electronic equilibrium of the crystal lattice, creating sites that facilitate the accommodation of copper (Cu^{2+}), but in most cases it occurs

as nano-inclusions or concentrated at the interfaces between grains, especially in framboidal pyrites.

Zinc (Zn), in turn, is generally found in the form of submicroscopic inclusions of sphalerite (ZnS) within or adjacent to pyrite crystals (Gregory et al., 2015; Li et al., 2023; Ding et al., 2022; Atienza et al., 2023), although some authors propose that this element can also be incorporated into the pyrite structure by coupled substitutions involving Cu^{+} and As^{3-} (Zhuang et al., 2023). In some specific cases, small amounts of Zn can be incorporated into the pyrite structure as a solid solution, partially replacing Fe^{2+} during mineral growth (Büker et al., 1998; Lee et al., 2001). The presence of zinc (Zn) in higher concentrations in oxidized fossils from the beige limestone (BL) subfacies, as described by Osés et al. (2017), compared to the less altered samples of this study, can be attributed to its release during pyrite oxidation. In this process, Zn originally incorporated as an inclusion or solid solution is mobilized and can be retained locally by adsorption on iron oxides (such as goethite or hematite) (Bekényiová et al., 2015). Additionally, experimental studies indicate that gaseous sulfur released during pyrite decomposition can react with zinc oxides (ZnO) present in the microenvironment, promoting the neoformation of sphalerite (ZnS) (Liu et al., 2018). Thus, the Zn preserved in the less oxidized samples may reflect primary mineralization, while in the more oxidized specimens - such as those described by Osés et al. (2017) - it may have been remobilized and incorporated into secondary minerals. These aspects reveal later oxidative processes that reorganized the element into new, more detectable mineral phases. However, in our samples, there is no evidence of neoformed sphalerite crystals (e.g., SEM/EDS), suggesting that such transformation has not occurred or was not preserved, leaving no detectable mineralogical record.

Since As was not detected in the samples of this study, the crystallographic incorporation of these elements into pyrite may be questionable, and it is more plausible that they are associated with distinct mineralogical phases or secondary diagenetic products, predominantly in the form of micro- or nanometric inclusions of minerals such as chalcopyrite ($CuFeS_2$) and galena (PbS) (Gregory et al., 2015; Ding et al., 2022; Song et al., 2023; Zhuang et al., 2023).

Chromium (Cr) in sedimentary environments is conditioned by redox variations. In the minimum oxygen zone (MOZ), Cr is reduced to Cr^{3+}, a less soluble species, which tends to settle in the sediments (Calvert & Pedersen, 1993). This reduction can be mediated by ions such as Fe^{2+}, by oxidizing agents such as H_2O_2, or by biological processes (Huang et al.,

2021). After reduction, Cr^{3+} can be removed from the water column by adsorption on organic matter particles or by coprecipitation with mineral phases (Reinhard et al., 2014). Studies suggest that Cr has a low affinity for direct incorporation into the crystalline structure of pyrite, when compared to other trace elements (Atienza et al., 2023), and analyses of hydrothermal pyrites show no significant correlation between Cr and S (Ding et al., 2022). However, the data from this work reveals a strong correlation between Cr-S, which may indicate that chromium was retained in the sediments during the formation of iron sulfides, possibly by coprecipitation or adsorption on the pyrite surface, even without crystallographic substitution.

Potassium (K) presents a comparable distribution between the fossil and the matrix. The presence of potassium in the matrix may be related to K concentrations attributed to the presence of fine detrital minerals, such as potassic clays or feldspars (Catto et al., 2016). In addition to this possible detrital origin, the association of K^+ with preservation-associated metals suggests its incorporation into secondary mineral phases formed in diagenetic microenvironments enriched in K^+— especially those resulting from the oxidation of sulfides, such as jarosite group minerals, in which K^+ occupies structural positions alongside iron and sulfate.

Aubineau et al. (2019) showed that microbial biofilms can induce potassium enrichment in sediments, promoting the formation of minerals such as illite, and also highlighted that such microbial enrichment of K^+ may be associated with reverse weathering processes, in which dissolved ions are reincorporated into secondary mineral phases that are favored in reducing environments rich in organic matter and mediated by the action of sulfate-reducing bacteria (SRB), being sensitive to factors such as the composition of pore fluids, rate of organic decomposition, and persistence of the reducing zone. The systematic co-occurrence of these metals in fossiliferous regions suggests that their incorporation is directly related to the taphonomic mineralization process and the composition of the interstitial solution at the time of early diagenesis (Wu et al., 2023; Large et al., 2015).

Phosphorus (P) was detected as a subordinate component in the samples, with irregular distribution and relatively low concentrations. Nevertheless, the few points where P is concentrated mostly coincide with regions associated with preserved soft tissues, suggesting a possible link with organic mineralization processes. The moderate correlation between P, S, Cu and Fe in fossil areas reinforces this hypothesis. In fossils from the Crato Lagerstätte, the phosphatization of soft tissues — including muscles and internal structures

— has already been documented (Barling et al., 2015; Osés et al., 2016; Dias & Carvalho, 2022). These processes are favored by persistent anoxic conditions, high bacterial activity and slightly acidic pH, as described in classic studies on early phosphatization in restricted lacustrine and marine environments (Briggs & Wilby, 1996; Lucas & Prévôt, 1991; Martill, 1988). Such conditions promote the release of phosphate from the degradation of organic matter and its subsequent precipitation in the form of calcium phosphate, particularly when calcium (Ca^{2+}) is available in the interstitial fluids of the sediments (Lucas & Prévôt, 1991; Briggs, 2003).

Barium (Ba) was detected locally in a specific region of sample GP/1E11237c, without widespread distribution in the other samples. This suggests that Ba did not actively participate in the widespread taphonomic processes that preserved most of the fossils but may reflect very specific geochemical conditions of a diagenetic microenvironment. Osés et al. (2017) suggested the occurrence of barite (BaSO4) in the thin sections of GL (gray limestone) due to the association between the intensity of barium and sulfur, considering that barium sulfate was involved in diagenetic processes in these microfacies. Barite ($BaSO_4$) forms under sulfated conditions in environments with sulfate-reducing bacterial (SRB) activity, especially when sulfate and barium are available in solution (Zuo et al., 2023; Paytan & Griffith, 2007). Barite formation may occur as an authigenic mineral linked to the degradation of sulfur-rich organic matter or in places where the redox gradient favors the release of Ba^{2+} from ion exchanges with clay minerals or by dissolution of Ba-bearing feldspars. Zuo et al. (2023) described the formation of barite in reducing microenvironments, where $BaSO_4$ precipitation was favored by pH variations and the availability of barium and sulfate in solution. Although the study focuses on marine contexts, the authors suggest that the decomposition of organic matter may act as a source of biogenic barium, a mechanism that may also occur in lacustrine environments rich in organic matter (Maltsev et al., 2023).

In contrast, elements such as calcium (Ca), strontium (Sr), and manganese (Mn) were evenly distributed throughout the sample, with no preferential enrichment in the fossils, indicating that they mainly reflect the composition of the carbonate host and did not actively participate in the taphonomic processes. Manganese (Mn) was diffusely distributed between fossils and rock, with no evident compartmentalization. However, multiple studies indicate that Mn can be incorporated into pyrite by isomorphic substitution to Fe^{2+} or as inclusions adsorbed on crystal surfaces during distinct stages of diagenesis (Ding et al., 2022; Zhuang et al., 2023). For example, Atienza et al. (2023) recorded zoned enrichment of Mn in

framboidal pyrite cores, suggesting its incorporation in early stages of mineral formation under reducing conditions. Our data indicates a great correlation between Mn, Ca and Sr, suggesting alternative geochemical behavior, possibly linked to carbonate phases. The observed association between Mn, Ca and Sr can be explained by the similarity in the ionic radius and charge of the divalent cations Mn^{2+}, Ca^{2+} and Sr^{2+} (Railsback, 1999; Okrusch & Frimmel, 2019), which enables their mutual substitution in crystal structures of carbonate minerals, such as calcite (Reeder, 1983; Finch & Allison, 2007). In biological and diagenetic environments, such substitutions commonly occur during carbonate precipitation and may be influenced by factors such as growth rate and interstitial water composition. Experimental studies demonstrate that Mn and Sr are effectively incorporated into calcite with variable partition coefficients (Lorens, 1981), which reinforces that Mn and Sr are preferentially associated with carbonate phases. Another possibility for this correlation is the widespread occurrence of pyrolusite at the Crato plattenkalk.

Table 1. Raman bands identified in the analyzed samples, accompanied by the color of the collection points, mineralogical attribution, type of vibration observed and the respective references. The bands are related to typical vibrational modes of functional groups present in the minerals, such as symmetrical or asymmetrical stretching and bending.

Suggested attribution	**Band (cm^{-1}) in "BeP" and "BP"**	**Vibrational mode**	**Ref.**
JAROSITE	221 (P2; P4)	Bending vibration (Fe–O)	221 cm-1 (Frost et al., 2005; 2006)
	302 (P2; P4)	Bending vibration (Fe–O)	299 cm-1 (Sasaki et al., 1998; Cao et al., 2017)
	343 (P2)	? Bending vibration (Fe–O)	340 - 343 cm-1 (Frost et al., 2005 e 2006; Sasaki et al., 1998)
	427 (P2; P4)	$\nu_2(SO_4^{2-})$, bending vibration	424 - 434 cm-1 (Cao et al., 2017)
	451 (P2; P4)	$\nu_2(SO_4^{2-})$,	424 - 434 cm-1 (Cao et al., 2017)
	570 (P2; P4)	Bending vibration (OH)	550 cm-1 (Cao et al., 2017)
	624 (P2; P4)	ν_4 (SO_4^{2-})	619 - 624 cm-1 (Cao et al., 2017)

	1005 (P2; P4)	ν_1 (SO_4^{2-})	1005 – 1011 cm-1 (Sasaki et al., 1998; Frost et al., 2005; Cao et al., 2017)
	1091 (P2; P4)	ν_3 (SO_4^{2-}) Asymmetric stretching	1100 – 1111 cm-1 (Cao et al., 2017)
	1161 (P2; P4)	ν_3 (SO_4^{2-}) Asymmetric stretching	1152 - 1165 cm^{-1} (Cao et al., 2017)
MULTIPLE SULFATE PHASES	982 (P2; P4)	ν_1(SO_4^{2-})	980 – 990 cm-1 (Montero et al., 1974; Kloprogge et al., 2002; Dimova et al., 2006; Frost et al., 2014; Omori, 1968; Lakshman, 1941; Buzgar et al., 2014)
PYRITE	342 (P1; P3, P5; P6)	ν(Fe–S)	338 - 343 cm-1 (Ma et al., 2023; Chen et al., 2022; Zhu et al., 2020; Bryant et al., 2018).
	379 (P3)	Ag, symmetric stretch (S–S)	(Yuan & Zheng, 2015; Bryant et al., 2018).
CALCIUM PHOSPHATE	960 (P5)	ν_1(PO_4^{3-}) Symmetric stretching	960 cm-1 (Sauer et al., 1994; Penel et al., 2002)
CALCITE	1089 (P6)	ν_1(CO_3^{2-}) Symmetric stretching	1086(+) cm-1 (Yin et al., 2017; Han et al., 2024; Itoh, 2024)
GYPSUM	1005 – 1008 (P3; P6)	ν_1(SO_4^{2-})	(1005 - 1009 cm-1 (Prasad, 2001, Chio et al., 2004)
Possibly phosphate or, less likely, carbonate)	1189 (P5)	Photoluminescence (possibly Nd3+)	(Chen & Stimets., 2014; Lenz et al., 2015; Culka & Jehlička, 2017; Fau et al., 2022)

Possibly phosphate or, less likely, carbonate	1172 (P5)	Possibly phosphate or, less likely, carbonate	(Chen & Stimets., 2014; Lenz et al., 2015; Culka & Jehlička, 2017; Fau et al., 2022)

Table 2. Shapiro-Wilk normality test applied to elementary data transformed into $\log_{10}$. The W statistic expresses the degree to which the data adheres to a normal distribution — values closer to 1 indicate greater conformity. The p-value represents statistical significance: results lower than 0.05 indicate that the data differ significantly from normality, thus rejecting the null hypothesis.

Element	**P**	**S**	**K**	**Ca**	**Cr**	**Mn**	**Fe**	**Co**	**Cu**	**Zn**	**Sr**	**Pb**
W	0.59	0.87	0.97	0.97	0.69	0.96	0.86	0.62	0.70	0.72	0.96	0.68
p-value	0	0	0.45	0.36	0	0.26	0	0	0	0	0.25	0

CONCLUSÃO

A presente dissertação avançou significativamente na compreensão da preservação de insetos fósseis da Formação Crato, integrando abordagens morfológicas, químicas e mineralógicas. Os resultados evidenciam que a preservação desses fósseis não se limita à querogenização, como sugerido por modelos anteriores, mas envolve uma complexa interação de processos tafonômicos, incluindo piritização, fosfatização de tecidos moles e formação de sulfatos, como jarosita, gipsita e barita.

A análise detalhada da distribuição química e das texturas mineralógicas revelou microambientes redox distintos dentro de um mesmo organismo, indicando que a preservação segue um gradiente tafonômico em vez de uma dicotomia rígida. A identificação inédita de jarosita associada à piritização em calcário cinza e a ausência de matéria orgânica residual reforçam a complexidade desses processos e oferecem novos parâmetros para avaliação da qualidade de preservação em Lagerstätten.

Além de aprofundar o entendimento tafonômico da Formação Crato, este estudo fornece contribuições metodológicas e conceituais que podem ser aplicadas em outros contextos paleontológicos e, potencialmente, na paleontologia forense, permitindo a

caracterização detalhada de fósseis e de seus microambientes originais. Em suma, a dissertação evidencia que a preservação de insetos fósseis é um processo multifacetado, influenciado por condições geoquímicas localizadas, e propõe um modelo integrativo que serve como referência para estudos futuros sobre Lagerstätten e preservação excepcional de organismos fósseis.

ANEXOS

ANEXO 1. PONTOS DE MEDIDAS DE FLUORESCÊNCIA DE RAIOS-X (XRF)

Nesta seção, são apresentados os resultados extras da análise de fluorescência de raios X (XRF) realizada na amostra GP/1E 11237c, fóssil de gafanhoto proveniente da Formação Crato (Fig. 1-3).

Figura 1. Amostra GP/1E 11237c. Os pontos analisados estão representados por cores diferentes, que identificam diferentes regiões da amostra: pontos vermelhos indicam as medidas feitas da interface entre a matriz e o exoesqueleto do fóssil; pontos verdes indicam as medidas feitas na matriz da amostra. Pontos amarelos indicam as áreas mais escuras

(marrom a preto); e, pontos azuis indicam as áreas de medida no fóssil nas áreas mais claras (bege). Os pontos internos são representados marcações com texto rosa e os pontos externos são os de texto laranja.

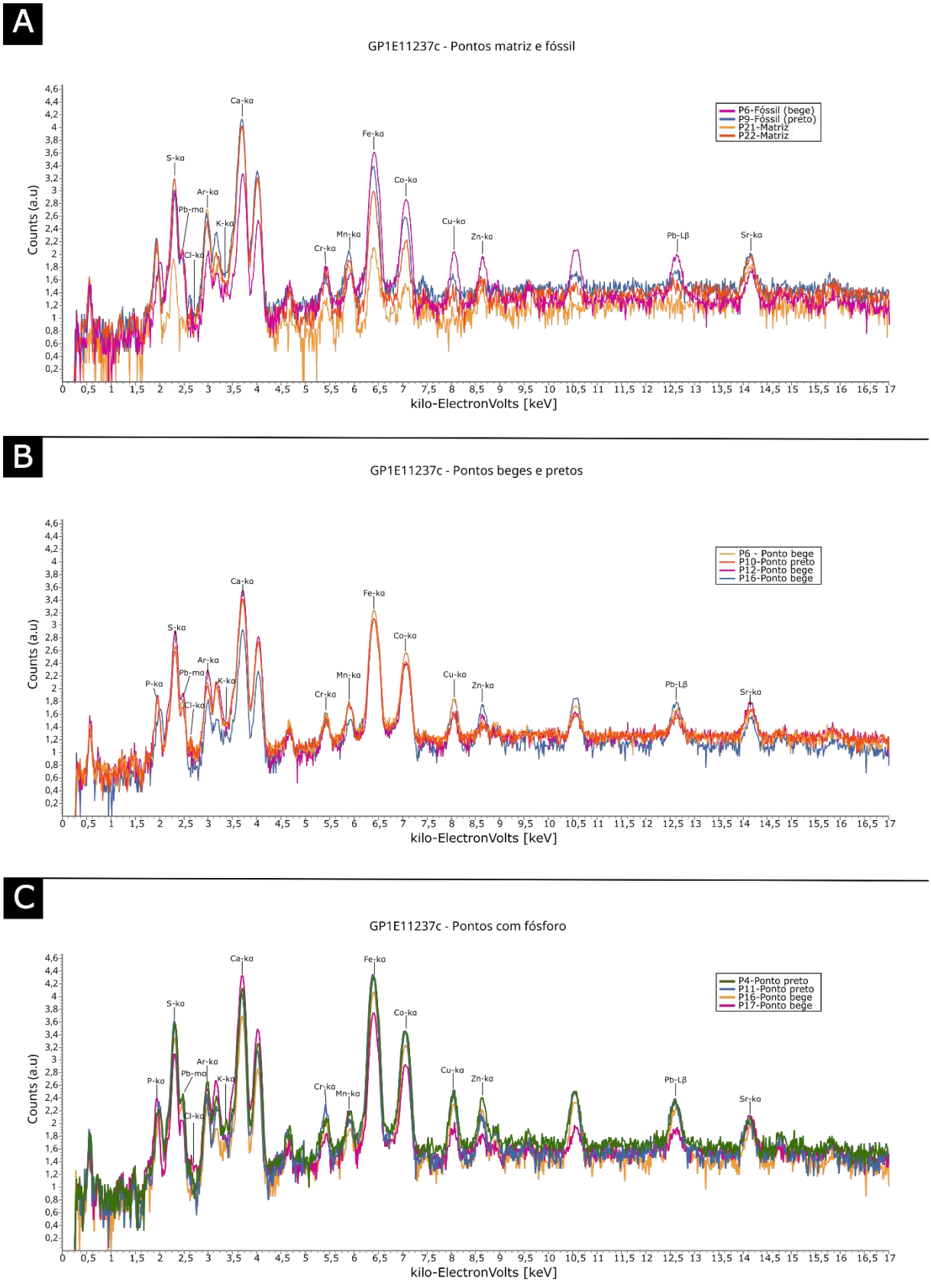

Figura 2. Espectros de XRF da amostra GP1E 11237C.**A.** Comparação das contagens de elementos entre a matriz e o fóssil. **B.** Comparação entre pontos pretos e marrons em relação

aos pontos beges. **C.** Comparação dos pontos escuros com os pontos beges onde há contagens de fósforo.

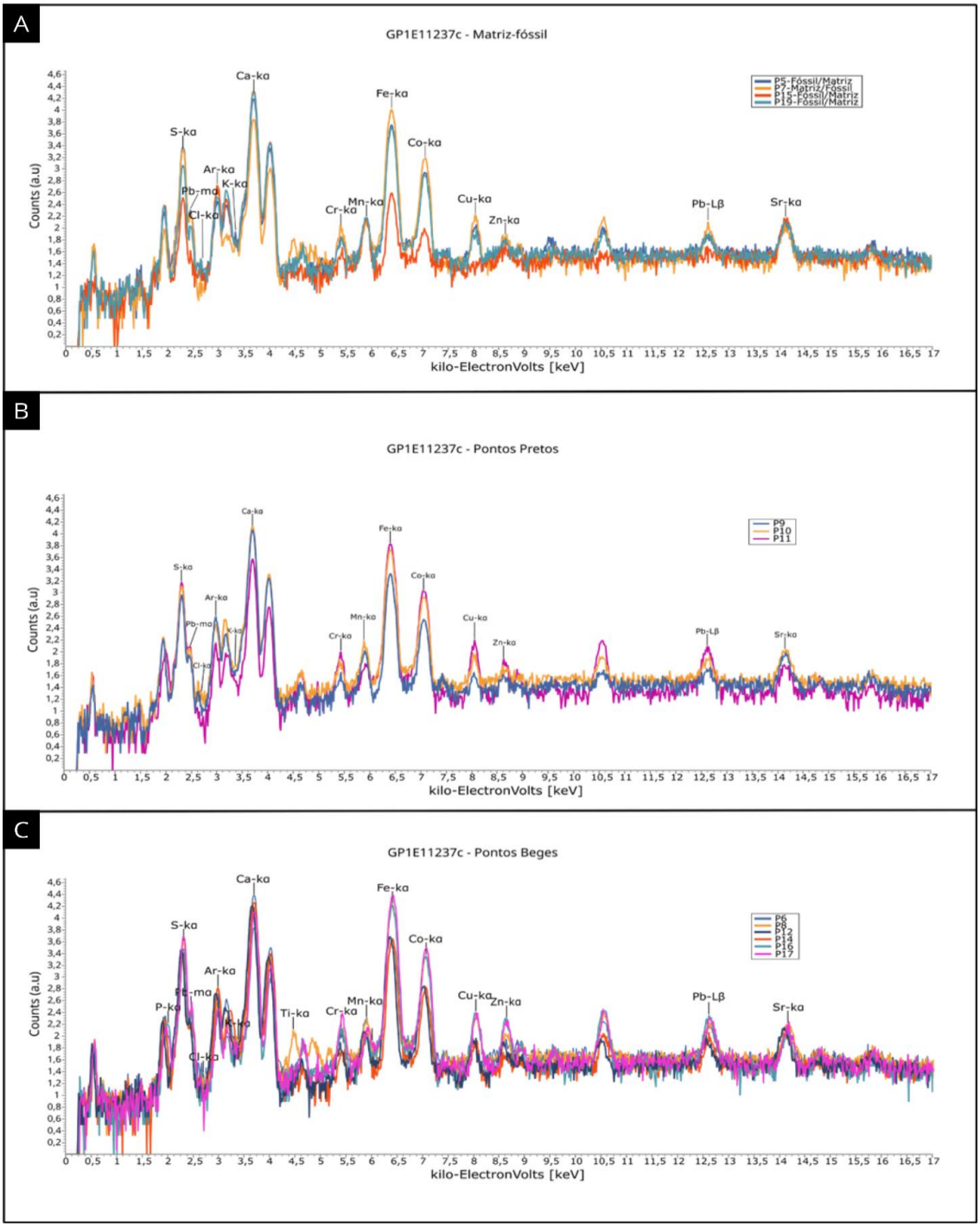

Figura 3. Espectros de XRF da amostra GP1E 11237C, abrangendo uma análise de diferentes pontos da matriz calcária e do fóssil. **A.** pontos próximos a matriz (interface matriz-fóssil). **B.** pontos de coloração mais escuras, geralmente preta. **C.** pontos bege.

ANEXO 2

Tabela 1. Contagens de fótons medidas pelo detector de xrf em $\log_{10}$ para a amostra gp1e 11237c. As intensidades foram normalizadas pelo argônio (ar) e estão apresentadas em unidades de contagem por segundo (cps) correspondendo aos elementos encontrados na amostra. Valores zerados indicam que o elemento não ocorreu ou está abaixo do limite de detecção pela técnica.

	P	S	CL	Ar	K	Ca	Cr	Mn	Fe	Co	Cu	Zn	Sr	P
Nº Atômico	15	16	17	18	19	20	24	25	26	27	29	30	38	8
Energia	2.013	2.307	2.622	2.957	3.313	3.691	5.412	5.895	6.399	6.925	8.041	8.631	14.142	10.
P1	0.000	4.252	2.622	3.517	2.875	4.989	2.818	3.094	5.173	3.113	3.374	3.359	3.118	3
P2	0.000	4.158	2.682	3.517	2.735	5.033	2.787	3.075	5.148	3.096	3.264	2.754	3.122	3
P3	0.000	4.048	2.661	3.517	2.725	5.088	2.589	3.055	5.011	3.038	3.153	2.708	3.143	3
P4	2.806	4.264	2.757	3.517	2.839	4.914	2.943	3.024	5.209	3.189	3.443	3.360	3.068	3
P5	0.000	4.324	2.792	3.517	2.930	5.257	2.847	3.214	4.943	2.957	3.125	2.912	3.332	3
P6	0.000	4.157	2.738	3.517	2.747	5.120	2.876	3.147	5.065	3.080	3.312	2.629	3.147	3
P7	0.000	4.134	2.497	3.517	2.557	4.780	2.905	3.042	5.062	2.972	3.215	2.848	3.134	3
P8	0.000	4.396	2.733	3.517	2.950	5.079	3.082	3.219	5.239	3.189	3.376	3.007	3.399	3
P9	0.000	3.836	2.478	3.517	2.658	5.070	2.382	2.962	4.430	2.530	2.415	2.392	3.101	2
P10	0.000	4.076	2.731	3.517	2.817	5.206	2.744	3.163	4.922	2.971	2.921	2.615	3.251	3
P11	3.316	4.540	2.974	3.517	3.094	5.073	3.425	3.149	5.462	3.421	3.727	3.369	3.391	3
P12	0.000	4.136	2.667	3.517	2.706	4.992	2.649	2.966	4.596	2.702	2.814	2.761	3.159	2
P13	0.000	4.704	3.006	3.517	3.092	5.033	3.710	3.407	5.631	3.546	3.833	3.863	3.466	3
P14	0.000	4.012	2.515	3.517	2.802	4.958	2.508	2.865	4.497	2.596	2.695	2.422	3.014	2
P15	0.000	3.116	0.000	3.517	2.630	5.145	2.220	3.042	3.541	2.367	0.000	2.476	3.196	0
P16	3.326	4.538	2.818	3.517	2.887	4.996	3.369	3.167	5.494	3.429	3.744	3.634	3.456	3
P17	2.937	4.567	2.966	3.517	2.958	5.076	3.489	3.183	5.463	3.401	3.552	3.469	3.445	3
P18	0.000	4.423	0.000	3.517	2.910	5.056	3.292	3.148	5.114	3.084	3.267	3.412	3.279	3
P19	0.000	3.913	2.579	3.517	2.750	5.236	2.649	3.159	4.767	2.872	2.853	2.715	3.221	2
P20	0.000	3.089	1.416	3.517	2.608	5.034	2.492	2.892	3.839	0.000	0.000	0.000	3.083	0
P21	0.000	2.548	1.378	3.517	2.501	4.964	2.153	2.857	3.157	0.000	0.000	2.400	2.990	0
P22	0.000	4.090	0.000	3.517	2.695	5.137	2.809	3.009	4.201	2.481	0.000	2.675	3.245	0

ANEXO 3

Testes de associações elementares.

Análises de associação dos elementos revelando a distribuição suas distribuições em diferentes pontos da amostra. Os pares Sr e Ca e Fe e S variam independentemente, ou seja, aumentos ou diminuições de um elemento são geralmente acompanhados pelo outro (Figura 4A).

As observações acima têm relação com a localização dos pontos de análise. Nos pontos mais internos do fóssil, a presença de ferro é maior do que a de cálcio. Em contraste, nos pontos situados na matriz, a concentração de cálcio é mais elevada.

Para Ca e Fe, observa-se que quando as contagens de Ca aumentam, as contagens de Fe tendem a diminuir (Figura 4a). Essa inversão também se reflete nas contagens de S, que tende a diminuir junto com o Fe, e aumentar quando a concentração de Fe é elevada. O estrôncio, por sua vez, pouco muda na presença de Fe. A Figura 4C detalha a comparação das contagens entre Fe e outros metais (Pb, Zn e Cu). Assim como as contagens de enxofre são vistas oscilando em conjunto com as contagens de ferro, Pb, Zn e Cu, também evidenciam a variação em conjunto. Portanto, elementos podem estar correlacionados entre si.

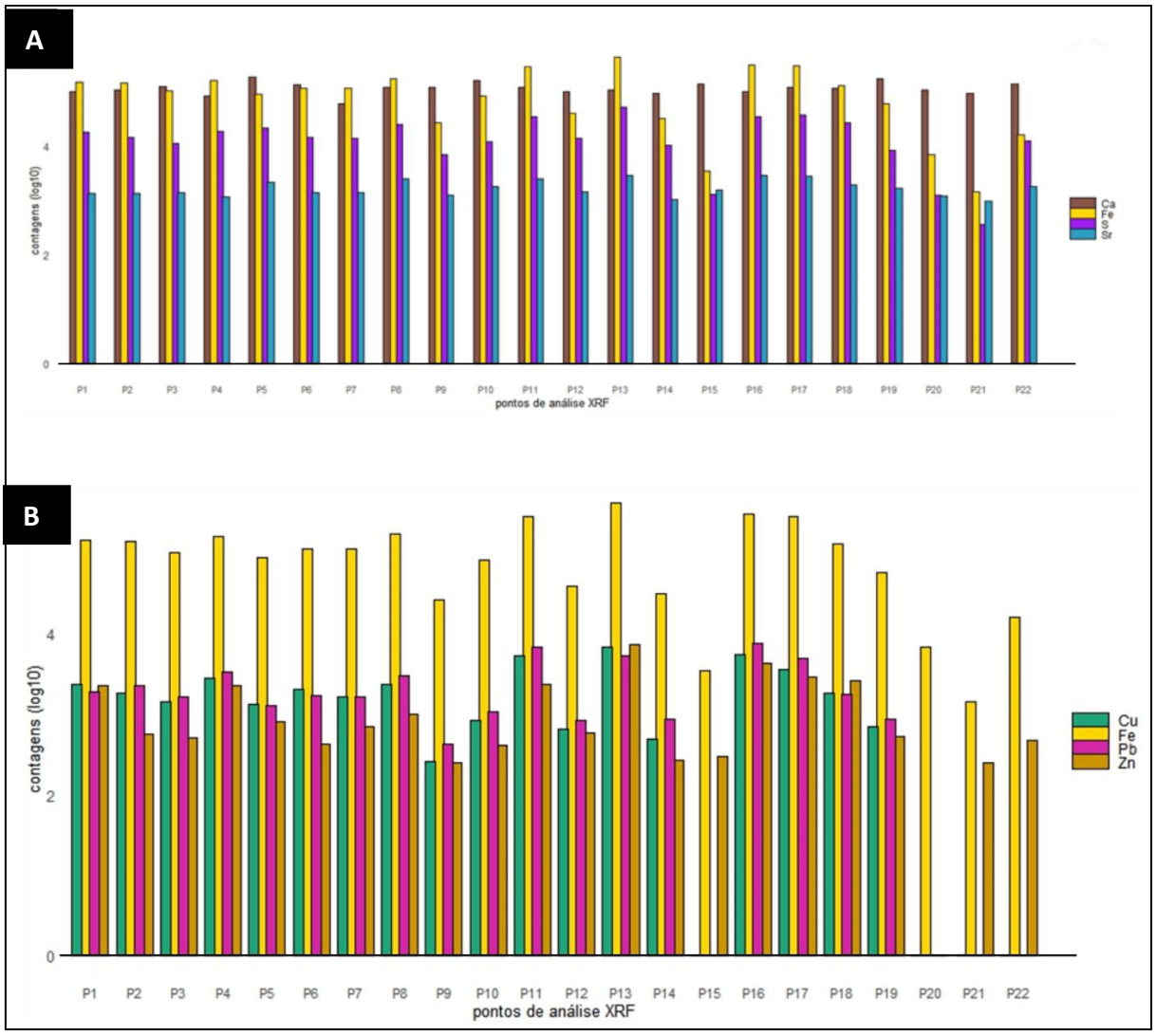

Figura 4. Comparação entre diferentes pontos da amostra GP/1E 11237c. **A.** Padrão de variação de Ca, Fe, S e Sr. **B.** Padrões apresentados pelos principais metais detectados na amostra (Cu, Fe, Pb e Zn).

De maneira isolada, comparamos as contagens de Ca e P, para verificar se há compostos de fosfato de cálcio (Figura 5A). Apenas quatro pontos tiveram presença significativa de P, sendo três pontos pretos e um bege. Devido à limitação do número de pontos com P, não foi observada relação clara entre este e outros elementos.

A média das contagens de elementos foi determinada para diferentes pontos de interesse: no centro do fóssil (pontos internos), interface matriz-fóssil (pontos externos) e matriz. O Ca presente nos pontos externos é ligeiramente mais expressivo, por outro lado, os demais elementos apresentam contagens mais elevadas no interior do fóssil.

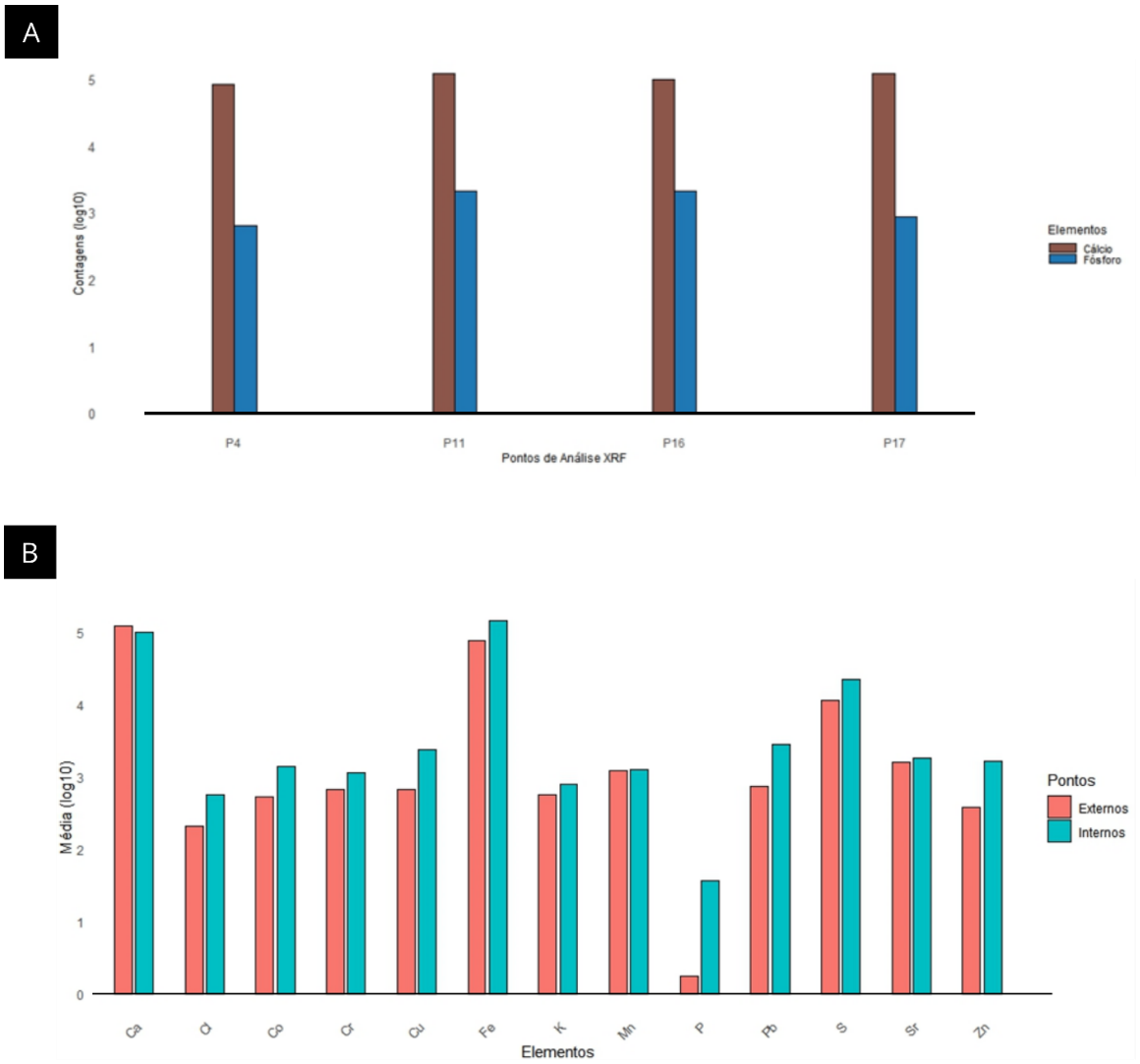

Figura 5. Comparação entre diferentes pontos da amostra GP/1E 11237c. **A.** Pontos com incidência de fósforo, com comparação de P e Ca. **B.** Média da contagem dos elementos de todos os pontos comparando os pontos próximos à interface matriz-fóssil (externos) e pontos internos do fóssil (internos).

3.1 MICROSCOPIA ELETRÔNICA DE VARREDURA (MEV) E ESPECTROSCOPIA POR ENERGIA DISPERSIVA (EDS)

ANEXO 4. MICROSCOPIA E ESPECTROSCOPIA DE ENERGIA DISPERSIVA – AMOSTRA GP/1E 10776

As micrografias da amostra GP1E 10776 revelam diversos detalhes importantes sobre a preservação e a estrutura interna do fóssil. Inicialmente, a amostra é mostrada em seu estado original antes da realização da secção transversal, proporcionando uma visão geral de sua forma e integridade (Figura 28A). A tridimensionalidade do fóssil é particularmente evidente em uma vista lateral após a secção transversal, que destaca a profundidade e a complexidade das estruturas internas preservadas (Figura 28B).

Para análise detalhada, selecionamos a região de interesse (Figura 26Cque revelam feições que não são puramente geológicas (Figura 28D).

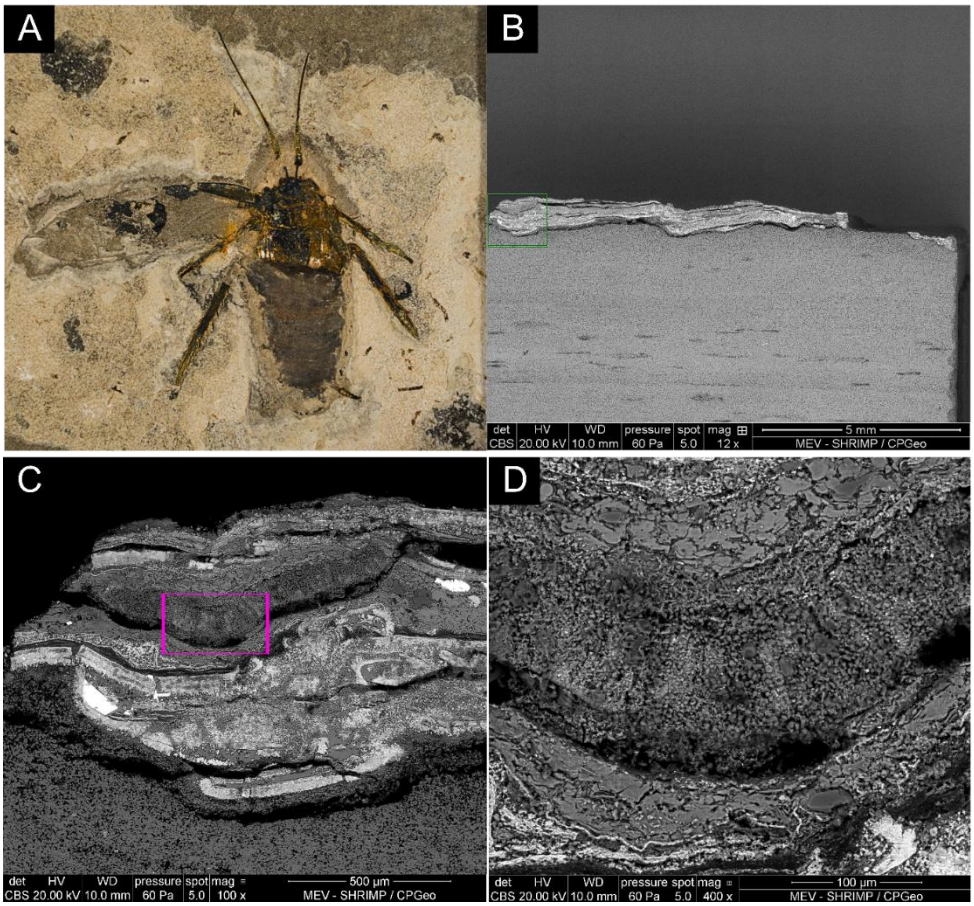

Figura 28. Micrografias da amostra GP1E 10776 **A.** Amostra antes da secção transversal**. B.** Vista lateral do fóssil após a secção. Tridimensionalidade evidente. **C.** Área 1 com regiões de interesse marcadas com retângulos coloridos. **D.** Detalhe da área rosa marcada em C, sendo um possível órgão mineralizado.

O mapa de EDS gerado na região onde as estruturas preservadas se assemelham a mesentérios de insetos da família Blattodea (Figura 29A) Os mapas revelam que essas são majoritariamente preservadas por Fe e S, ou seja, por pirita (Figura 29C).

Observa-se nos mapas dos elementos químicos e nos mapas de combinação dos elementos que essas estruturas são preservadas internamente por sulfeto de ferro e são envoltas por apatita, e calcita. Essa "capa" que envolve esses possíveis órgãos também possuem cristais placoides onde o silício (Si) ocorre em conjunto com alumínio (Al) e potássio (K) (Figura 29F), que podem sugerir a presença de aluminossilicatos.

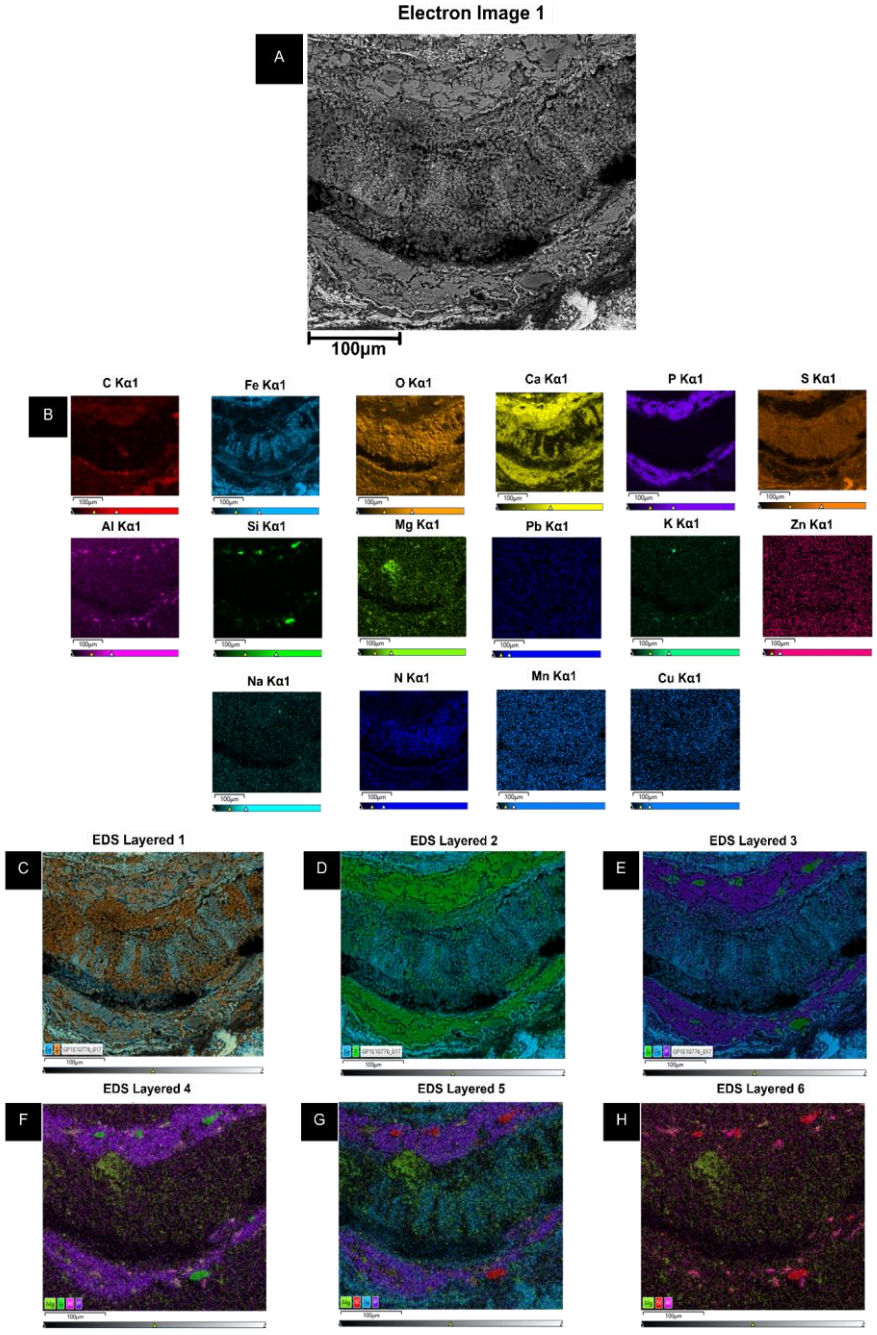

Figura 29. Mapeamento elementar de EDS de possível órgão na amostra GP1E 10836. **A.** Imagem da área de interesse. **B**. Mapas elementares. **C.** Associação dos elementos Fe e S evidenciando a pirita como mineral de preservação interna. **D.** Combinação de Fe e P evidenciando a "capa" de fosfato encapsulando a estrutura preservada por sulfeto de ferro. **E.** Combinação dos elementos Fe, Si e P. **F.** Sobreposição dos mapas de Mg, Si, Al e P. **G.** Combinação de Mg, Si, Fe e P. **G.** Junção dos mapas de Mg Si e Al.